University of Science and Technology of China

Hefei, CHINA

Measurement of charm production cross-section and leptons from its semileptonic decay at RHIC

A dissertation submitted

for the degree of

Doctor of Philosophy in Physics

by

Yifei Zhang

Co-supervisors: Ziping Zhang, Nu Xu

2007

Dedicated to my dear family

谨献给我亲爱的父母

<div align="center">

ABSTRACT OF THE DISSERTATION

Measurement of charm production cross-section and leptons from its semileptonic decay at RHIC

by

Yifei Zhang

Doctor of Philosophy in Physics

University of Science and Technology of China, Hefei, 2007

</div>

The strong interaction, one of the four fundamental forces of nature, is confining: there is no single quark as a color-triplet state observed experimentally. *Quantum Chromodynamics* (QCD) is believed to be a correct basic gauge field theory of strong interactions. Lattice QCD calculations predict a phase transition from hadronic gas to a new matter, *Quark-Gluon Plasma* (QGP), at high energy nuclear-nuclear collisions. In this new form of matter, quarks are deconfined and approach local thermalization. One of the ultimate goals of the heavy ion collision experiments is to search for the QGP matter and study its properties. The Relativistic Heavy Ion Collider (RHIC) located at Brookhaven National Laboratory (BNL) provides a high energy density environment to create and search for the QGP matter by colliding ions like Au at energies up to $\sqrt{s_{\mathrm{NN}}}$=200 GeV. Recent experimental studies at RHIC have given strong evidences that the nuclear matter created in Au+Au collisions at $\sqrt{s_{\mathrm{NN}}}$=200 GeV has surprisingly large collectivity and opacity as reflected by its hydrodynamic behavior at low p_T and its particle suppression behavior at high p_T.

Charm quarks provide a unique tool to probe the partonic matter created in relativistic heavy-ion collisions at RHIC energies. Due to their large quark mass ($\simeq 1.3$ GeV/c^2), charm quarks are predicted to lose less energy than light quarks via only gluon radiation. A measurement of the nuclear modification factor for the charmed hadrons semileptonic decayed single electrons compared to light hadrons is valuably important to complete

<div align="center">

5

</div>

the picture of the observed jet-quenching phenomenon and help us better understand the energy-loss mechanisms at parton stage in Au+Au collisions at RHIC.

Furthermore, the interactions between charm quarks and the medium could boost the radial and elliptic flow resulting in a different charm p_T spectrum shape. Due to its large mass, a charm quark could acquire flow from the sufficient interactions with the surrounding partons in the dense medium. The measurement of charm flow and freeze-out properties is vital to test light flavor thermalization and the partonic density in the early stage of heavy ion collisions.

Charm quarks are believed to be produced only at early stages via initial gluon fusions and its cross section can be evaluated by perturbative QCD calculations. Thus study of the binary collision (N_{bin}) scaling properties for the total charm cross-section from different collision systems can test the theoretical assumptions and determine if charm quarks are indeed good probes to the partonic matter created in high energy heavy ion collisions. Charm total cross-section measurement is also essential for the separation of bottom contribution in non-photonic electron measurement, and for the model calculations, which tries to explain the observed similar suppression pattern of J/Ψ at RHIC and SPS.

In this thesis, we present the measurements of $D^0 \to K\pi$ at low p_T ($p_T \leq 2 \text{ GeV}/c$) and non-photonic electron spectra ($0.9 \leq p_T \leq 5 \text{ GeV}/c$) from D^0 semi-leptonic decay. In addition, we use a newly proposed technique to identify muons from charm decays at low p_T. The combination of all these three measurements stringently constrains the total charm production cross-section at mid-rapidity at RHIC. They also allow the extraction of the charmed hadron spectral shape and a study of possible charm radial flow in Au+Au collisions.

D^0 mesons were reconstructed from hadronic decay $D^0 \to K^-\pi^+$ ($\bar{D}^0 \to K^+\pi^-$) with a branching ratio of 3.83% in minbias Au+Au collisions. The D^0 yields were obtained from fitting a Gaussian plus a linear (or a second-order polynomial function) for residual background to the invariant mass distributions of kaon-pion pairs after mixed-event combinatorial background subtraction.

The inclusive muons at $0.17 \leq p_T \leq 0.25$ GeV/c in minbias Au+Au and central Au+Au collisions were analyzed by combining the ionization energy loss (dE/dx) measured in the Time Projection Chamber (TPC) and the mass calculated from the Time Of Flight (TOF) detector at STAR after the residual pion contamination subtracted. The dominant background muons from pion/kaon weak decays were statistically subtracted using the distribution of the distance of closest approach to the collision vertex (DCA).

Inclusive electrons up to $p_T = 5$ GeV/c are identified by using a combination of velocity (β) measurements from the TOF detector and dE/dx measured in the TPC. Photonic background electrons are subtracted statistically by reconstructing the invariant mass of the tagged $e^{\pm}$ and every other partner candidate $e^{\mp}$ using a 2-dimensional invariant mass method. Partner track finding efficiency is estimated from STAR Geant + Monte Carlo embedding data. More than $\sim 95\%$ of photonic background (photon conversion and π^0 Dalitz decay) can be subtracted through this method. The p_T spectra for non-photonic electrons in central Au+Au minbias Au+Au collisions and its subdivided centralities will be presented. In addition, the method to extract the elliptic flow v_2 of non-photonic electron is also developed in the thesis.

By combining these three independent measurements: $D \rightarrow K\pi$, muons and electrons from charm semileptonic decays in minbias and central Au+Au collisions at RHIC, we observed that: The transverse momentum spectra from non-photonic electrons are strongly suppressed at $0.9 \leq p_T \leq 5$ GeV/c in central Au+Au collisions relative to d+Au collisions. For electrons with $p_T \gtrsim 2$ GeV/c, corresponding to charmed hadrons with $p_T \gtrsim 4$ GeV/c, the suppression is similar to that of light baryons and mesons. The blast wave fit to the electron spectra with $p_T \lesssim 2$ GeV/c indicates that charmed hadrons may interact and decouple from the system differently from multi-strange hadrons and light hadrons. Future upgrades with a direct reconstruction of charmed hadrons are crucial for more quantitative answers. Charm differential cross-sections at mid-rapidity ($d\sigma_{c\bar{c}}^{NN}/dy$) are extracted from a combination of the three measurements covering $\sim 90\%$ of the kinematics. The total charm cross-section per nucleon-nucleon collision ($\sigma_{c\bar{c}}^{NN}$) is reported as $1.40 \pm 0.11(stat.) \pm 0.39(sys.)$ mb in $0 - 12\%$ central Au+Au and $1.29 \pm 0.12 \pm 0.36$ mb in

minbias Au+Au collisions at $\sqrt{s_{\rm NN}}$=200 GeV. The charm production cross sections are found to follow the number of binary collisions scaling. This supports the assumption that hard processes scale with binary interactions among initial nucleons and charm quarks can be used as a probe sensitive to the early dynamical stage of the system.

In the above measurements, the bottom contribution to the non-photonic electron spectrum is neglected. The separation of bottom and charm contributions in current non-photonic electron measurements is very difficult. There are large uncertainties in the model predictions for charm and bottom production in high-energy nuclear collisions. Thus identification of bottom from the non-photonic electron measurements is crucial to better understand charm physics. In the discussion section of this thesis, we will try a fit to non-photonic electron spectrum and estimate the bottom contributions. We will also compare the v_2 distribution from simulation to the experimental data and estimate the possible charm v_2.

RHIC能区粲夸克产生截面和
粲粒子半轻子衰变道的研究

张一飞

中国科学技术大学

摘　要

自然界四大基本作用力之一的强相互作用具有禁闭特性：夸克禁闭在强子中，实验尚未观测到自由夸克。量子色动力学（QCD）被认为是一种正确的用来描述强相互作用的基本规范场理论。格点 QCD 计算预言在高能核核碰撞中可能会产生从强子气到一种新物质：夸克－胶子等离子体（QGP）的相变。在这种新的物质形态下，夸克会解禁闭从而达到局部热平衡状态。寻找 QGP 物质并研究其特性是重离子对撞实验最终目标之一。位于美国布鲁克海汶国家实验室（BNL）的相对论重离子对撞机（RHIC）通过质心能量高达 200 GeV 的核核碰撞来提供用于产生和寻找 QGP 物质的高能量密度的环境。近期在 RHIC 运行的实验研究表明 200 GeV 金金碰撞产生的核物质具有相当强的集体运动效应和对末态强子的不透明性。主要表现在低横动量区域的流体动力学行为和高横动量区域的粒子产额压低。

粲夸克被认为是研究 RHIC 能区相对论重离子碰撞中产生的部分子物质的理想探针。由于它的质量比较大，约 $1.3 \text{ GeV}/c^2$，理论预言粲夸克通过胶子辐射损失的能量要比轻夸克少。因此测量粲夸克强子半轻子衰变的单电子的核修正因子，并与轻强子作比较，对于构造完整的喷柱淬灭的物理图像以及帮助我们理解 RHIC 能区金金碰撞中部分子能损机制都有着非常重要的意义。

此外，粲夸克和碰撞产生的物质之间的相互作用可能会形成粲夸克的径向流和椭圆流，从而改变粲夸克横动量谱的分布形状。由于粲夸克的质量较大，在与周围的高密度物质经过足够多的相互作用后，可能会获得集体运动流效应。实验上测量粲夸克强子的流效应和冻结温度等特性，对检验早期重离子碰撞中轻味夸克热化和部分子密度具有相当重要的意义。

粲夸克被认为通过碰撞初始的胶子聚合产生，其产生截面可以用微扰 QCD 理论计算。因此研究不同碰撞系统下粲夸克产生截面及其对于两两碰撞数的标度不变特性对于检验理论和检验粲夸克是否是高能重离子碰撞中产生的部分子物质的理想探针都非常重要。粲夸克产生截面的测量是电子测量中分离底夸克的贡献，以及对试图解释 RHIC 和 SPS 观测到的 J/Ψ 压低现象的理论模型的不可或缺的重要依据。

这篇论文里，我们将介绍低横动量区间（$p_T \leq 2$ GeV/c）$D^0 \rightarrow K\pi$ 强子衰变道和粲夸克半轻子衰变的单电子谱（$0.9 \leq p_T \leq 5$ GeV/c）。另外，我们还提出一种新的方法来鉴别低横动量区间粲夸克半轻子衰变的 μ 子。联合以上三种独立的测量，可以较为精确的给出 RHIC 能区金金碰撞中中心快度区的粲夸克产生截面，并且可以很好的描述粲夸克强子的横动量谱形状，以及研究可能的粲夸克径向流。

在最小偏置金金碰撞中，通过 $D^0 \rightarrow K\pi$ 强子衰变道（分支比为 3.83%）来重建 D^0 介子的质量峰。在 K，π 不变质量峰减除了混和事例背景之后，用线性或二次函数加上一个高斯函数来拟合 D^0 介子的质量峰，从而得到 D^0 介子的产额。

在最小偏置金金碰撞中和中心金金碰撞中，通过联合 STAR 探测器上时间投影室（TPC）测得的电离能损（dE/dx）和飞行时间谱仪（TOF）测得的粒子质量谱来鉴别低横动量区间（$0.17 \leq p_T \leq 0.25$ GeV/c）的 μ 子。在 μ 子质量谱中，减除了 π 的污染。主要的背景是来自 K，π 弱衰变的 μ 子，通过背景 μ 子和粲夸克衰变的单 μ 子相对于初始对撞顶点的最接近距离（DCA）分布的不同来去除背景。

通过联合 TPC 测得的电离能损和 TOF 测得的粒子速度（β），电子可以被鉴别到 $p_T = 5$ GeV/c。电磁过程产生的电子本底通过重建标记电子（正电子）和所有伴随正电子（电子）的不变质量来在统计上减除。为了减少随机组合造成的背景，我们采用了二维重建不变质量的方法。伴随径迹的重建效率从 STAR 探测器模拟和蒙特卡罗样本分析中得到。这种方法可以减除约 95% 的电磁过程本底（光子转换和中性 π 介子达利兹衰变）。于是可以得到中心金金碰撞，最小偏置金金碰撞及其他中心度下的非电磁产生的电子横动量谱。另外，在本论文里我们也将讨论获取非电磁产生的电子的椭圆流（v_2）的方法。

联合以上三个独立的测量：RHIC 能区金金碰撞中的 $D^0 \rightarrow K\pi$ 强子衰变道，粲夸克衰变的单 μ 子和单电子谱，我们观测到中心金金碰撞中的非电磁产生的电子横动量

谱相对于氘金碰撞在横动量为 $0.9 \leq p_T \leq 5$ GeV/c 区间有很强的压低。在电子横动量约大于 2 GeV/c 区间，其相应的粲夸克强子横动量约大于 4 GeV/c，电子谱的压低程度与轻夸克重子和介子相似。基于 blast wave 模型，拟合横动量在 2 GeV/c 以下的电子谱给出的结果说明粲夸克强子与介质的相互作用和耦合可能不同于多奇异夸克强子和轻夸克强子。将来探测器升级后对粲夸克强子的直接重建将会给出更准确的答案。联合这三种独立的测量，可以可靠的给出粲夸克中心快度区的产生截面。这种方法覆盖了约 90% 的粲夸克运动学区间。200 GeV 中心金金碰撞中平均每核子对碰撞的粲夸克总产生截面的测量结果为：$1.40 \pm 0.11(stat.) \pm 0.39(sys.)$ mb。200 GeV 最小偏置金金碰撞中平均每核子对碰撞的粲夸克总产生截面的测量结果为：$1.29 \pm 0.12 \pm 0.36$ mb。测量结果表明粲夸克产生截面相对于两两碰撞数具有标度不变性。这说明硬过程对于初始核子中的两两相互作用具有标度性。而且证明粲夸克可以用来作为研究碰撞早期动力学机制的探针。

在以上的测量中，我们忽略了非电磁产生的电子谱里来自底夸克衰变的贡献。目前在实验得到的非电磁产生的电子谱中分离底夸克和粲夸克的贡献是相当困难的。理论模型预言的高能核碰撞中粲夸克和底夸克的产生的不确定性也很大。所以要更好的理解粲夸克物理，分离非电磁产生的电子谱中底夸克的贡献就相当的重要。在本论文的讨论部分，我们将介绍通过拟合非电磁产生的电子谱来估计底夸克的贡献。并且我们把模拟的电磁产生的电子椭圆流 v_2 与实验数据比较来估计可能的粲介子椭圆流 v_2。

Table of Contents

LIST OF FIGURES

16

List of Tables

CHAPTER 1

Introductions

1.1 Quantum ChromoDynamics

1.1.1 Confinement and asymptotic freedom

Quantum ChromoDynamics (QCD) [DKS03] is thought to be a correct theory of the strong nuclear force, one of the four fundamental forces of nature. It describe the strong interactions among quarks, which are regarded as fundamental constituents of matter, via their color quantum numbers. The strong interactions among quarks are mediated by a set of force particles known as gluons. Different from *Quantum ElectroDynamics* (QED) - the gauge theory describing electromagnetic interaction, QCD is based on the non-Abelian gauge group $SU(3)$, with gauge bosons (color octet gluons), and hence the gluons could have self-interacting. This results in a negative β-function and *asymptotic freedom* at high energies and strong interactions at low energies.

These strong interactions are confining: the self-coupled gluons strongly restrain the isolation of the quarks at large distance. There is no single quark as a color-triplet state observed experimentally. Only color-singlet bound states can propagate over macroscopic distances. The only stable color-singlets with size of the order of $1fm$ are quark−antiquark pairs, mesons, and three-quark states, baryons. At high energy reactions, like deep inelastic scattering, the quark and gluon constituents of hadrons act as quasi-free particles, partons. Such reactions can be factorized into the convolution of non-perturbative parton distribution functions, which cannot be calculated from first principles directly. But with process-dependent functions (*i.e. hard processes involving large momentum transfers*), the reactions can be calculated as perturbative expansions in the coupling constant α_s.

In QED, the electrodynamic coupling constant $\alpha = \frac{1}{137}$. However, due to the gluons self-interactions, the renormalized QCD coupling shows renormalization scale (μ) dependence [Alp02]. The running coupling $\alpha_s(\mu)$ can be written as:

$$\alpha_s(\mu) \equiv \frac{g_s^2(\mu)}{4\pi} \approx \frac{4\pi}{\beta_0 \ln(\mu^2/\Lambda_{QCD}^2)}, \qquad (1.1)$$

where g_s, which is strong charge in the gauge group, is the only parameter in the QCD Lagrangian besides the quark masses. β_0 (>0) is the first coefficient of the *beta*-function (renormalization neglects the higher orders). The strong force of the gluon-gluon self-coupling becomes smaller at shorter distance or with larger momentum transfers ($\alpha_s \rightarrow 0$ as $\mu \rightarrow \infty$), which is known as *asymptotic freedom*. In this case, QCD can be calculated perturbatively. Many experiments measured α_s at different scales. Since some of the precise measurements come from Z^0 decays, it has become universal to use $\alpha_s(M_z)$ as the label. The $\alpha_s(M_Z) = 0.1176 \pm 0.002$ [PDG04] comes from a fit to the experimental data, and the QCD scale $\Lambda_{QCD} \sim 200$ MeV. Fig. 1.1 shows the measured α_s at different momentum transfer scale μ compared with Lattice QCD calculations.

1.1.2 Nonperturbative QCD

Corresponding to the asymptotic freedom of QCD at high momentum scales (short distances), the running coupling becomes larger at lower momenta (longer distances). This effect is called *infrared slavery*. Eq. 1.1 shows strong coupling at $\mu \sim \Lambda_{QCD}$. Perturbation theory is not expected to be a reliable solution when α_s becomes large. Thus nonperturbative methods must be used to study the low-momentum, long-distance behavior of QCD.

A closely related phenomenon is *hadronization*. This term refers to the dynamical process in which a set of partons produced in a short-distance interaction reorganize themselves, possibly with the production of additional partons, to make the hadrons that are observed in the final state. This again is expected to be a low momentum transfer process, corresponding to the relatively long timescale over which hadron formation takes
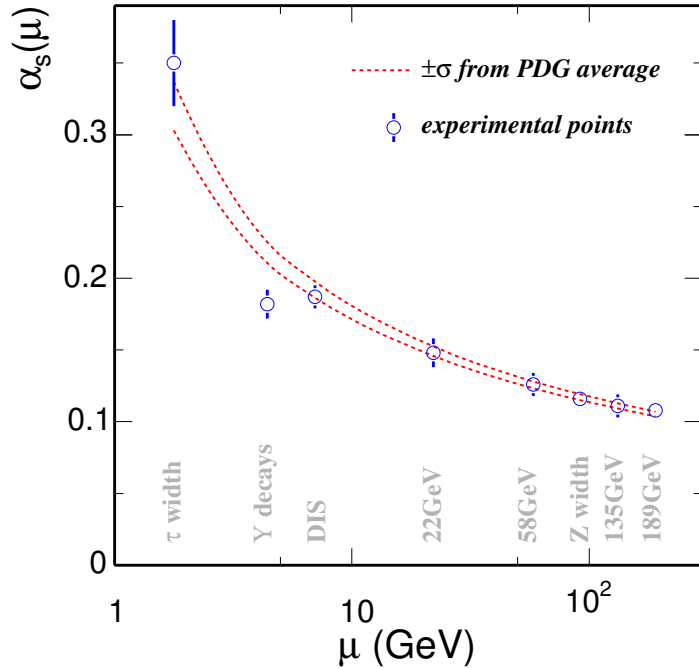
Figure 1.1: Measured QCD running coupling constant α_s from different experiments compared with Lattice QCD calculations.

place.

A nonperturbative approach that is widely used to study confinement is *lattice QCD* [Gup98]. The continuum field theory is replaced by one defined on a space-time lattice. As long as the size of the lattice elements inside a hadron is sufficiently small, hadronic properties and matrix elements should be reliably calculable on massively parallel computers.

1.1.3 Heavy quark masses and perturbative QCD (pQCD)

The masses of the heavy c quark and b quark ($m_c \sim 1.3$ GeV/c^2, $m_b \sim 4.75$ GeV/c^2) are almost exclusively generated through their coupling to the Higgs field in the electroweak sector, while the masses of light quarks (u, d, s) are dominated by spontaneous breaking of chiral symmetry in QCD. This means that in a *Quark-Gluon Plasma* (QGP), where chiral symmetry is expected to be restored, light quarks are left with their bare current masses while heavy-flavor quarks remain heavy. The heavy quark masses are not modified by the QCD vacuum [PDG04, Se04]. Hence once heavy quarks are pair-produced

in early stage via initial gluon fusions [Lin95] at high energy collision, their total number is conserved because the typical temperature of the subsequently evolutional medium is much smaller than the heavy quark masses. Therefore, heavy-flavor quarks are an ideal probe to study early dynamics in high-energy nuclear collisions, and their cross section can be evaluated by pQCD calculations.
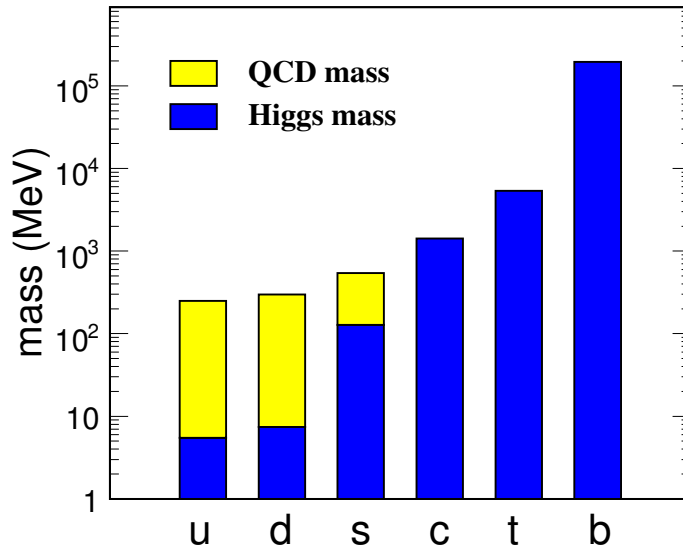
Figure 1.2: Masses of the six flavors. The masses generated by electroweak symmetry breaking (current quark masses) are shown as dark boxes; A large fraction of the light quark masses is due to the chiral symmetry breaking in the QCD vacuum (constituent quark masses), shown as light boxes. The numerical values were taken from Ref. [PDG04].

QCD is formulated in terms of quarks and gluons while the experimentally observed states are hadrons. As previously mentioned, in principal the method of perturbation theory is appropriate in the high-momentum scale, short-distance regime. It is known as the QCD factorization theorem [Css89, Col98] and states that for processes that have initial and/or observed final state hadrons the differential cross-section has the following form:

$$d\sigma(x, Q^2, m^2) = \prod_{h,h'} \sum_{i,f} f_{i/h}(x, \mu^2) \otimes d\hat{\sigma}_{i \to f}(x, Q^2, m^2, \mu_r^2, \mu_F^2) \otimes D_{h'/f}(x, \mu^2) + \mathcal{O}(\Lambda/Q),$$

(1.2)

where the factor $f_{i/h}$ stands for the *Parton Distribution Function* (PDF) of the parton i inside the hadron h present in the initial state, and Q and x represent the hard scale and some kinematical variable respectively. The parton distributions depend on the factorization/renormalization scale μ^2. The second factor $d\hat{\sigma}_{i \to f}$, also known as the (Wilson) coefficient function, represents the partonic hard scattering cross section for the reaction $i \to f$ that depends on the unphysical renormalization and factorization scales μ_r^2 and μ_F^2 and on the masses of the heavy quarks m^2. The last factor D is the so called *Fragmentation Function* (FF). It contains the information for the hadronization of the hard parton f (that is produced in the hard process described by the partonic cross-section $d\hat{\sigma}$) into an observed hadron h'. Since the concepts of parton distributions and hadronization are only for the initial and final states of hadrons, lepton-nucleon *Deep Inelastic Scattering* (DIS) and high energy e^+e^- collisions are performed to measure PDFs and FFs, respectively.

The large masses ($\gg \Lambda_{QCD}$) of the heavy quarks, which are 'hard' scales, make perturbative QCD applicable [Vog02]. Asymptotic freedom is assumed in calculating the interactions between two heavy hadrons on the quark/gluon level but the confinement scale determines the probability of finding the interacting parton in the initial hadron. Factorization assumes that between the perturbative hard part and the full expansion, non-perturbative parton distribution functions are applied. The integral hadronic cross section in an AB collision where $AB = pp, pA$ or nucleus-nucleus can be written as:

$$\sigma_{AB}(S, m^2) = \sum_{i,j=q,\bar{q},g} \int_{4m_Q^2/s}^1 \frac{d\tau}{\tau} \int dx_i dx_j \delta(x_i x_j - \tau) f_i^A(x_i, \mu_F^2) f_j^B(x_j, \mu_F^2) \hat{\sigma}_{ij}(s, m^2, \mu_F^2, \mu_R^2),$$

(1.3)

where f_i^A and f_i^B are the nonperturbative PDF determined from experiments, x_i and x_j are the fractional momentum of hadrons A and B carried by partons i and j, $\tau = s/S$, s is partonic center of mass energy squared, $\hat{\sigma}_{ij}(s, m^2, \mu_F^2, \mu_R^2)$ is hard partonic cross section, which only depends on quark mass m, not kinematic quantities, can be calculated in QCD in powers of α_s^{2+n}, known as *leading order* (LO), $n = 0$; *next-to-leading order* (NLO), $n = 1$

.... Eq. 1.4 express the partonic cross-section to NLO:

$$\hat{\sigma}_{ij}(s, m^2, \mu_F^2, \mu_R^2) = \frac{\alpha_s^2(\mu_R^2)}{m^2}\{f_{ij}^{(0,0)}(\rho) + 4\pi\alpha_s(\mu_R^2)[f_{ij}^{(1,0)}(\rho) + f_{ij}^{(1,1)}(\rho)\ln(\mu_F^2/m^2)] + \mathcal{O}(\alpha_s^2)\},$$
(1.4)

where $\rho = 4m^2/s$, μ_F is factorization scale which separates hard part from nonperturbative part, μ_R is renormalization scale, at which the strong coupling constant α_s is evaluated. $\mu_F = \mu_R$ is assumed in evaluations of parton densities, and $f_{ij}^{(a,b)}$ are dimensionless, μ−independent scaling functions. For LO, $a = b = 0$ and $ij = q\bar{q}$, gg. For NLO, $a = 1$,$b = 0, 1$ and $ij = q\bar{q}, gg$ and $qg, \bar{q}g$. $f_{ij}^{(0,0)}$ are always positive, $f_{ij}^{(1,b)}$ can be negative. If $\mu_F^2 = m^2$, $f_{ij}^{(1,1)}$ does not contribute. Results of theoretical calculations strongly depend on quark mass, m, factorization scale, μ_F, in the parton densities and renormalization scale, μ_R, in α_s, *etc.* [MNR93, Vog02, RP03].

1.1.4 Deconfinement, equation of state and QCD phase

Currently, the isolated quark has never been observed. Quarks and gluons are confined in QCD matter as hadron gas. If the temperature and energy density of the matter are sufficiently high, the strong force among quarks and gluons may be greatly reduced. Thus quarks and gluons could be deconfined from hadrons and become disengaged with large distance among them in that hot and dense condition. This phenomenon is called *deconfinement*. The deconfinement indicates a phase transition from a hadron gas to a new deconfined form of matter – the QGP, which is formed by these dissociative quarks and gluons with new (color) *degree of freedom* (d.o.f). In the QGP phase, the broken chiral symmetry will be restored. The evolution of energy density and pressure with temperature from Lattice QCD calculations illustrate the phase transition [KLP00], see Fig. 1.3.

Large increase of degrees of freedom at T_c is seen in the rapid change in energy density and pressure. The critical temperature is predicted to be $T_c \sim 150 - 180$ MeV, and the energy density at the critical point is $\varepsilon_c(T_c) \sim 1 - 3$ GeV/fm^3 (~ 0.17 GeV/fm^3 for nuclear matter) [Kar02b]. The arrows indicate the *Stefan-Boltzmann* (SB) limits,
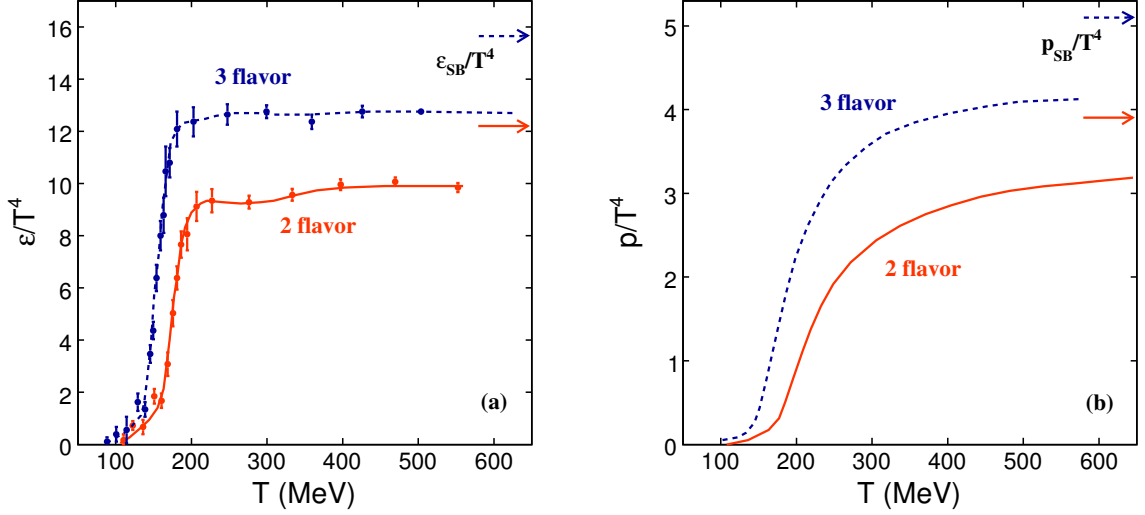
Figure 1.3: The evolution of ε/T^4 (a) and p/T^4 (b) with the increase of temperature T for 3 flavor and 2 flavor configurations. The arrows indicate the SB limit for each case.

applicable for the systems with massless, non-interacting quarks and gluons. The similar deviation of the curves from the SB limits indicates that besides the effect of quark masses, the quasiparticles, which form the new matter, must interact with one another. The various heavy-ion experiments devoted to the creation and detection of new forms of highly excited matter also indicate that, at the reachable energy scales, the produced phase exhibits a strong collective behavior (see next section). All these theoretical predictions and experimental observations are incompatible with a weakly interacting QGP.

Based on local 4-momenta conservation and other conserved currents (e.g. baryon number),

$$\partial_\mu T^{\mu\nu} = 0, \qquad \partial_\mu j^\mu = 0, \tag{1.5}$$

from the *Hydrodynamic* model, the equations of relativistic ideal hydrodynamics are

$$j^\mu(x) = n(x)u^\mu(x), \tag{1.6}$$

$$T^{\mu\nu} = [\varepsilon(x) + p(x)]u^\mu u^\nu - g^{\mu\nu}p(x), \tag{1.7}$$

where $\varepsilon(x)$ is the energy density, $p(x)$ is the pressure, $n(x)$ is the conserved number

density, and $u^\mu(x) = \gamma(1, v_x, v_y, v_z)$ with $\gamma = 1/\sqrt{1-v_x^2-v_y^2-v_z^2}$ is the local four velocity of the system.

Eq. 1.5 contains 5 equations for 6 unknown fields $\varepsilon, n, p, v_x, v_y, v_z$. To fully describe the system one needs an *equation of state* (EOS), which relates pressure, energy and baryon density. The thermal condition of the system can be fixed by pressure, p and temperature, $T(\varepsilon)$. The EOS, which describes the system response to changes of the thermal condition, is separately constructed for a relativistic ideal QGP phase (dashed line in Fig. 1.4), $\partial p/\partial \varepsilon = \frac{1}{3}$, and a hadron resonances gas (dotted line), $\partial p/\partial \varepsilon \sim \frac{1}{6}$. By combining these two EOSs, the EOS indicates the phase transition (solid line) can be obtained from Maxwell construction with a bag constant B. Here B is tuned to the desired phase transition temperature: $B^{1/4} = 230$ MeV gives $T_c(n = 0) = 164$ MeV at vanishing net baryon density.
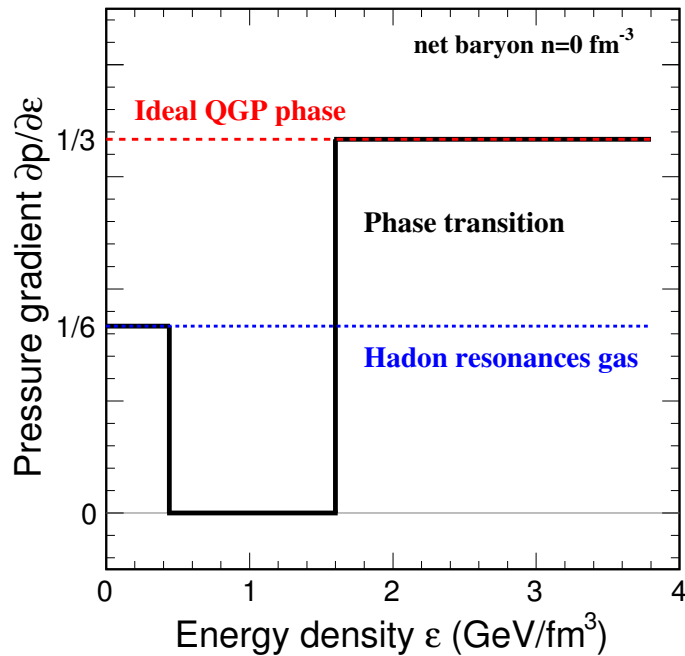
Figure 1.4: Equations of state for ideal QGP phase, hadron resonances gas and phase transition at vanishing net baryon density.

1.2 Relativistic Heavy Ion Collisions

With very high energy density and temperature in a bulk system, the new QGP phase of matter is predicted to be formed by the deconfined quarks and gluons. In order to search for the production of QGP matter and to study its properties, relativistic heavy-ion collisions have been performed to provide the hot and dense environment under laboratory conditions. The Relativistic Heavy Ion Collider (RHIC) at Brookhaven National Laboratory is built to create and search for this novel form of matter by colliding Au ions at energies up to $\sqrt{s_{\mathrm{NN}}}$=200 GeV.

In relativistic heavy-ion collisions, due to the Lorentz contraction in the moving direction, the collision geometry between the two nuclei behaves as two thin disks approaching each other nearly with speed of light. The heavy-ion collisions can be approximated as the interpenetrating collisions of their constituent nucleons with partonic interactions at high energy. The number of participating nucleons and the produced particle multiplicities in the final hadron state can be calculated by the Glauber model which relates these quantities to the size of the impact parameter, b, which is defined as the distance between the perpendicular bisectors along the colliding direction of the two ions. The impact parameter is large for peripheral collisions, consisting of a small number of participants and small multiplicities. A central collision occurs when the impact parameter is small. Only central collisions of two heavy nuclei at high energies are expected to provide a sufficiently hot and dense environment to produce the QGP. In central heavy-ion collisions, with sufficient interactions of the partons, the chemical and local thermal equilibrium of the quark-gluon system could be reached and thus the QGP forms. At the initial stage of the collision with the primary hard scattering, high p_T jets, heavy quark pairs, direct photons, *etc.* are created due to large momentum transfers. Due to high energy densities and pressure gradients, the QCD system expands and cools down. The partons can hadronize to mesons and baryons via inelastic interactions. When the chemical freeze-out point (temperature) is reached, the inelastic interactions will stop, and the relative particle yields will not change. After that, the elastic interactions re-distribute the transverse

momenta among hadrons. The particle kinetic freeze-out point (temperature) will occur after the elastic interactions stop.

1.2.1 Energy loss and jet quenching

Particle yields will change due to energy loss in the strong interacting medium created in nuclear-nuclear collisions. These modifications of high p_T particle yields can be used as unique tools to study the medium properties. Experimentally, the widely used observable quantity of particle energy loss is called the nuclear modification factor R_{AB}, which is defined as the ratio of the spectra in $A + B$ collisions and those in $p+p$ collisions, scaled by the number of binary nuclear-nuclear collisions [Adl02a]:

$$R_{AB}(p_T) = \frac{d^2 N^{AB}/dp_T d\eta}{T_{AB} d^2 \sigma^{pp}/dp_T d\eta}, \qquad (1.8)$$

where $T_{AB} = \langle N_{bin} \rangle / \sigma^{pp}_{inel.}$ accounts for the nuclear overlap geometry, averaged over the measured centrality class [Won94]. $\langle N_{bin} \rangle$ is the equivalent number of binary collisions calculated from the Glauber model.

As presented in Fig. 1.5 (a), high p_T suppression of N_{bin} scaled hadron production in central Au+Au collisions relative to $p+p$ collisions has been observed in RHIC experiments at $\sqrt{s_{\text{NN}}}$=200 GeV. This is considered as evidence for the energy loss of the energetic partons, high p_T jets interacting with the hot and dense medium created in central Au+Au collisions at RHIC [Ada03b]. Due to the absence of nuclear effects such as shadowing [EKS98, DFS03, Kop03, Vogt04], the Cronin effect [Acc04, Cat04, BPLF04], *etc.*, hard processes are expected to scale with the number of binary collisions ($R_{AB} = 1$). Thus the nuclear suppression phenomenon was not seen in d+Au collisions. The enhancement in the intermediate p_T region for R_{dAu} is due to the Cronin effect. The consistent picture of away-side jet quenching has also been observed in dihadron azimuthal angle correlations. Fig. 1.5 (b) shows the associated hadron ($2<p_T<p_T(trig)$ GeV/c) azimuthal distribution relative to a triggered hadron ($4<p_T<6$ GeV/c) after subtraction of the elliptic flow and pedestal contributions. The enhanced correlation at near-side ($\Delta\phi \sim 0$),

which means the pair is from a single jet, was observed in $p+p$, $d+$Au and Au+Au collisions. The pair from the back-to-back jet correlation at away-side ($\Delta\phi \sim \pi$) in central Au+Au collisions shows a dramatic suppression relative to those in $p+p$ and $d+$Au collisions [Ada03b, Wan04].
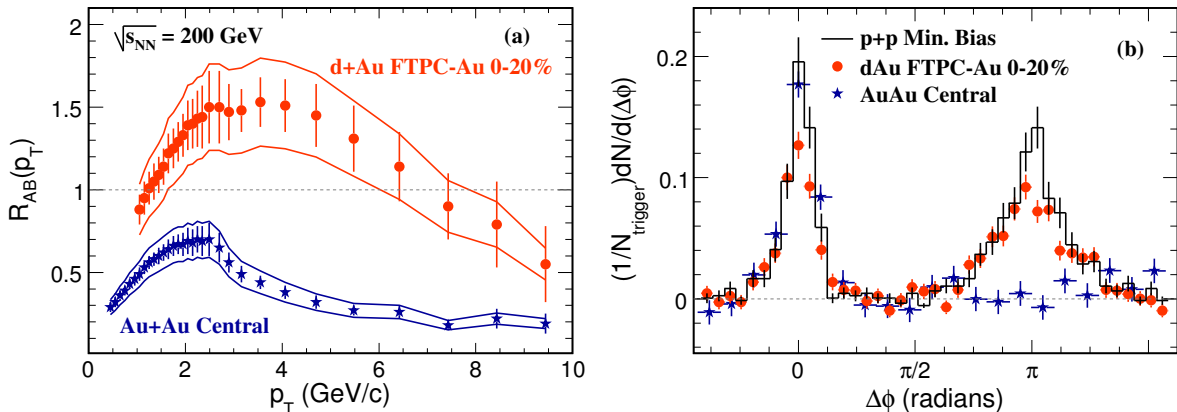
Figure 1.5: Panel (a): $R_{AB}(p_T)$ for minimum bias and central $d+$Au collisions and central Au+Au collisions. The bands show the normalization uncertainties. Panel (b): Two particle azimuthal distributions in $p+p$, $d+$Au and central Au+Au collisions.

All these high p_T suppression or away-side jet quenching observations indicate that light quarks strongly lose energy in the interacting dense medium. However, due to their large quark mass and small gluon radiative angle, heavy quarks are predicted to lose less energy compared to light quarks since pQCD energy-loss calculation assumes only gluon radiation [DK01, DGW05, Arm05]. The finite mass generalization of the small x (soft radiation $x \ll 1$) invariant DGLAP radiation spectrum is given by

$$\omega\frac{dN_g^{(0)}}{d^3\vec{k}} \simeq \frac{C_R\alpha_s}{\pi^2}\frac{k^2}{(k^2 + m_g^2 + x^2M^2)^2},\qquad(1.9)$$

where $\omega(k)$ is the energy carried by radiated gluons in the medium with momentum k, and α_s is the strong coupling constant. The color charge factor $C_R = \frac{N_c^2-1}{2N_c} = \frac{4}{3}$ with the number of color flavor $N_c = 3$ in this case. The gluon radiation angle is defined as $\theta_c \equiv \sqrt{m_g^2 + x^2M^2}/(xE)$. Due to large quark mass M, the gluon radiation is suppressed at smaller angles $\theta<\theta_c$. This effect is known as the "dead cone" phenomenon.

From study on the non-abelian analog of the *Ter-Mikayelian* plasmon effect for gluons
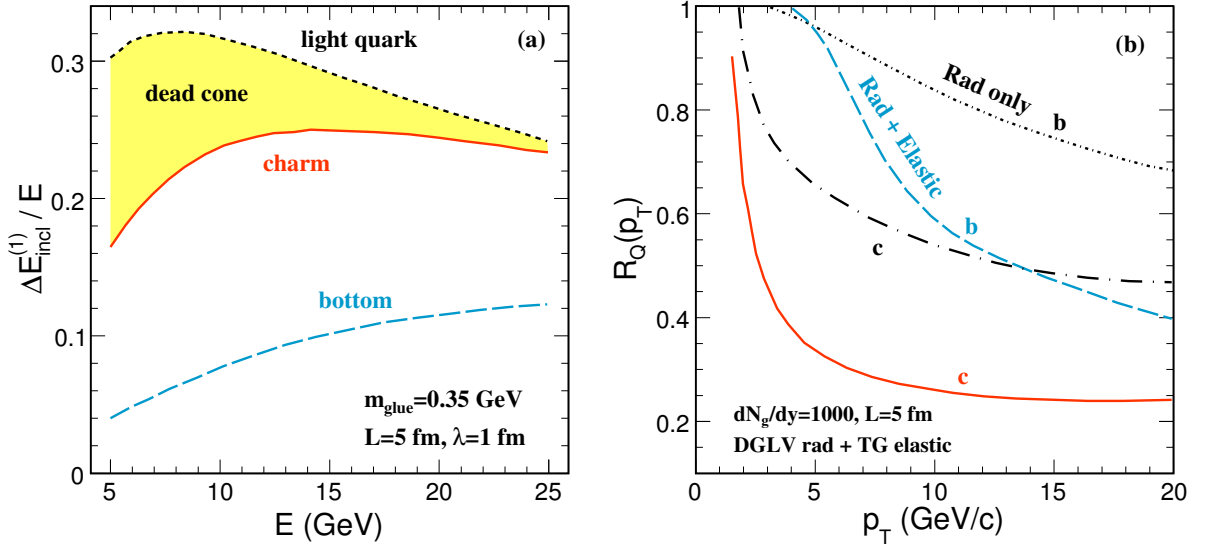
Figure 1.6: Panel (a): The 1st order in opacity fractional energy loss for heavy quarks is shown as a function of their energy in a plasma characterized by α_s=0.3, Debye mass μ=0.5 GeV, and $L = 5\lambda = 5$ fm. Panel (b): Heavy quark nuclear modifications as a function of p_T for fixed $L = 5$ fm and $dN_g/dy = 1000$. Short- (bottom) and long- (charm) dot-dashed curve include only radiative energy loss, while dashed (bottom) and solid (charm) curve include elastic energy loss as well.

and the extended GLV energy loss method, the heavy quark energy loss to first order in the opacity, L/λ_g (L is the path length, λ_g is the gluon mean free path), are numerically estimated as the solid curves (charm) and long-dashed curve (bottom) shown in Fig. 1.6 (a), which is much less than light quarks (short-dashed curve). The shaded area indicates the so called "dead cone" effect.

However, recent measurements of the p_T distributions and nuclear modification factor for the non-photonic electrons (presumably from heavy quark decays) at high p_T show similar suppression to those from light hadrons [STACRAA, PHECRAA], see Fig. 1.7. This renews the interest in understanding the heavy quark energy loss mechanism in central Au+Au collisions at RHIC. From theoretical calculations, which take elastic (collisional) energy loss into account, the nuclear modifications of heavy quarks are expected to have larger suppression compared to those with only radiative energy loss [Wic05], see Fig. 1.6 (b). Accounting for elastic energy loss seems to produce good agreement with experiments for heavy flavor energy loss, but this prescription fails in the case of light
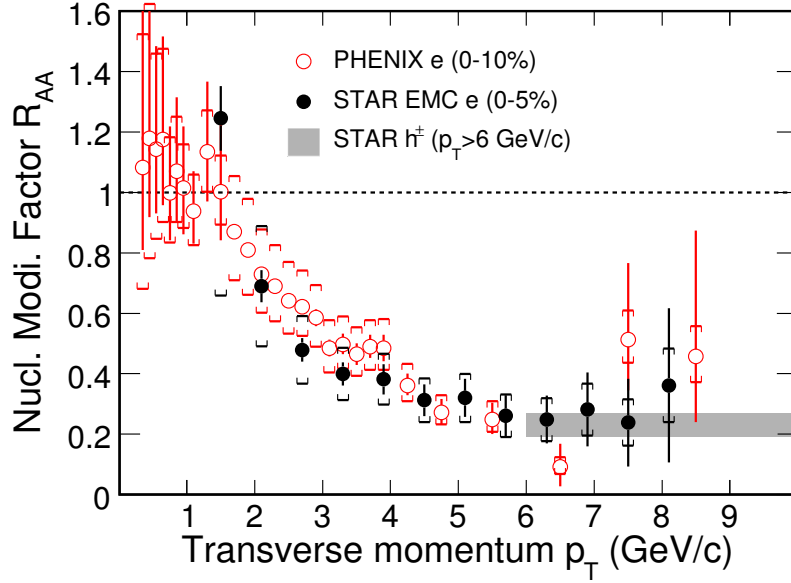
Figure 1.7: Nuclear modification factors of non-photonic electron from PHENIX (open circle) and STAR (solid circle) are suppressed in similar magnitude with light flavor hadrons (grey band).

flavors. These will be discussed in more detail in chapter 5.

1.2.2 Collective motion and freeze-out

The measured hadron spectra, especially in the soft sector at transverse momenta $p_T \lesssim 1.5$ GeV/c, reflect the properties of the bulk of the matter produced in heavy-ion collisions after elastic interactions have stopped among the hadrons at kinetic freeze-out. At this stage the system is already relatively dilute and "cold". However, from the final state hadron spectra at kinetic freeze-out, one can obtain the information about the earlier hotter and denser stage. Since different hadrons have different production (hadronization) mechanisms, the characteristics of the different stages of the collision systems can be explored by analysis of the transverse momentum distributions for various hadron species. Fig. 1.8 (a) shows the measured m_T ($\equiv \sqrt{p_T^2 + mass^2}$) spectra for light hadrons (π, K, p), Λ, Ξ and multi-strange hadrons (Φ, Ω) in 200 GeV central Au+Au collisions [Ada04a, Ada04b, Ada04c, Cas04], and charmed hadron (D^0) [YF06] in 200 GeV minimum bias Au+Au collisions (will be discussed in Chapter 4).

13
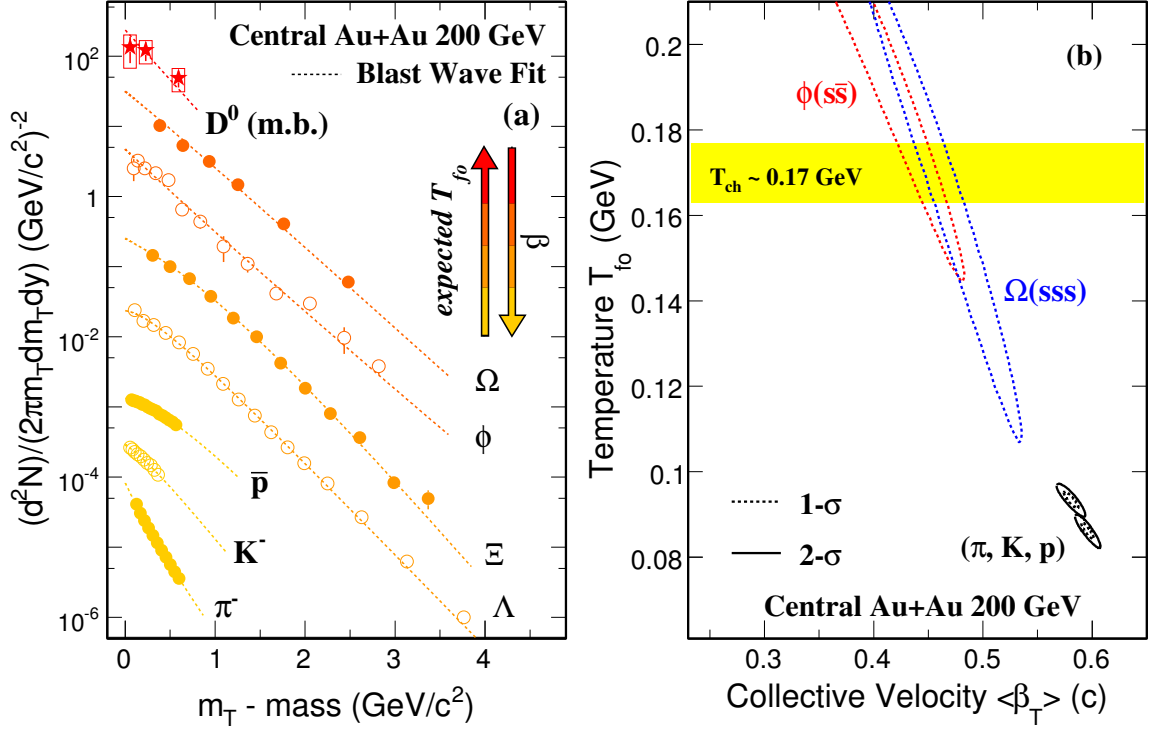
Figure 1.8: Panel (a): The m_T spectra for light hadrons (π, K, p), Λ, Ξ and multi-strange hadrons (Φ, Ω) in 200 GeV central Au+Au collisions, and charmed hadron (D^0) in 200 GeV minimum bias Au+Au collisions are shown in symbols. The Blast Wave fit results are shown in curves. The BW fit for D^0 was done by combining D^0 spectrum and the measured charm decay leptons spectra below 2 GeV/c. The BW fits were done for π^-, K^-, $\bar{p}$ simultaneously and for other particles separately. The arrows show the expected increasing freeze-out temperature and decreasing collective velocity from bottom to top. Panel (b): Blast-wave parameters T_{fo} vs. $\langle \beta_T \rangle$ contour plot from the simultaneous fits to light hadrons (π, K, p) spectra in 5-10% and 0-5% Au+Au collisions and separate fits to multi-strange hadrons $\phi(s\bar{s})$, $\Omega(sss)$ spectra in 0-10% central Au+Au collisions.

14

In the Blast Wave thermal model [SSH93], local thermal equilibrium is assumed and only particle mass and temperature of the system modify particle transverse momentum. After the collision, the bulk system expands and becomes more and more dilute and cold, while the particle collective velocity develops larger and larger. Extraction of model parameters characterize the random, generally interpreted as a kinetic freeze-out temperature T_{fo} and collective, radial flow velocity $\langle \beta \rangle$, aspects. Fig. 1.8 (b) shows the fit parameters T_{fo} versus $\langle \beta \rangle$ for different particles in central Au+Au collisions. Simultaneous fit results for light hadrons (π, K, p) give large flow velocity and small freeze-out temperature in central collisions, indicating that light hadrons kinetically freeze out late with strong collectivity when system evolutes a more rapid expansion after chemical freeze-out. Compared to light hadrons, the larger temperature and smaller flow velocity obtained from the fits indicates that multi-strange hadrons freeze out at earlier stage during the evolution of the bulk system. Since multi-strange hadrons are expected to have smaller hadronic scattering cross sections and their transverse momentum distributions will not change significantly after chemical freeze-out, the kinetic freeze-out temperature from the fit to those particles is consistent with the chemical freeze-out temperature T_{ch}, albeit with still large uncertainties. The chemical freeze-out temperature T_{ch} is close to the critical temperature T_c, indicating the temperature of the system created in the collisions is greater than T_c and hence the phase transition may take place and QGP may form at RHIC energy of $\sqrt{s_{\mathrm{NN}}}$=200 GeV.

Due to relatively heavy quark mass and much smaller hadronic scattering cross section, heavy flavor hadrons are expected to freeze-out early and difficultly participate in collective motion. Thus the larger freeze-out temperature and smaller flow velocity are expected for heavy flavor hadrons. But currently the experimental statistics is not good enough to distinguish the freeze-out properties between D-meson and multi-strange hadrons, this will be discussed in chapter 5.

1.2.3 anisotropic flow

Recent heavy-ion collisions experiments at RHIC have successfully generated a lot of exciting results. Besides strong suppression of particles with high momentum created in the collisions - jet quenching, the large azimuthal anisotropy - elliptic flow is one of the most remarkable discoveries. All observations indicate that the extremely opaque quark-gluon matter formed in the collisions exhibits highly collective, near-hydrodynamic behavior [KH03]. In non-central heavy-ion collisions, the initial coordinate spacial anisotropy, which is formed by the geometrical overlap of the two nuclei, will produce anisotropic pressure gradients in the high dense matter which then subsequently produce a final-state momentum space anisotropy of the produced particles via rescattering. Because of the self-quenching of coordinate space anisotropy, the measurement of the particle azimuthal anisotropy distributions with respect to (w.r.t) the reaction plane can reveal the information on the dynamics at the early stage of the collision.

The initial space anisotropy in the overlapping region (x,y), which is the plane transverse to the beam axis z, is characterized by the eccentricity:

$$\varepsilon = \frac{\langle y^2 - x^2 \rangle}{\langle y^2 + x^2 \rangle} \tag{1.10}$$

The final particle spectrum in momentum space can be expanded into a Fourier expression in terms of particle azimuthal ϕ distributions w.r.t the reaction plane Ψ_r:

$$E\frac{d^3N}{dp^3} = \frac{d^2N}{2\pi p_T dp_T dy}(1 + \sum_{n=1}^{\infty} 2v_n cos[n(\phi - \Psi_r)]), \tag{1.11}$$

The Fourier coefficients represent anisotropy parameters and can be extracted as

$$v_n = \langle cos[n(\phi - \Psi_r)]\rangle, \tag{1.12}$$

where the first and second coefficients v_1, v_2 are called the directed and elliptic flow.

The identified particle elliptic flow v_2 shows strong transverse momentum dependence.

In the low p_T region, particle collective motion shows hydrodynamical behavior [KH03, Ada05]. As is well known, hydrodynamic models, which assume ideal relativistic fluid flow and negligible relaxation time compared to the time scale of the equilibrated system, successfully reproduce the experimental data and reasonably describe the mass ordering for v_2 at low p_T. Thus the particle v_2 follows $m_T - m$ scaling [Yan07], as shown in Fig. 1.9 (a). Here $m_T \equiv \sqrt{p_T^2 + m^2}$ and m is the particle mass. On a $m_T - m$ scale, at intermediate p_T (1.5 GeV/c < p_T < 4 GeV/c), the particle v_2 is split into meson and baryon groupings, and this phenomenon may be described by coalescence/recombination models [LK02, MV03]. In these models, mesons and baryons are hadronized by coalescing two and three co-moving quarks, respectively. The simple picture is that the hadron v_2^h can be described by its constituent quark v_2^q as:

$$v_2^h(p_T) \simeq n_q v_2^q(p_T/n_q), \quad n_q(meson) = 2, \quad n_q(baryon) = 3, \quad (1.13)$$

where n_q is the number of constituent quarks. Thus, v_2 may follow the *Number-of-Quark* (NQ) scaling. This scaling behavior is observed in Au+Au collisions at RHIC. Fig. 1.9 (b) shows the scaling of identified particle v_2 divided by n_q as a function of $(m_T - m)/n_q$. These exciting results are considered as indicators for the observation of the partonic level collectivity (deconfinement) in heavy-ion collisions at RHIC energies.

1.2.4 Charm production at RHIC

Charm quarks are a unique tool to probe the partonic matter created in relativistic heavy-ion collisions at RHIC energies. Because of their large quark mass ($\simeq 1.3$ GeV/c^2), charm quarks are predicted to lose less energy compared to light quarks when pQCD energy-loss calculation assumes only gluon radiation [DK01, DGW05, Arm05]. Recent measurements of the p_T distributions and nuclear modification factor for the non-photonic electrons (presumably from heavy quark decays) at high p_T show similar suppression to those from light hadrons [STACRAA, PHECRAA]. This renews the interest in understanding the picture of the observed jet-quenching phenomena at the partonic stage in
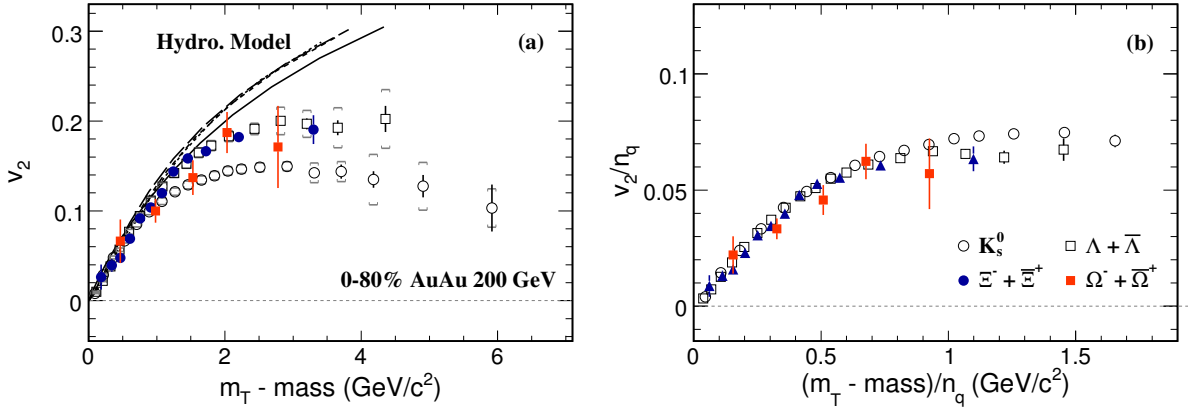
Figure 1.9: Panel (a): Identified particle v_2 as a function of $m_T - m$ in 0-80% Au+Au collisions at $\sqrt{s_{NN}}$=200 GeV. Open circles, open squares, solid triangles and solid circles represent K_s^0, $\Lambda + \bar{\Lambda}$, $\Xi + \bar{\Xi}$ and $\Omega + \bar{\Omega}$, respectively. Hydrodynamic calculations are shown as curves for comparison. Panel (b): Identified particle v_2 scaled by the number of constituent quarks (n_q) versus $(m_T - m)/n_q$.

Au+Au collisions at RHIC. Furthermore, theoretical calculations have shown that interactions between the surrounding partons in the medium and charm quarks could change the measurable kinematics[MT05, HGR06, DDZ06], and could boost the radial and elliptic flow resulting in a different charm p_T spectrum shape. Due to its heavy mass, a charm quark can acquire flow from the interactions with the constituents of a dense medium in analog to Brownian motion. Its decoupling from medium also depends on the cross-section of the interaction and medium density. Therefore, the measurement of charm flow and freeze-out properties is vital to test light flavor thermalization and the partonic density in the early stage of heavy ion collisions [Xu03, LM03, GKR04, MT05, BKG03]. The charmed hadron kinetic freeze-out temperature T_{fo} and the radial flow velocity β can be derived from blast-wave model [SSH93] fits to data.

These postulations and predictions are based on the assumptions that charm quarks are produced only at early stages via initial gluon fusion and that their production cross-section can be calculated by perturbative QCD [Lin95, CNV05]. Study of the binary collision (N_{bin}) scaling properties for the total charm cross-section from d+Au to Au+Au collisions can test these assumptions and determine if charm quarks are indeed good probes with well-defined initial and final states. Charm total cross-section measurement

is also essential for model calculations, which tries to explain observed similar suppression pattern of J/Ψ at RHIC and SPS [Pbm00, ABR03, GR01, Kos02, TSR01, GKL02]. It has been shown that low p_T muons and intermediate p_T electrons from charmed hadron semileptonic decays can stringently constrain the charm total cross-section and are sensitive to the radial flow and the freeze-out condition [LZZX06].

1.2.5 Bottom contribution in non-photonic electron measurements

Due to the absence of the measurement of B-mesons and precise measurement of D-mesons, it is difficult to separate bottom and charm contributions experimentally in current non-photonic electron measurements for both spectra and elliptic flow v_2. As discussed previously, the suppression behavior of heavy quarks is quite different from light quarks due to the "dead cone" effect [DK01], and this is especially true for the bottom quark. Even when the elastic energy loss is included, the bottom quark still loses much less energy. The bottom contribution may reduce the energy loss of non-photonic electrons from heavy flavor decays. But as shown in Fig. 1.10 (a), the suppression of the non-photonic electron R_{AA} is as large as light hadrons. Both the theoretical result with charm energy loss only and the theoretical calculations with charm+bottom energy loss by assuming large $\hat{q}$ or counting elastic energy loss can describe the data within errors [DGV06, Wic05, Rap06, Vit06, Arm06].

Recently, PHENIX has measured the non-photonic electron v_2 [SS07], shown in Fig. 1.10 (b). The observed large elliptic flow of the non-photonic electron may indicate strong coupling of heavy quarks with medium. There are many theoretical calculations for the non-photonic electron v_2, such as charm thermal+flow model (solid curve) [GKR04], A multiphase transition (AMPT) model assume cross section σ_p=10 mb (dashed curve) [ZCK05], resonance states of D-/B- mesons (band) [HGR06], *etc*. The comparison with theories also showes that both the model results with charm only and the results with charm+bottom have good agreement with data within errors.

Thus, the puzzle of the bottom contributions in non-photonic electron spectra and v_2
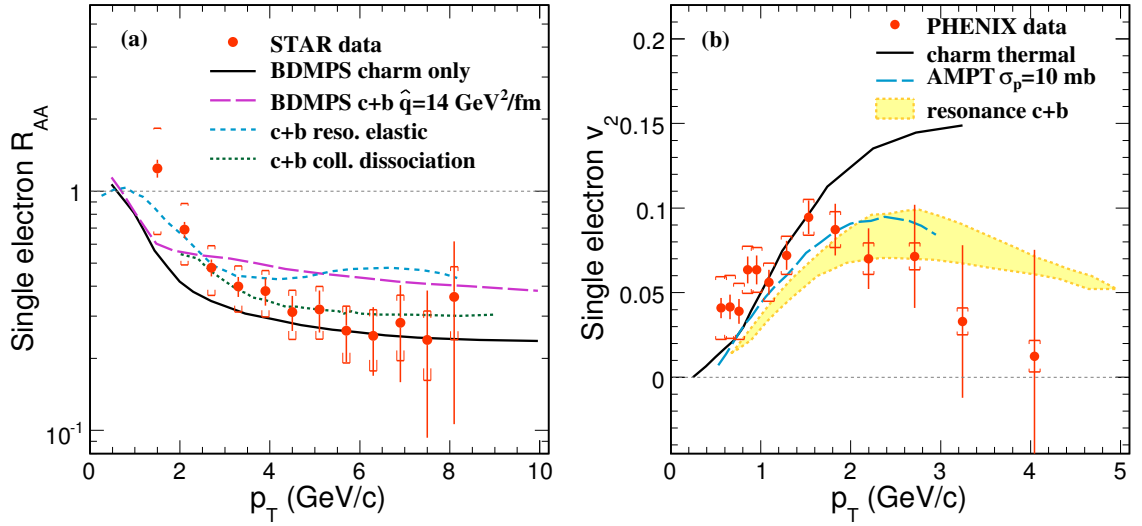
Figure 1.10: Panel (a): Non-photonic electron R_{AA} measured from STAR (circle) compared to theories. Panel (b): Non-photonic electron v_2 measured from PHENIX (circle) compared to theories.

still remains. We will have a detail discussion about this issue in chapter 5.

CHAPTER 2

Experimental Set-up

2.1 The RHIC accelerator

The Relativistic Heavy Ion Collider (RHIC) located at Brookhaven National Laboratory (BNL) is built to accelerate and collide heavy ions and polarized protons with high luminosity. The RHIC accelerator facility consists of two concentric storage rings, called blue and yellow rings, sharing a common horizontal plane in the tunnel. The superconducting magnets in each ring with a circumference of 3.8 km are designed to bend and focus the ion beams. The counter-rotating beams can collide with one another at six location along their 3.8 km circumference. The top center-of-mass collision energy for heavy ion beams is 200 GeV per nucleon pair. The operational momentum increases with the charge-to-mass ratio, resulting in the top energy of 125 GeV/u for lighter ion beams and up to 250 GeV/u for polarized proton beams. The average luminosity for gold-on-gold collisions at $\sqrt{s_{\mathrm{NN}}}=$ 200 GeV is $8 \times 10^{26} cm^{-2} s^{-1}$ without electron cooling and $7 \times 10^{27} cm^{-2} s^{-1}$ with electron cooling.

Fig. 2.1 shows the RHIC accelerator complex including the accessorial accelerators used to bring the ions beams up to RHIC injection energy, and strip electrons from the atoms. Negatively charged gold ions are partially stripped of their electrons and then accelerated to 15 MeV/u in the Tandem Van de Graaff facility. After a charge selection by bending magnets, beams of gold ions are transferred to the Booster Synchrotron and accelerated to 95 MeV/u through the Tandem-to-Booster line. Then the gold ions are injected into the Alternating Gradient Synchrotron (AGS) and accelerated to 10.8 GeV/u. The beams are transferred to RHIC through the AGS-to-RHIC Beam Transfer Line.

Finally, beams are injected to RHIC and fully accelerated to the top collision energy 100 GeV/nucleon. For $p+p$ collisions, proton beams are injected from the 200 MeV Linac into the booster, followed by acceleration in the AGS and injection into RHIC.
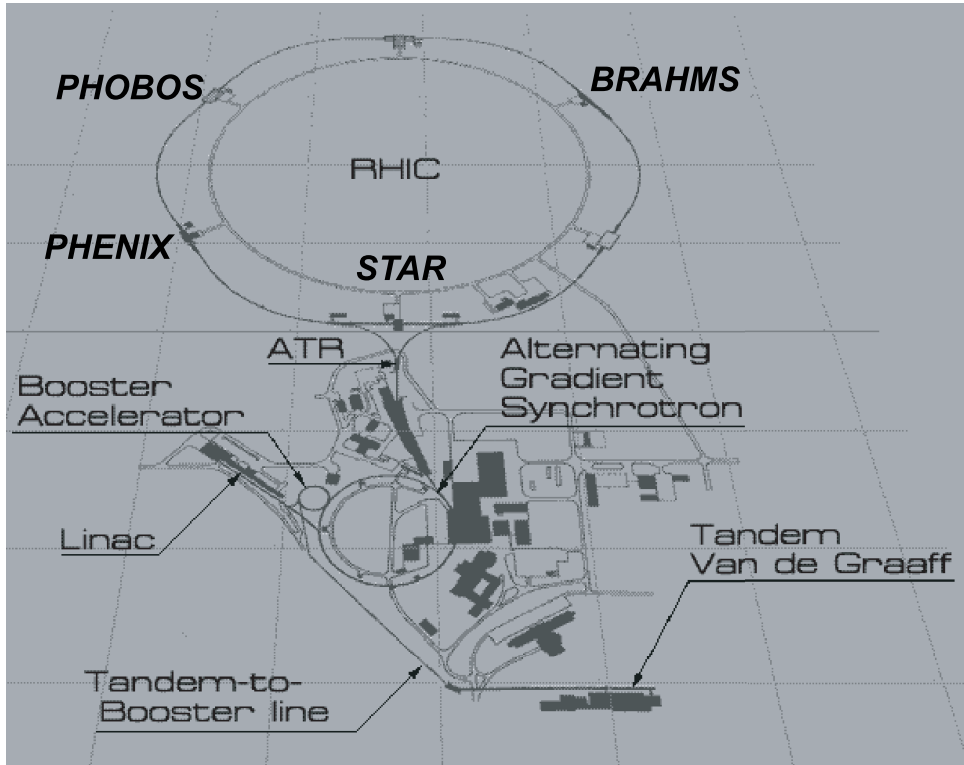
Figure 2.1: Schematic of the RHIC complex. RHIC's two 3.8-kilometer rings collide relativistic heavy ions and polarized protons at six intersection points.

There are six interaction points along the rings, and 4 of them are equipped with detectors. They are two large experiments STAR (6 o'clock), PHENIX (8 o'clock) and two small ones PHOBOS (10 o'clock) and BRAHMS (2 o'clock), respectively.

2.2 The STAR detector

To investigate the behavior of strongly interacting matter at high energy density and to search for signatures of the new matter form of QGP, The Solenoidal Tracker at RHIC (STAR) was specially constructed for measurements of hadron production over a large solid angle with high precision tracking, high quality momentum, and good particle identification capability. It has an azimuthal symmetric acceptance and covers large range

around mid-rapidity. STAR consists of several subsystems and a main tracker - the *Time Projection Chamber* (TPC) located in a homogenous solenoidal analyzing magnet.
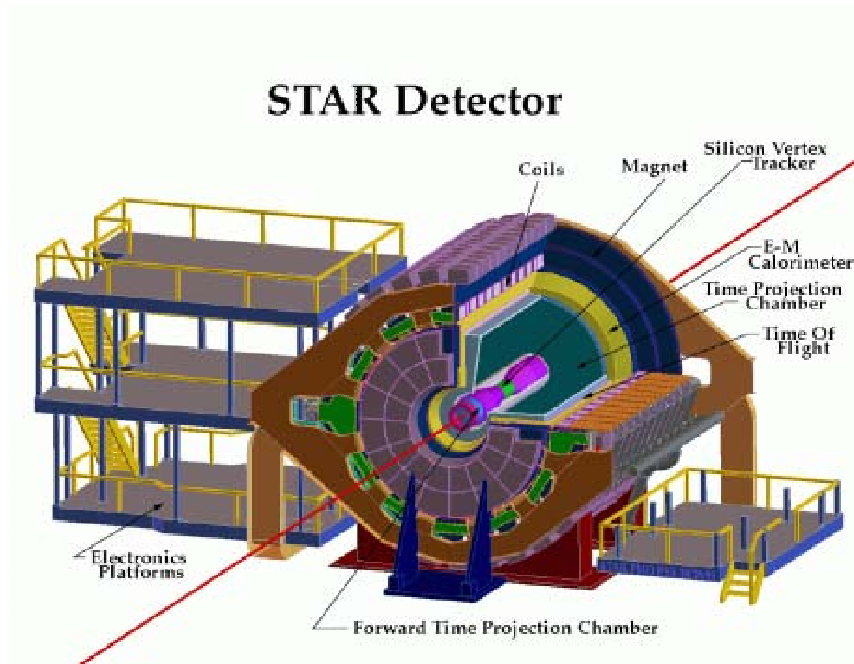
Figure 2.2: Perspective view of STAR detector, with a cutaway for viewing inner detector systems. Figure is taken from [STA03].

The layout of the STAR experiment is shown in Fig. **??**. Fig. 2.3 shows the cutaway view of the STAR detector. The STAR magnet is cylindrical in design with a length of 6.85 m and has inner and outer diameters of 5.27 m and 7.32 m, respectively. A uniform magnetic field of 0.5 T (full field or reversed full field) or 0.25 T (half field) is provided for the tracking of charged particles. The main tracker - TPC for charged particle tracking and identification is 4 meters long and located at a radial distance from 50 to 200 cm from the beam axis including 45 layers. It covers a pseudo-rapidity range $|\eta| < 1.5$ and in full azimuth (2π). There are inner detectors *Silicon Vertex Tracker* (SVT) and *Silicon Strip Detector* (SSD) close to the interaction vertex, which provides additional high precision space points on track so that it improves the position resolution and allows us to reconstruct the secondary vertex of weak decay particles. Both the TPC and SVT contribute to particle identification using ionization energy loss (dE/dx), with an anticipated combined energy loss resolution of $\sigma = 7\%$. The momentum resolution

reaches a value of $\delta p/p = 0.02$ for a majority of the tracks in the TPC. The momentum resolution improves as the number of hit points (nhitpts) along the track increases and as the particle' s momentum decreases, as expected.
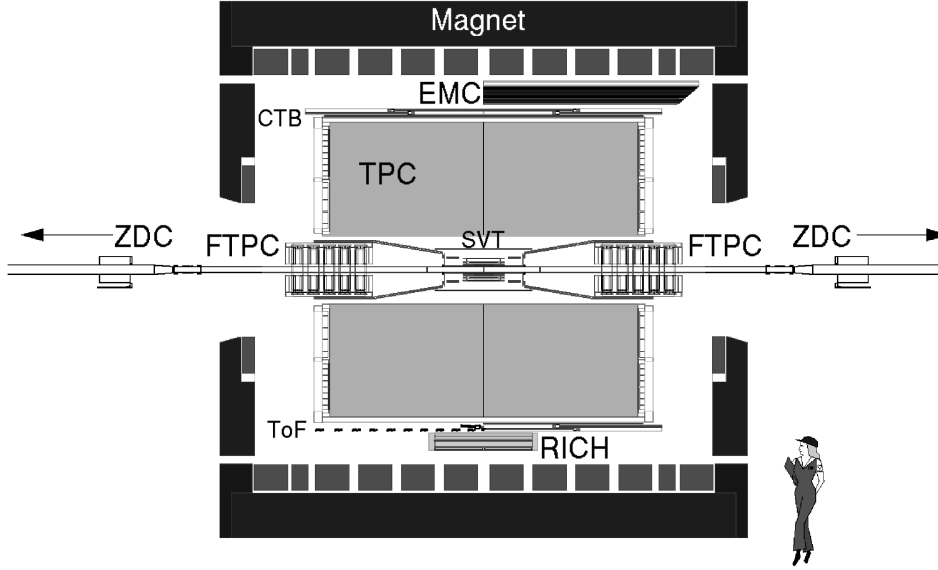
Figure 2.3: Cutaway view of the STAR detector. It includes the partial installed ElectroMagnetic Calorimeter (EMC) and two prototypes Time-of-Flight (TOF) detectors.

In the extended large rapidity region, there are two *Forward TPC* (FTPC) detectors installed covering $2.8 < |\eta| < 3.8$ with complete azimuth to track particles at forward and backward rapidity. One prototype tray of *Time-Of-Flight* (TOF) detector using scintillator materials (TOFp) was installed since Run II and another prototype tray of TOF detector using *Multigap Resistive Plate Chamber* (MRPC) technology (TOFr) was installed since Run III, covering $-1 < |\eta| < 0$ and $\frac{1}{120}$ of full azimuth. In future run, TOFp will be removed and a full barrel TOF detector based on MRPC technique will be installed, which is expected to extend the PID capability of STAR greatly. Part of barrel *ElectronMagnetic Calorimeter* (BEMC) and endcap EMC (EEMC) were also installed since Run II. They are used to measure the electromagnetic probes - electrons and photons.

The fast detectors are designed for providing inputs of the trigger system, such as *Zero-degree Calorimeter* (ZDC), *Central Trigger Barrel* (CTB) and *Beam-Beam Counters*

(BBC). Two ZDCs locates on each side ~ 18 m away from the collision points. Each is centered at 0° and covers ~ 2.5 mrad. In the collision, usually just the overlap parts of the two colliding ions interact with each other. The left fragments are continuously going forward. The charged fragments are bent by the dipole magnets and the outgoing neutrons can be detected by the ZDCs. The ZDC signals are used for monitoring the heavy ion beam luminosity and for the experiments triggers. A minimum bias trigger was obtained by selecting events with a pulse height larger than that of one neutron in each of the forward ZDCs, which corresponds to 95 percent of the geometrical cross section. The CTB is a collection of scintillating tiles surrounding the outer cylinder of the TPC. The CTB will be mostly used to select central triggered events in heavy ion collisions by measuring the occupancy of those CTB slats. The BBC subsystem covers $3.3 < |\eta| < 5.0$, measuring the "beam-jets" at high rapidity from *Non-Singly Diffractive* (NSD) inelastic $p+p$ interactions. It consists of two disk shaped scintillating detectors, with one placed at each endcap of the TPC (3.5 m from TPC center). Each BBC disk is composed of scintillating tiles that are arranged in a hexagonal closest packing. The $p+p$NSD trigger sums the output of all tiles on each BBC and requires a coincidence of both BBC's firing above noise threshold within a time window.

2.3   The Time Projection Chamber - TPC

TPC is the primary tracking device of the STAR detector [And03]. The TPC is designed to record the tracks of particles, provide the information of their momenta, and identify the particles by measuring their ionization energy loss (dE/dx). Charged particles are identified over a large momentum range from 0.15 GeV/c to ~ 30 GeV/c. For half field, the lower limit ~ 0.075 GeV/c can be achieved. The TPC consists of a 4.2 m long cylinder with 4.0 m in diameter. The cylinder is concentric with the beam pipe, and the inner and outer radii of the active volume are 0.5 m and 2.0 m, respectively. The TPC covers the full region of azimuth ($0 < \phi < 2\pi$) and covers the pseudo-rapidity range of $|\eta| < 2$ for inner radius and $|\eta| < 1$ for outer radius. Fig. 2.4 shows a cutaway view of the

TPC structure.
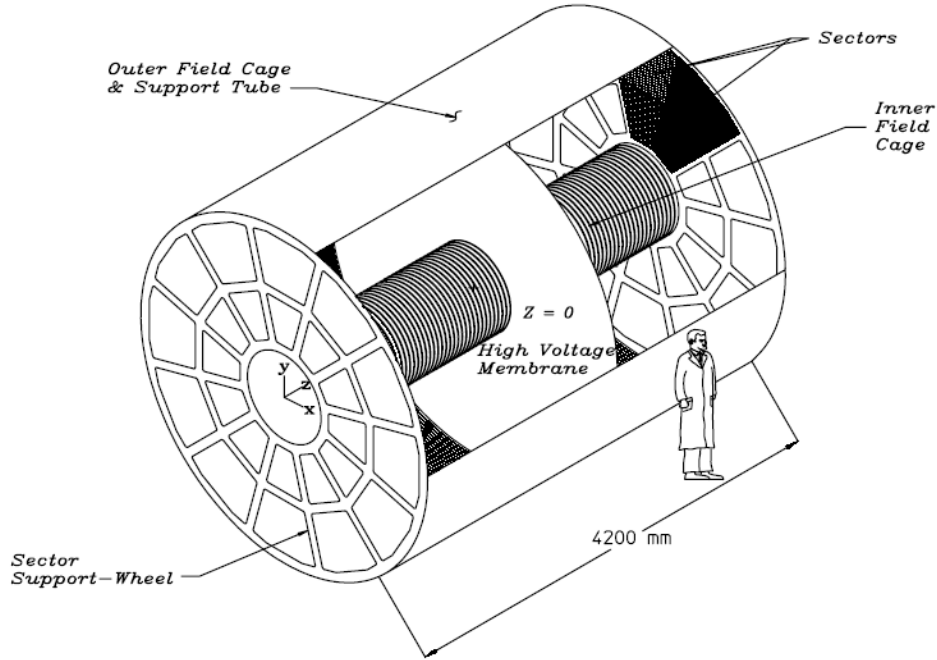
Figure 2.4: Cutaway view of the TPC detector at STAR.

The TPC is divided into two parts by the central membrane. It is typically held at 28 kV high voltage. A chain of 183 resistors and equipotential rings along the inner and outer field cage create a uniform drift filed ($\sim$ 135 V/cm) from the central membrane to the ground planes where anode wires and pad planes are organized into 12 sectors for each sub-volume of the TPC. The working gas of the TPC is P10, the mixture of 90% Ar and 10% CH_4, regulated at 2 mbar above the atmospheric pressure. The electron drift velocity in P10 is relatively fast, $\sim$ 5.45 cm/μs at 130 V/cm drift field. The gas mixture must satisfy multiple requirements and the gas gains are $\sim$ 3770 and $\sim$ 1230 for the inner and outer sectors working at normal anode voltages (1170 V for inner and 1390 V for outer), respectively. The readout system is based on the *Multi-Wire Proportional Chamber* (MWPC) with readout pads. Each readout pad is also divided into inner and outer sub-sectors, while the inner sub-sector is designed to handle high track density near collision vertex. 136,608 readout pads provide (x, y) coordinate information, while z coordinate is provided by 512 time buckets and the drift velocity. Typical resolution is $\sim 0.5 - 1.0$ mm.

When charged particles traverse the TPC, they liberate the electrons from the TPC gas due to the dE/dx. These electrons are drifted towards the end cap planes of the TPC and collected by a readout pad. The signal is amplified and integrated by a circuit containing a pre-amplifier and a shaper. Then it is digitalized and then transmitted over a set of optical fibers to STAR *Data AcQuisition system* (DAQ).

At the DAQ stage, raw events containing millions of ADC values and TDC values were recorded. Raw data were then reconstructed into hits, tracks, vertices, the collision position through the reconstruction chain of TPC by Kalman method. The TPC reconstruction process begins by the 3D coordinate space points finding. This step results in a collection of points reported in global Cartesian coordinates. The *Timing Projection chamber Tracker* (TPT) algorithm is then used to reconstruct tracks by helical trajectory fit. The resulted track collection from the TPC is combined with any other available tracking detector reconstruction results and then refit by application of a Kalman filter routine − a complete and robust statistical treatment. The primary collision vertex is then reconstructed from these global tracks and a refit on these tracks with the *distance of closest approach* (*dca*) less the 3 cm is preformed by a constrained Kalman fit that forces the track to originate from the primary vertex. As expected, the vertex resolution decreases as the square root of the number of tracks used in the calculation. The primary vertex resolution is $\sim$ 350 μm with a track multiplicity above 1000. The reconstruction efficiency including the detector acceptance for primary tracks depends on the particle type, track quality cuts, p_T, track multiplicity *etc*. The typical value for the primary pions with $N_{fit} \geq 25$ and $|\eta| < 0.7$, *dca* < 3.0 cm is approximate constant at $p_T > 0.4$ GeV/c: $>\sim$ 90% for Au+Au peripheral collisions and $\sim$ 80% for central collisions, respectively.

The TPC provide the track momentum and the dE/dx information for charged particles identification. For a particle with charge z (in units of e) and speed $\beta = v/c$ passing through The mean rate of dE/dx is given by the Bethe-Bloch equation 2.1 [PDG04]:

$$-\frac{dE}{dx} = Kz^2\frac{Z}{A}\frac{1}{\beta^2}\left[\frac{1}{2}\ln\frac{2m_ec^2\beta^2\gamma^2T_{max}}{I^2} - \beta^2 - \frac{\delta}{2}\right] \qquad (2.1)$$

The meaning of each symbol can be referred to [PDG04]. Different types of particles (different rest masses) with the same momentum have different kinematic variables β (γ), which may result in distinguishable dE/dx. The typical resolution of dE/dx in Au+Au collisions is $\sim 8\%$, which makes the π/K separation up to $p \sim 0.7$ GeV/c and proton/meson separation up to $p \sim 1.1$ GeV/c.

Combined the TPC with other detectors, such as the TOF detector and the BEMC, *etc.*, the capability of particle identification can be greatly improved, particle separation can be extended to higher p_T region.

2.4 The prototype TOF detector based on MRPC technology

A full barrel TOF detector, based on the MRPC technology, has been proposed in the STAR detector upgrade programs. There will be 120 trays with 60 on east side and 60 on west side. For each tray, there will be 33 MRPCs. The TOFp detector (a prototype based on scintillator technology) was installed since Run II [Llo04]. It replaced one of CTB trays, covering $-1 < \eta < 0$, and $\pi/60$ in azimuth. It contains 41 scintillator slats with the signal read out by *Photo Multiplier Tubes* (PMTs). The resolution of TOFp is ~ 85 ps in Au+Au collisions. However, due to the significant higher cost by the PMTs, this design will not be used in the full TOF upgrade.

On the other hand, in Run III and Run IV, new prototypes of TOF detector based on MRPC (TOFr) were installed also covering $-1 < \eta < 0$ and $\pi/60$ in azimuth. In Run III, 28 MRPC modules were installed in the tray and 12 of them were equipped with electronics, corresponding to $\sim 0.3\%$ of the TPC acceptance [Ada03c]. In Run IV, a new tray with 24 modules were installed at the same place as Run III. But only 12 modules were equipped with valid electronics, which means the acceptance in Run IV was roughly similar to that in Run III.

The trigger system of the TOF detector is the two pVPDs, each staying 5.4 m away from the TPC center along the beam line [Llo04]. They provide a starting timing information for TOF detectors. Each pVPD consists of three detecting element tubes covering

$\sim 19\%$ of the total solid angle in $4.43 < |\eta| < 4.94$. Due to different multiplicities, the effective timing resolution of total starting time is 25 ps, 85 ps and 140 ps for 200 GeV Au+Au, d+Au and p+p collisions, respectively.
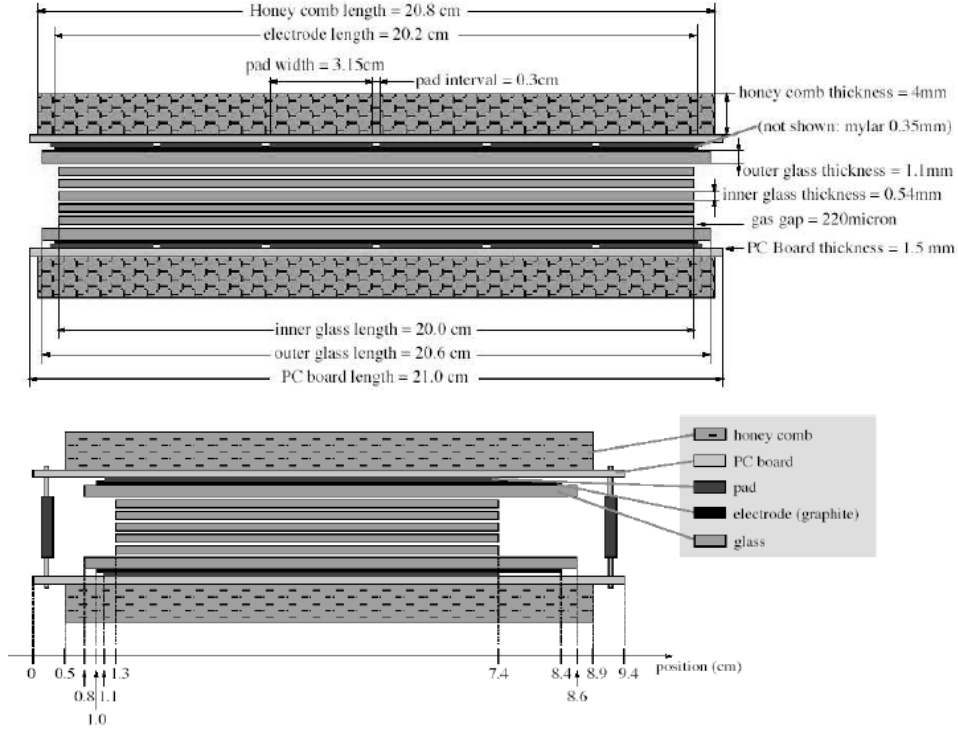
Figure 2.5: Two-side view of a MRPC module [Sha02].

Resistive Plate Chambers (RPCs) were developed in 1980s. MRPC technology was first developed by the CERN ALICE group less than 10 years ago. Fig. 2.5 shows the two side views (long edge view on top and short edge view on bottom) of an MRPC module appropriate for STAR [Sha02]. An MRPC basically consists a stack of resistive plates, spaced one from the other with equal sized spacers (such as fish line) creating a series of gas gaps. It works in avalanch mode. Electrodes are connected to the outer surfaces of the stack of resistive plates while all the internal plates are left electrically floating. Initially the voltage on these internal plates is given by electrostatics, but they are kept at the correct voltage due to the flow of electrons and ions created in the avalanches. There are six read-out strips on each module in this design. The first beam test for 6-gap MRPCs at CERN PS-T10 facility with $p_{lab} = 7$ GeV/c pions beam resulted in a ~ 65 ps timing resolution with more than 95% detecting efficiency and the module is capable of

29

working at high event rate (500 Hz/cm^2) [Sha02]. These modules were then assembled in a prototype TOF tray and tested in the AGS radiation area. Similar resolution was obtained. In RHIC Run III and Run IV, the MRPC modules in TOFr trays installed in the STAR detector were applied on the high voltage of 14 kV and with the working gas of 95% freon and 5% isobutane. The charged particle detecting efficiency is > 95% at high voltage plateau.

TOF system calibrations include the start time calibration from pVPDs and TOFr/TOFp flight time calibration. The main sources need to be considered are global time offset due to different electronics delays, the correlation between the amplitude and the timing signals, the correlation between the hit position and the timing signals *etc.* Detailed calibrations on TOF systems can be found in [Rua04b, Ada03c] (TOFr) and [Llo04] (TOFp).

CHAPTER 3

Non-photonic electron measurement in 200 GeV Au+Au collisions

Due to the large combinatorial background, direct reconstruction of heavy-flavor mesons via hadronic decay channels is difficult in current high energy nuclear collisions at RHIC [STAc05]. The indirect measurement of single leptons through heavy-flavor semileptonic decays has been used as an efficient way to study heavy flavor production. The transverse momentum (p_T) distributions of single electron and the extracted total charm cross-section have been measured in 200 GeV d+Au collisions [STAc05, Xin05]. Study of the binary collisions (N_{bin}) scaling properties for the charm total cross-section among d+Au to Au+Au collisions can test if heavy-flavor quarks are produced exclusively at initial impact. Modification of the single lepton production in nuclear collisions can reveal the heavy-flavor energy-loss. Thermal parameters extracted from the p_T distributions of single electron are useful for us to understand the heavy-flavor hadrons freeze-out and flow properties in medium in nuclear-nuclear collisions. Therefore, it is very important to measure single electron p_T distributions in Au+Au collisions.

In this chapter, analysis details of single electron p_T distributions in 200 GeV Au+Au collisions will be presented. In addition, due to large photonic background, it is difficult to measure single electron v_2 in current experimental environment, but a method to extract single electron v_2 will be proposed.

31

3.1 Non-photonic electron transverse momentum distributions

3.1.1 Data sets and cuts

In RHIC Run IV (year 2004), STAR experiment collected abundant triggered minimum bias (minbias) events and central events from $\sqrt{s_{NN}}$=200 GeV Au+Au collisions. A 0-80% minbias Au+Au collision centrality is defined by the charged particle reference multiplicity (refmult) measured at mid-rapidity ($|\eta| < 0.5$) requiring number of TPC fit points (nFitPts) > 9 and the distance-of-closest-approach (dca) < 3 cm. The sub-centralities for the data analysis are selected by applying the refmult cuts from the calculation of Glauber model [Glau01], which gives the average percentage of the number of events in each centrality bin, see Fig. 3.1. For the centrality dependence study of the non-photonic electrons, the minbias event sample was subdivided into three centrality bins: 0-20%, 20-40% and 40-80%. Table 3.1 lists the data sets under the trigger selections used in this analysis from Run IV 200 GeV Au+Au collisions. The right column lists two numbers for the size of event samples after the location of collision vertex along beam axis (V_z) cuts, one is the number of TPC triggered events used for the photonic background electron analysis, the other is the number of TOF triggered events used for inclusive electron identification.

Table 3.1: Data sets from Run IV used in this analysis

Trigger	Centrality(refmult cut)	Vertex Z cut (cm)	Events Size (TPC, TOF)
minbias	0-20% [319,1000)	$\|V_Z\| < 30$	3.28M, 1.93M
	20-40% [150,319)	$\|V_Z\| < 30$	3.36M, 1.97M
	40-80% [14,150)	$\|V_Z\| < 30$	6.55M, 3.85M
	0-80% [14,1000)	$\|V_Z\| < 30$	13.2M, 7.8M
central	0-12%	$\|V_Z\| < 50$	21.7M, 15.5M

The online centrality selection in Au+Au minbias collisions was based on the energy deposited in the two Zero-Degree Calorimeters (ZDC) [STA03, Ada05]. Since the 5-10% refmult cuts in central triggers will give some combination of ZDC- and TPC-based centrality, which is not 5-10% actually. But in the analysis, due to the limited statistics, all the central triggers are accepted, the centrality is 0-12%, the bias from realistic 0-10%

is about 5%. The TOF trigger set up in Run IV was to select events with a valid pVPD coincidence. The trigger efficiency for the TOF events is ∼60%. The tracks matched to the TOF should have good ADC signal (> 30) and at least one TOF hit. In Run IV, one TOFr tray, which is based on MRPC technology, and one TOFp tray, which uses RPC modules, were installed outside the TPC and calorimeters. The TOF detector covers 1/120 full barrel and negative pseudorapidity ($-1 < \eta < 0$).
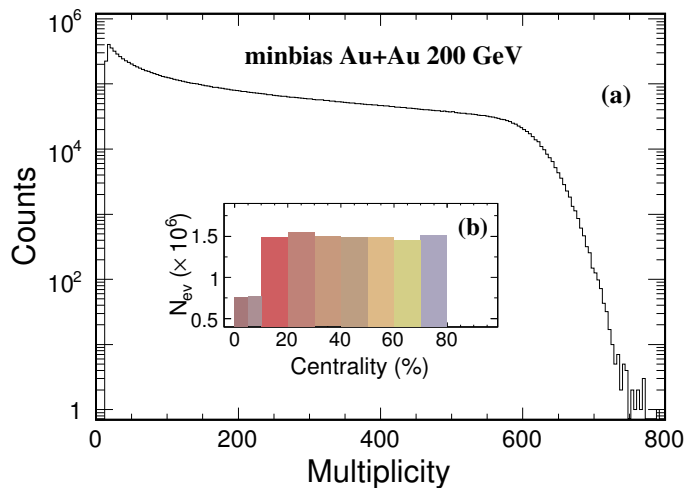
Figure 3.1: Panel (a) shows the multiplicity for minbias triggered events, which follows Glauber distribution. Panel (b) shows the centralities by cutting the multiplicity calculated from Glauber model.

3.1.2 Electron identification

The charged particle is usually identified by the ionization energy loss (dE/dx) measured in the STAR main detector TPC [And03]. With TPC dE/dx only, electron can be identified only up to $p_T \sim 0.8$ GeV/c [Ada04d, Joh02] due to large hadron contaminations. But the very small electron mass gives it the ability to be separated from other hadrons by measuring the flight timing information. The TOF detector was designed to measure the velocity (β) of electrons and hadrons [Tof05, STAc05, Sha06, Xin05].

By using a combination of velocity measured from the TOF and dE/dx measured in the TPC, inclusive electrons are identified up to $p_T \sim 4$ GeV/c in minbias Au+Au collisions and up to $p_T \sim 5$ GeV/c in central Au+Au collisions. Panel (a) of Fig. 3.2

33

shows the 2-D scattering plot of dE/dx measured from TPC vs. momentum (p) for the charged particles with good TOF hits matched in Au+Au collisions. Panel (c) shows the $1/\beta$ vs. p. Due to the different mass, charged particles can be separated by measuring their velocity. Electron band is around unity and merged with pion band. Panel (b) shows the dE/dx vs. p after the particle velocity cut ($|1/\beta - 1| < 0.03$), after most of the charged hadrons rejected, the pure dE/dx bands for electron and pion are left. And they are separated well.
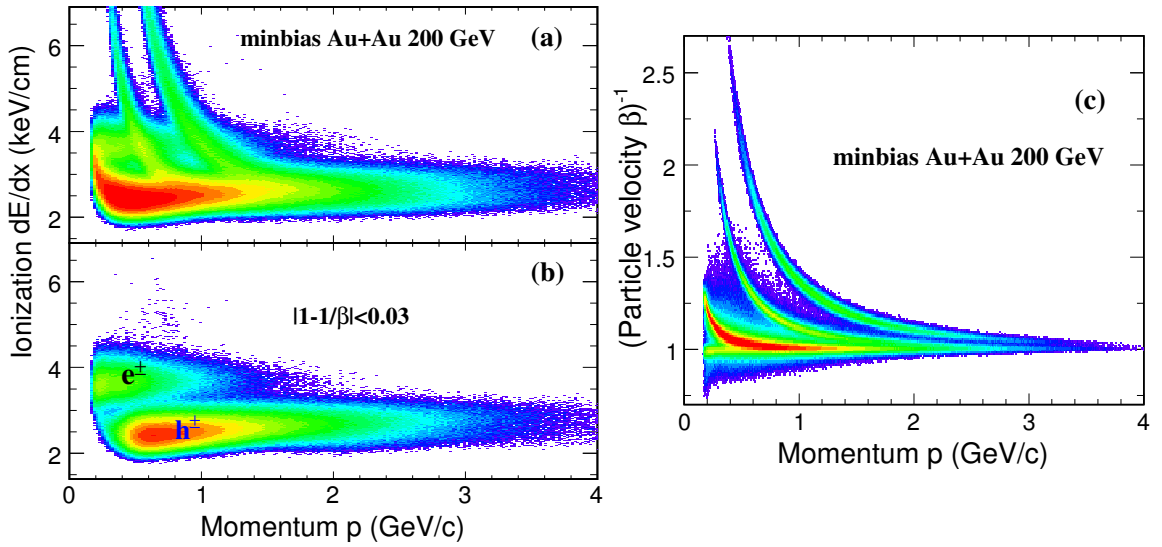
Figure 3.2: Panel (a): Ionization energy loss measured by TPC vs. momentum. Panel (b): Ionization energy loss measured vs. momentum after TOF velocity cut. Panel (c): Particle velocity measured by TOF vs. momentum.

Table 3.2 lists the cuts for inclusive electron selection.

The dE/dx distributions are not exactly gaussian. The $log_{10}((dE/dx)/(dE/dx_{Bichsel}))$ (abbreviated as dE/dx), which follows gaussian distribution, was defined as the logarithmic ratio of measured dE/dx and predicted dE/dx from Bichsel model [Bic06]. After the velocity cut, the 2-dimension histogram of dE/dx as a function of p_T was projected into several p_T bins. The 2-Gaussian function cannot describe the shoulder region between hadron peak and electron peak well at lower p_T, a function of exponential+gaussian was performed instead. At $p_T \gtrsim 1.5$ GeV/c, the other hadrons, such as protons, contaminate

Table 3.2: Cuts for inclusive electron selection

Primary track?	yes
TOF hits matched?	yes
Global dca	< 3.0 cm
nFitPts	≥ 25
nFitdedxPts	≥ 15
nFitPts/nMax	> 0.52
$1/\beta - 1$	(-0.03, 0.03)
pseudorapidity	(-1.0, 0)
TOFr ADC	> 30

the low dE/dx window and statistics cannot enable us to distinguish the difference of these two fits, so 3-Gaussian fit was used in this p_T region. Then the inclusive electron raw yields were obtained from these fits in each p_T bin. Fig. 3.3 shows the dE/dx distributions and fitting results in several typical p_T bins after TOF velocity cut. The integral yields by applying a cut on $3\sigma > dE/dx > dE/dx_{mean}$ are used to estimate the hadron contamination compared to the fits, dE/dx_{mean} is the central value of the dE/dx distribution. During the energy deposition in the TPC, the merged tracks are measured as larger energy loss, which dominate the tails shown on the right of electron gaussian peak, see Fig. 3.3. It is more obvious in central collisions than peripheral. The higher the multiplicity is, the larger the possibility of the track mergence. There are two small gaussian contributions to the tail: one is due to two merged pions, the other is considered as a mergence of one electron and one pion. The contamination of the tail to the electron is quite small, less than percent, even it looks obvious in the log scale. The tails fade at higher p_T.

Fig. 3.4 show the difference of the fit to the tails by fixing width and opening width. The yields of the inclusive electron change less than 1%.

Since dE/dx projected in a momentum bin is more like gaussian distribution than that projected in a p_T bin. The $n\sigma(p_T)$ is defined as

$$n\sigma(p_T) \sim A \times (dE/dx - dE/dx_{Bichsel})/(dE/dx_{Bichsel} \times \sqrt{ndEdxFitPts}) \qquad (3.1)$$
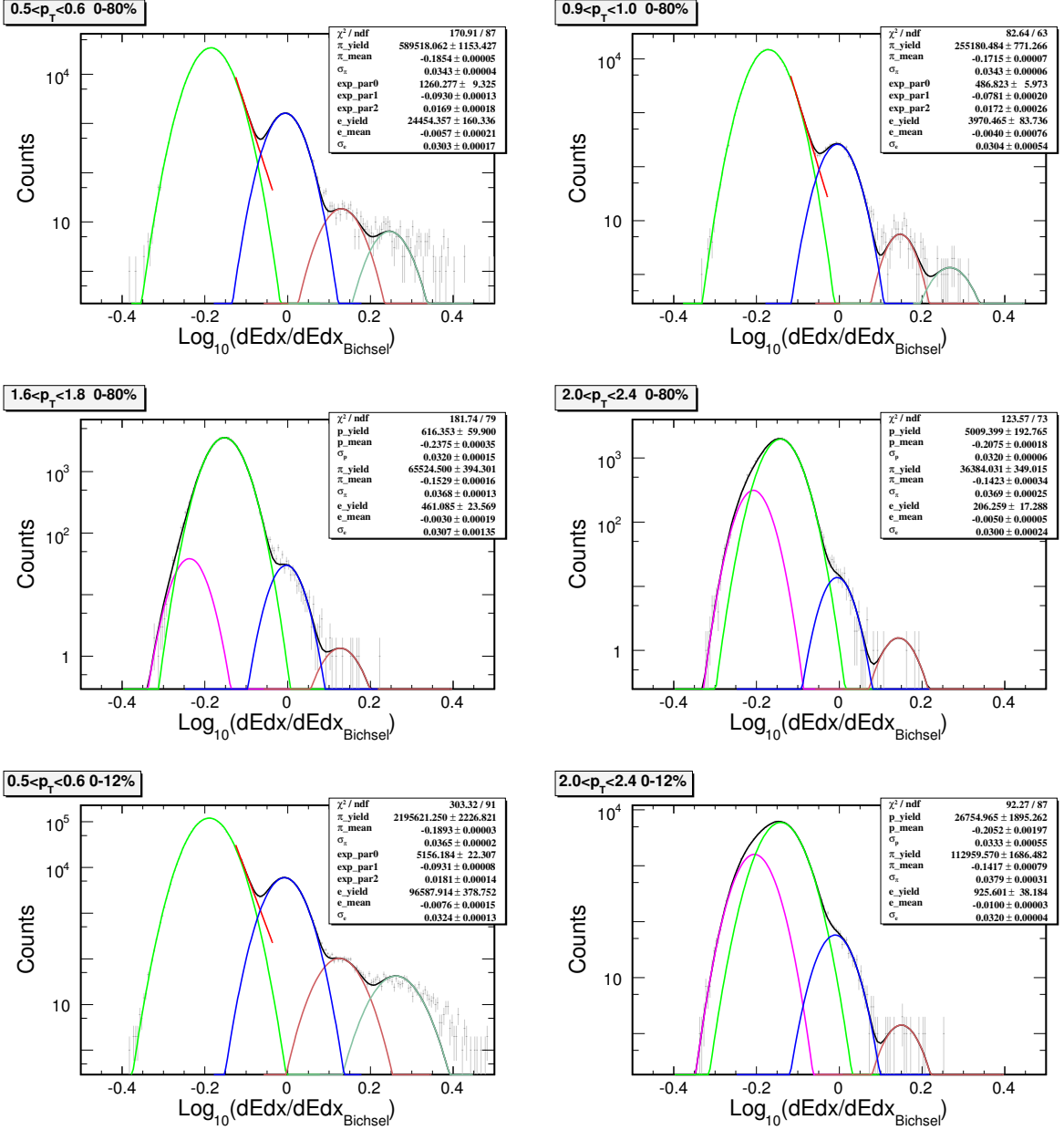
Figure 3.3: dE/dx projections in several p_T bins after the TOF velocity cut. The electron raw yields were extracted from the fit. Exponential (red curve) + gaussian (blue curve) function is used at low p_T. Multi-gaussian function is performed at higher p_T. The tails due to merged tracks are described by gaussian functions, they fade at higher p_T. The dE/dx distributions in minbias collisions (first 4 panels) and central collisions (last 2 panels) are similar.
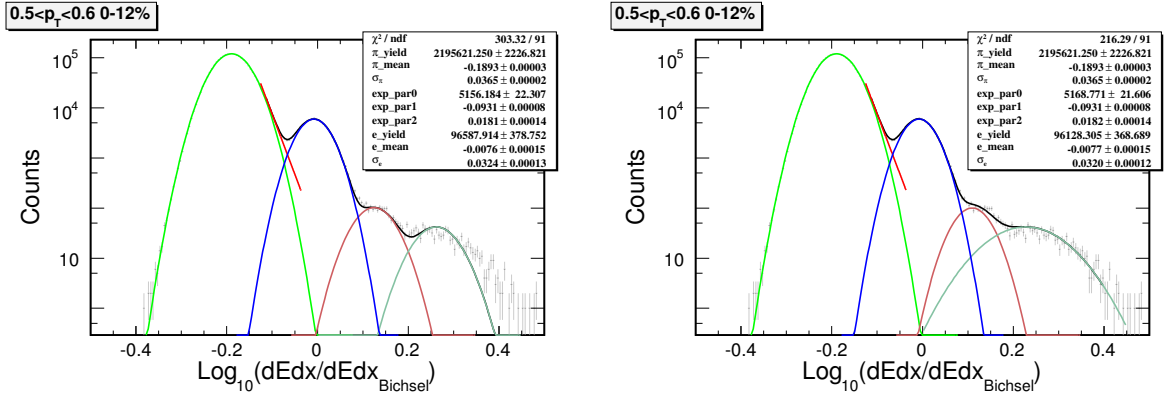
Figure 3.4: Left panel shows the gaussian fit to the tail with fixed width. Right panel shows the fit with open width. The difference of electron raw yields is $< 1\%$.

A is a constant, which only depends on the detector environment. $n\sigma$ is gaussian distribution in each p_T bin. $ndEdxFitPts$ is the number of fit points used for calculating the dE/dx of a charged particle during the tracking in the TPC. A 2-Gaussian function was used to fit the $n\sigma_e$ shown as Fig. 3.5. The difference between fit to $n\sigma_e$ and fit to $\log dE/dx$ is less than 5% point to point at lower p_T. At higher p_T the difference is even smaller, due to the smaller difference of momentum and p_T.
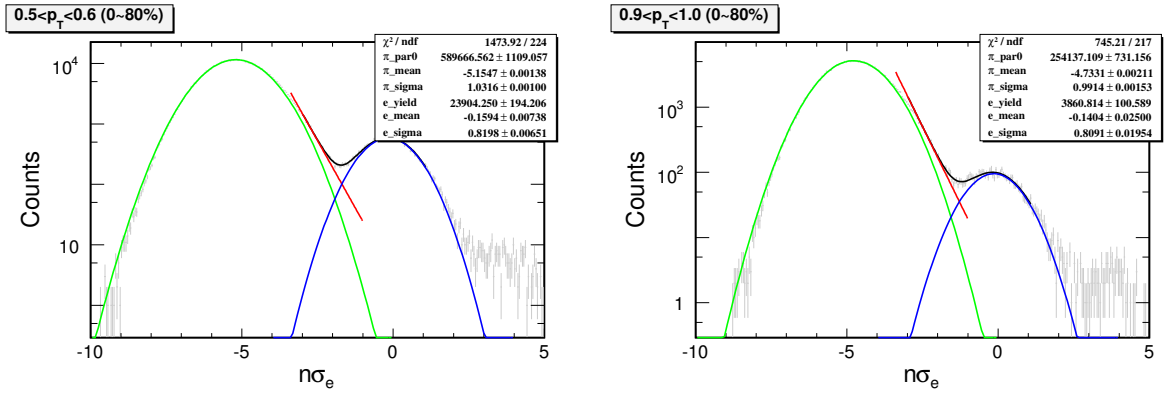
Figure 3.5: The difference between fit to $n\sigma_e$ and $\log dE/dx$ is less than 5% point to point at lower p_T. This was used to check the difference of the electron raw yields derived from dE/dx vs. p and p_T.

37

3.1.3 Acceptance and efficiencies

During the detector tracking and the extraction of the inclusive electron raw yields, a part of them were lost due to the detector acceptance, the reconstruction and cut efficiency *etc.*. The final yields of inclusive electron need to be corrected by the acceptance and efficiencies:

- TPC tracking efficiency − track reconstruction efficiency, TPC acceptance.

- TOF matching efficiency − TPC track with good TOF hits matched, TOF acceptance.

- number of dE/dx fit points cut efficiency.

Due to the lower statistics of electrons, the TPC tracking efficiency was studied from pion embedding for each centrality in Au+Au collisions, shown in left panel of Fig. 3.6. The different vertex Z cuts and eta cuts do not effect the tracking efficiency much. The TOF matching efficiencies used for electrons were determined from real data as the number of pion tracks matched to TOF divided by the number of pion tracks reconstructed from TPC. The centrality dependence of the matching efficiency is shown in right panel of Fig. 3.6. But different from electrons, $\sim 10\%$ of pions could be scattered or decay, especially at low p_T, which was corrected in the total efficiencies.

The TPC tracking efficiency does not include the ndEdxFitPts cut efficiency, since it is technically difficult to study dE/dx in embedding data. So the ndEdxFitPts cut efficiency was determined from real data as the number of tracks by cutting on ndEdxFitPtsgeq15 divided by the number of total tracks, shown in Fig. 3.7.

3.1.4 Photonic background

In this analysis, the dominant sources of photonic electron background are considered as gamma conversions and scalar meson Dalitz decay:

- $\gamma \rightarrow e^+ e^-$ photon conversions in the material in STAR detector.
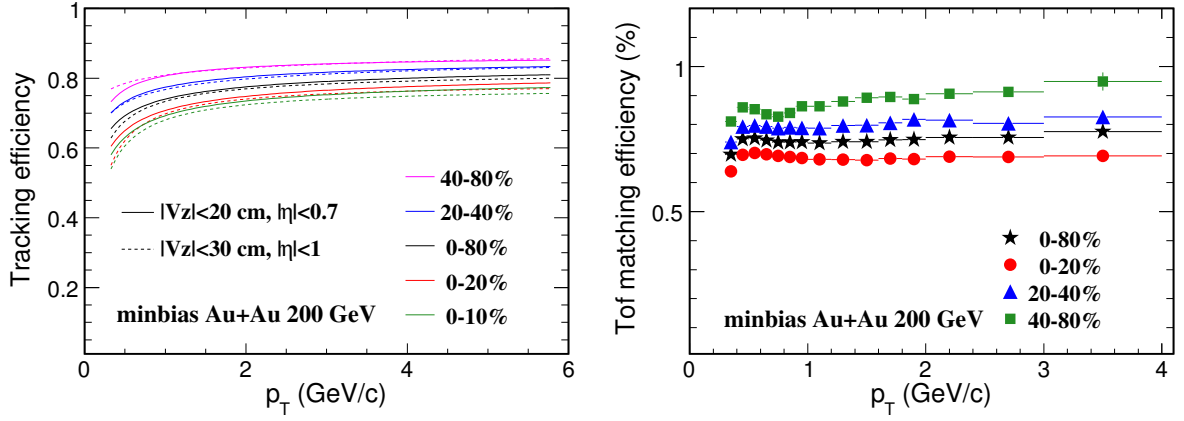
Figure 3.6: Left panel: Centrality dependence of TPC tracking efficiency from embedding data. Right panel: Centrality dependence of TOF matching efficiency from real data.
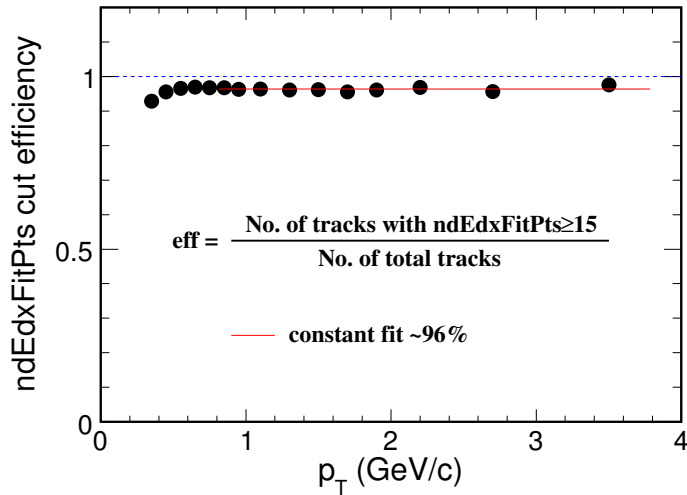
Figure 3.7: Efficiency of cutting on ndEdxFitPts $\geq$ 15 as a function of p_T.

- $\pi^0 \to \gamma e^+ e^-$ $(1.198 \pm 0.032)\%$.

- $\eta \to \gamma e^+ e^-$ $(0.60 \pm 0.08)\%$.

The huge photonic background electrons come from conversions, especially at low $p_T(<$ 1 GeV/c), due to the amount of materials in STAR detector. Fig. 3.8 shows the conversion point and conversion radius distributions from the simulation data with HIJING generator + STAR GEANT detector configuration in 200 GeV Au+Au collisions. It shows most of converted electrons are from the huge material of 3-layer SVT ($R \sim 7, 11, 16cm$) and its supporting structures.
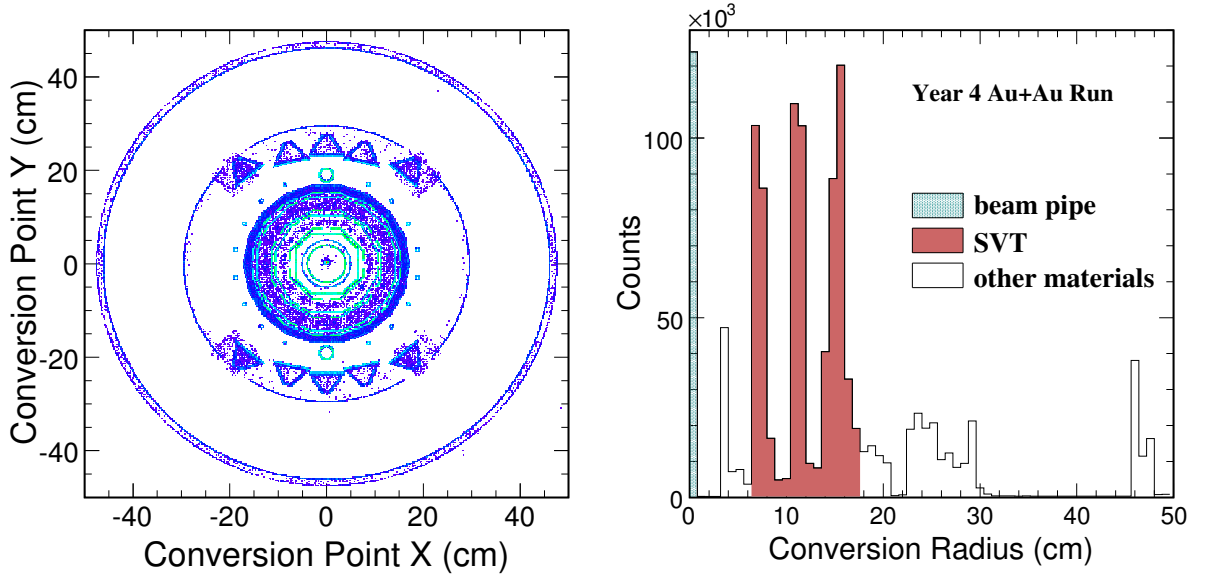
Figure 3.8: Left panel: The 2-D scattering plot for conversion point, where the photonic electron come from. It reflects the STAR material structure. Right panel: The conversion radius distributions.

Photonic electrons dominate the total yield, especially at low p_T. At $p_T > 1$ GeV/c, The electrons from heavy flavor hadron decays, which is considered as the signal, may become visible due to the enhancement of the total spectrum w.r.t background spectrum. From the previous measurements, background from photon conversion *etc.* was reconstructed experimentally using topological method [Ada04d, Joh02]. The e^+e^- from photonic background have the characteristic feature of low invariant mass. The e^+e^-

invariant mass were reconstructed from a tagged electron (positron) from TOF at low p_T (we use TPC dE/dx to identify electron at high p_T, due to the poor statistics from TOF events at high p_T) combined with every other global positron (electron) candidate, whose helixes have a dca ($dca_{e^+e^-}$) to the tagged tracks' less than 1 cm, to find the other partner track reconstructed in the TPC. Because the TPC acceptance is large enough, the pair reconstruction efficiency is reasonable. Two methods to reconstruct the invariant mass for e^+e^- pairs were used in this analysis: One is to reconstruct the invariant mass in the Cartesian coordinate. In the other method, the invariant mass of the pair is constructed in the r-z plane with an opening angle cut of ($\phi_{e^+e^-} < \pi/10$) in the azimuthal plane, here the z-axis is the beam direction. The random combinatorial background is constructed by rotating the partner candidate lepton by 180°. Raw yields of the photonic electrons are the excess over the combinatorial background in the low mass region ($M_{e^+e^-} < 150$ MeV). Comparing these two methods, the second one with an opening angle cut has the ability to reduce the combinatorial background and the effect of the secondary vertex resolution, which shift the mass to higher region (the second bump observed in the first method), see Fig. 3.9.

From the measurement of the photonic invariant mass with the combinatorial background subtracted in each p_T bin, the photonic electron raw yield is obtained. Electrons could be randomly combined with hadrons due to hadron contamination from the dE/dx selections. The different dE/dx cuts were tried to estimate the systematic uncertainties. The uncertainties of the combinatorial background ($5 - 15\%$) dominate the systematic error for photonic electron spectra. The photonic background raw yields need correction by the efficiencies and detector acceptance as what we did for inclusive electron analysis. In addition, the partner finding efficiency, which was calculated by taking the ratio of $e^+(e^-)$ with partner $e^-(e^+)$ found to total converted electrons, was done from the same reconstruction process in embedding. Since the embedded π^0 was flat in p_T, the charged π p_T distribution measured by STAR [Lqe06] was used to weight the efficiency, shown in Fig. 3.10.
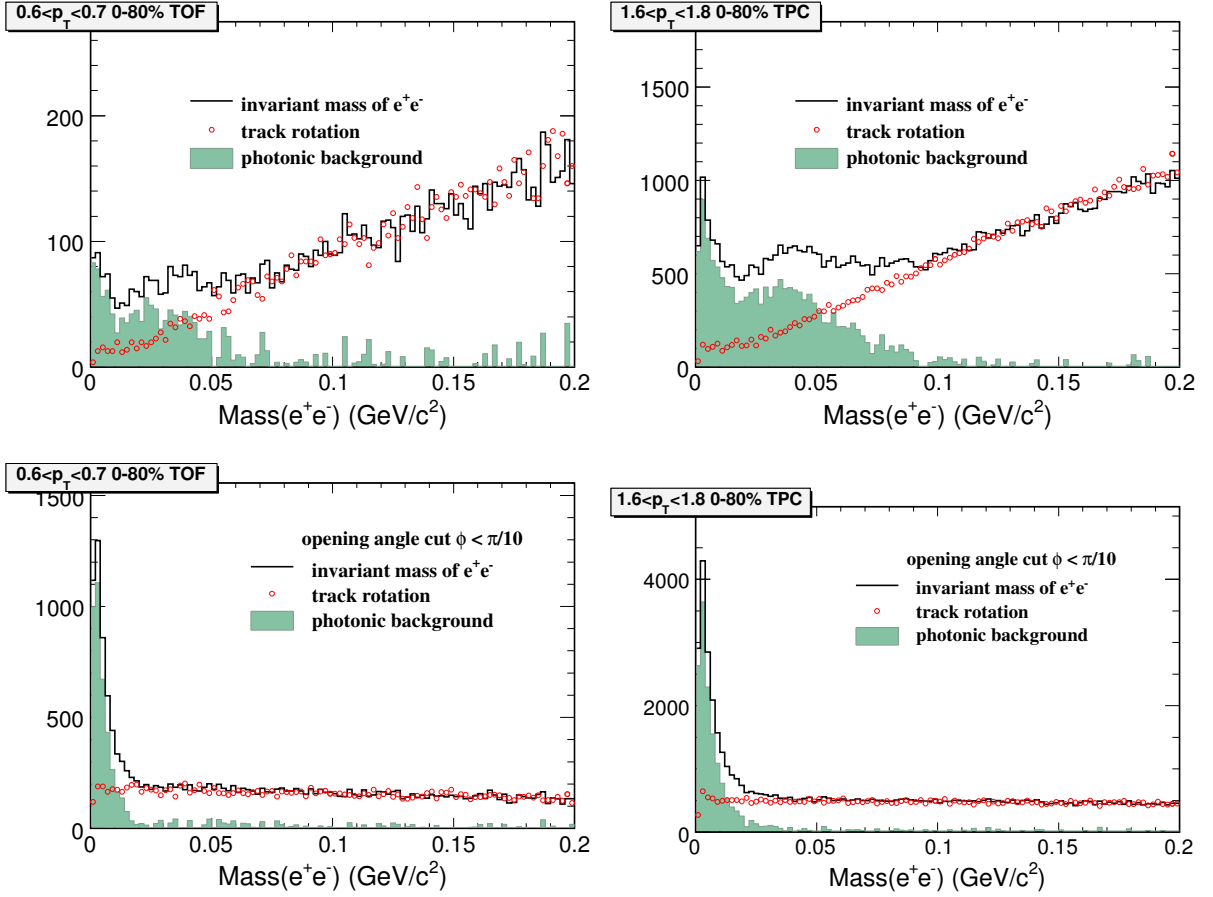
Figure 3.9: Left Column: Photonic invariant mass from TOF at low p_T. Right Column: Photonic invariant mass from TPC at high p_T. Upper Raw: Photonic invariant mass reconstructed in the Cartesian coordinate. Bottom Raw: Photonic invariant mass reconstructed in the r-z plane with an opening angle cut of ($\phi < \pi/10$) in the azimuthal plane.
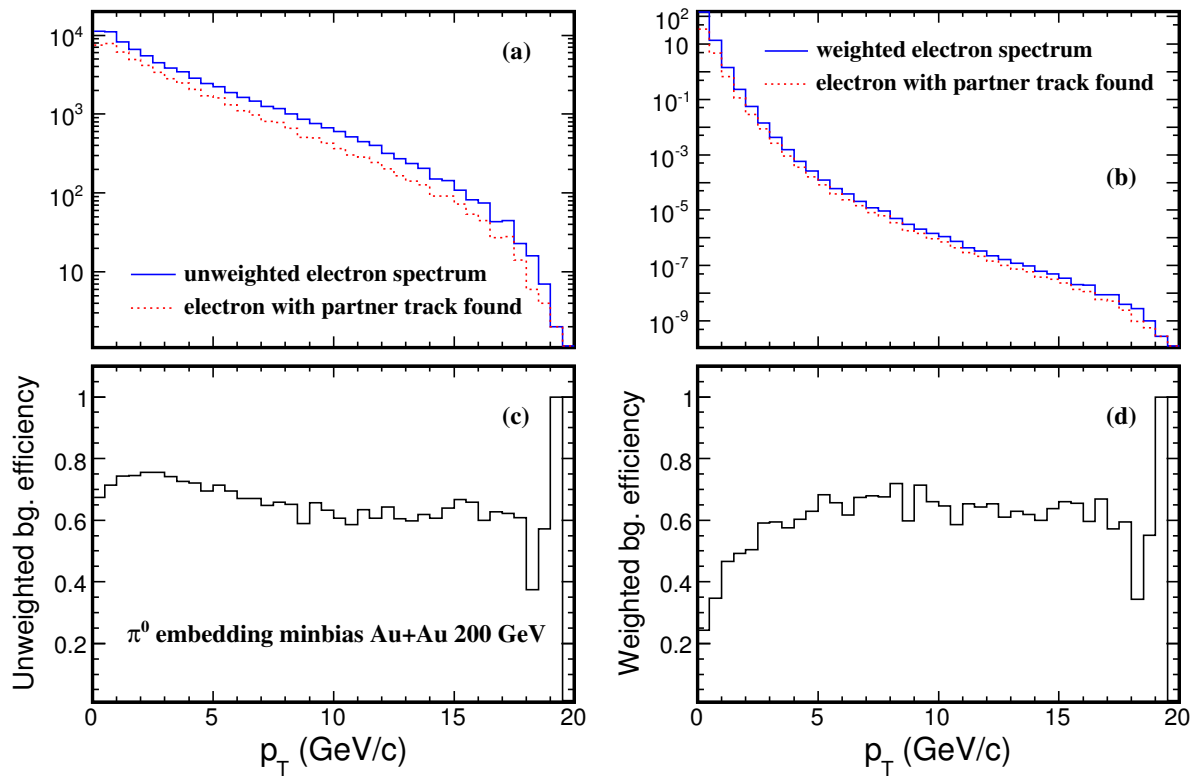
Figure 3.10: Panel (a): Converted electron p_T distribution (blue solid line) and electron p_T distributions with partner track found (red dashed line). Panel (b): Weighted electron p_T distributions. Panel (c): Background reconstruction efficiency. Panel (d): Weighted background reconstruction efficiency.

From the same embedding data, EMC electron analysis gives the consistent background efficiency, shown in the right panel of Fig. 3.11. At TOF electron p_T region, the effect of the momentum resolution to the background efficiency is small. A random sampling method was also used to cross check the normal weighted method. The normalized p_T spectra shape of π^+ was used to sample the electron candidates randomly in each p_T bin. Both the two methods give consistent efficiencies, shown in the left panel of Fig. 3.11.
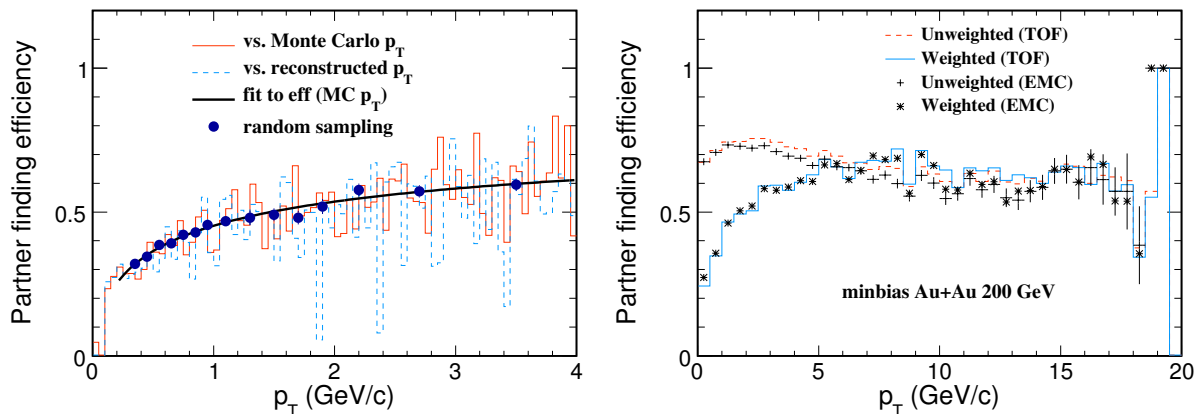
Figure 3.11: Left panel: Comparison of different ways to derive background efficiency at TOF electron p_T region from embedding. Right panel: Comparison of the background efficiency from different electron analysis.

To systematically estimate the uncertainties of different π spectra for the background efficiency weighting, the PHENIX π^0 spectrum [Phpi0] was also used to compare with STAR π^+ spectrum, shown in the Panel (c) of Fig. 3.12. The difference of the efficiencies weighted by STAR π^+ and PHENIX π^0 p_T distributions is small. At p_T around 1-5 GeV/c, the efficiencies are nearly the same. Below 1 GeV/c, the difference is up to 20%. At high p_T (> 5 GeV/c), it is $\sim$5%, see the Panel (a),(b) of Fig. 3.12.

Simply, the techniques are just shown in detail for minbias 0-80% and central 12% collisions, since good statistics can be collected in these two data sets. The techniques for other sub-centralities from minbias events are the same.

After corrected by detector acceptance and efficiencies, the inclusive and photonic electron spectra were shown in the Panel (a) of Fig. 3.13. The ratios of the inclusive spectra and the photonic electron spectra are consistent with unit at low p_T (< 0.9 GeV/c). The
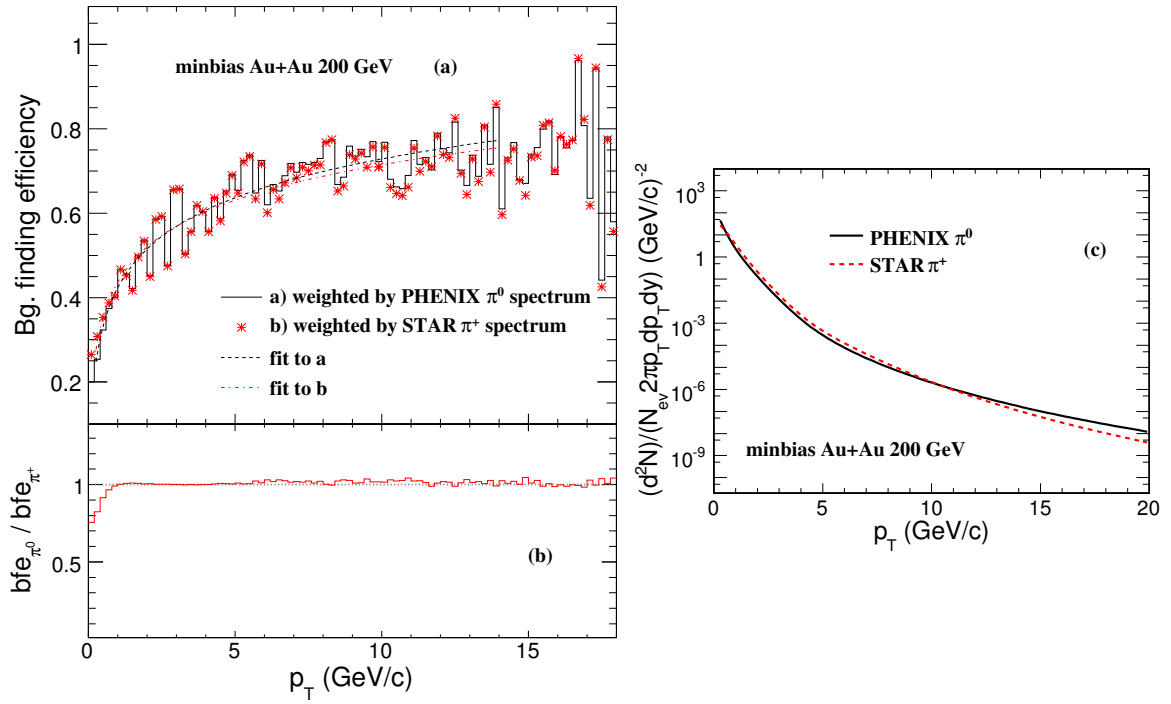
Figure 3.12: Panel (a): Comparison of the background efficiency from different weighting. Panel (b): The ratio of the efficiencies. Panel (c): Comparison of PHENIX π^0 spectrum and STAR π^+ spectrum.

increasing ratios above unit at $p_T > 0.9$ GeV/c indicate that the observable signal, shown in the Panel (b). Due to poor statistics of the invariant mass by selecting tagged electrons from TOF, we use TPC dE/dx instead. Panel (c) shows the comparison of the photonic background spectra from TOF and TPC. Within errors, they are consistent.
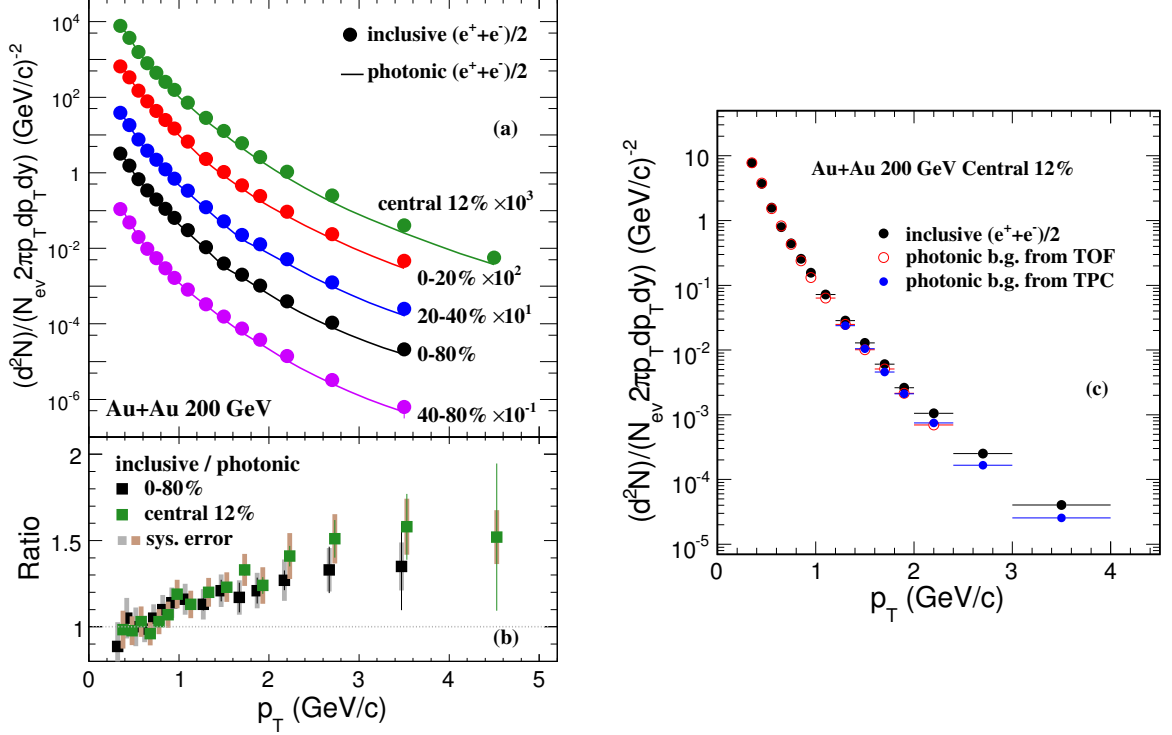
Figure 3.13: Panel (a): Centrality dependence of inclusive electron and photonic electron spectra. Panel (b): The ratio of inclusive electron over photonic electron spectra. Panel (c): Comparison of photonic spectrum from TOF and that from TPC in central 12% collisions.

Table 3.3 summarizes the cuts for tagged electron and its partner electron for the conversion pair selection.

The final spectra were also corrected by the efficiencies of the $n\sigma_e$ cuts. The efficiencies of $dca_{e^+e^-}$, $M_{e^+e^-}$ and opening angle cuts were included in the background reconstruction efficiencies from embedding. From PYTHIA study, only $\sim 2\%$ electrons from π^0 and η Dalitz decay are lost by cutting on $M_{e^+e^-} < 150$ MeV, shown in Fig. 3.14. Including vector meson decays, a 2-3% contribution from other sources to the total background was taken into account [STAc05].
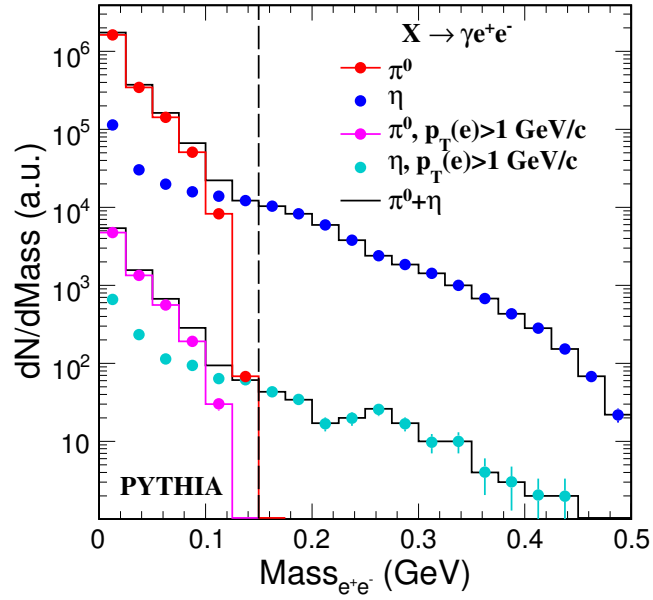
Figure 3.14: Invariant mass distributions of π^0 and η Dalitz decays from PYTHIA. The lost fraction above the mass cut is $\sim$1.4% for all electron p_T. For electron $p_T > 1$ GeV/c, the lost fraction is $\sim$2%.
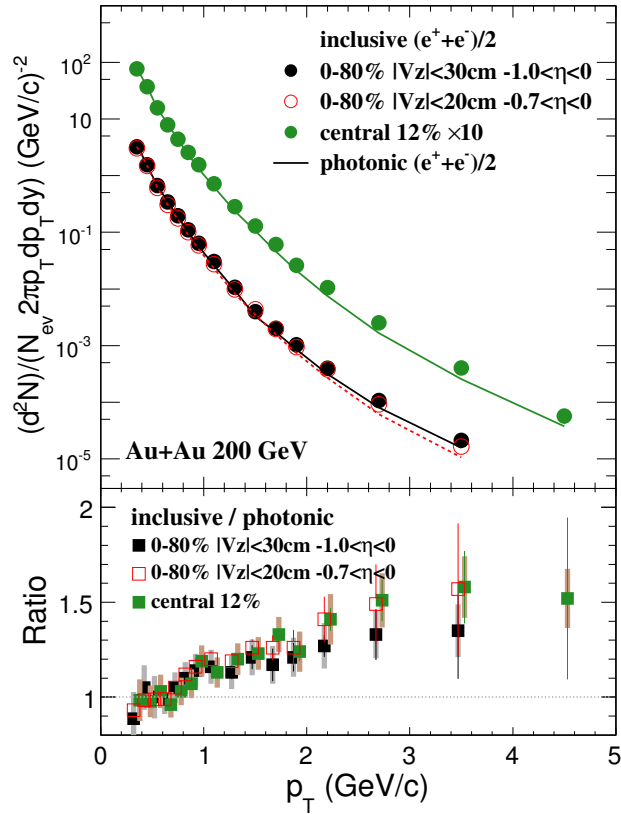
Figure 3.15: Comparison of the inclusive and photonic electron spectra and their ratios with different Vz and η cuts.

Table 3.3: Electron cuts for photonic background analysis

Tagged electron	partner electron
inclusive electron cuts required	nFitPts $\geq$ 15
	nFitPts/nMax > 0.52
$-1 < n\sigma_e < 3$ (TOF)	$-1 < n\sigma_e < 3$
$0 < n\sigma_e < 2$ (TPC)	
$dca_{e^+e^-} < 1$ cm	
$M_{e^+e^-} < 150$ MeV	
$M_{e^+e^-(\theta)} < 150$ MeV	
Opening angle $(\phi) < \pi/10$	

Since the tighter cuts for vertex-Z and eta could reduce the material influence, which is sensitive to the ratio of signal to photonic background, another cuts of $|Vz| < 20$ cm and $-0.7 < |\eta| < 0$ were applied to cross check the final inclusive and photonic electron spectra, shown in Fig. 3.15. The inclusive and photonic electron spectra are both little lower than those from former cuts, due to the reduced yields of converted electrons. The inclusive/photonic ratio is similar as central top 12%, whose Vz distributions is narrow from -20 cm to 20 cm. At higher p_T (> 2 GeV/c), the ratio from former cuts is a little lower than the central top 12% and the minbias result from new cuts, which is probably because the decrease of material by applying the new cuts.

3.1.5 Centrality dependence of non-photonic electron

After the photonic background subtraction from inclusive electrons, the non-photonic electrons, which are the signal from heavy flavor decay, are extracted. Due to low p_T huge photonic background and high p_T low statistics, the non-photonic electrons were measured covering p_T from 0.9 GeV/c to 4 GeV/c in minbias Au+Au collisions and p_T from 0.9 GeV/c to 5 GeV/c in central 12% Au+Au collisions.

Fig. 3.16 shows the centrality dependence of the non-photonic electron spectra. The bin-by-bin errors dominated by the uncertainties of inclusive electron yield extraction, photonic combinatorial background reconstruction and photonic background efficiency *etc.*, were propagated to the final non-photoinc electron spectra. The overall systematic
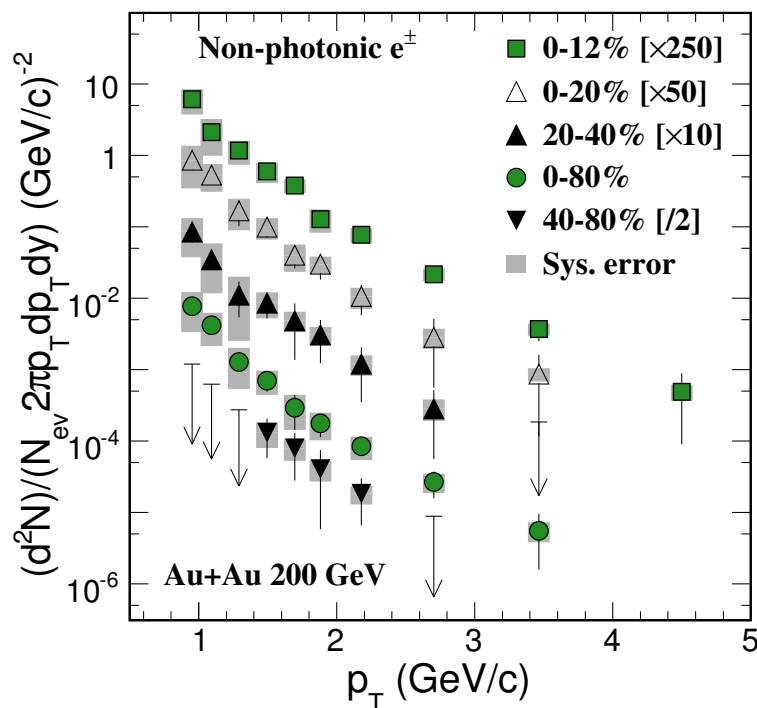
Figure 3.16: Centrality dependence of the non-photonic electron spectra.

errors, like the tracking efficiency uncertainty *etc.*, were counted in the total systematic errors, which are shown as the shaded boxes.

Table 3.4 lists the systematic error contributions.

Table 3.4: Systematic errors contributions to the electron spectra.

Inclusive electron yield extraction	$5 - 15\%$ (point-to-point)
Combinatorial background uncertainties	minbias: $6 - 15\%$ (point-to-point)
	Central $5 - 10\%$ (point-to-point)
$n\sigma_e$ cut: (0,3)(-1,3) - (-1,3)(-1,3), (0.2)(-1,3)	$3 - 5\%$
Background reconstruction efficiency	$0.3 < p_T < 0.9$ GeV/c up to 20% (weight)
	$p_T > 0.9$ GeV/c $3 - 5\%$ (weight, EMC)
η Dalitz, Kaon decay, vector meson decay	$2 - 3\%$
TPC tracking efficiency	5%
Central $10\% \rightarrow 12\%$	5%

3.2 Non-photonic electron azimuthal anisotropy distributions

3.2.1 Heavy flavor anisotropic flow

In non-central nucleus-nucleus collisions, the anisotropy in the initial coordinate space is transferred into final momentum anisotropy. The anisotropic flow is strongly sensitive to the partonic rescattering. The elliptic flow parameter v_2 from Fourier expansion of the azimuthal distributions is considered as good probe to extrapolate early pressure and density [Sor99]. The mass dependence of v_2 for identified light hadrons can be well reproduced by a hydrodynamical model in the low p_T region ($p_T < 2$ GeV/c), which indicates that the collective motion evolves in early partonic phase of the collisions [Hou01]. The p_T dependence of v_2 scaled by the number of constituent quarks is observed to be universal. The scaling behavior can be illuminated by a quark coalescence model [MV03]. But for heavy flavor quark, due to its extremely heavy mass, it can acquire flow only when light quarks punch it very frequently in a very dense medium. The thermal equilibrium is approached through sufficient interactions in the bulk matter. So the measurement of v_2 for heavy quarks is vital to test the light flavor thermalization and partonic density in the early stage of heavy ion collisions.

The single electron from heavy flavor hadrons semileptonic decay was used to infer the production of heavy quarks. The angular correlation between charmed meson and electron from its semileptonic decay is significantly strong. That indicates charmed meson v_2 can be indirectly measured through single electron v_2 [GKR04, DES04]. The non-zero single electron v_2 was observed by PHENIX detector at RHIC [SS07]. STAR detector provides a large acceptance with $|\phi| < 2\pi$, $|\eta| < 1.5$. The measurement of single electron v_2 from STAR will systematically enhance our understanding of the partonic thermalization in the high dense matter. But it is still a challenge due to the huge photon conversion from the virulent material in the STAR detector.

3.2.2 Inclusive and photonic electron elliptic flow

In this analysis, we try to develop a method to measure single electron v_2 from the data taken with the STAR experiment during the $\sqrt{s_{\text{NN}}}$=200 GeV Au+Au run in 2004. A total of 12 and 19 million 0-80% minimum bias Au+Au events were used for the inclusive electron identification from the TOF and photonic electron reconstruction from the TPC, respectively. The vertex Z is required to be less than 20 cm in order to reduce the material influence as well as the pseudorapidity $(-0.7 < \eta < 0)$.

Inclusive electrons are separated from hadrons with more than 90% purity after applying a cut of their dE/dx $(0 < n\sigma_e < 3)$ in the TPC and a cut of $|1/\beta - 1| < 0.03$ in the TOF.

As the photonic electron identification in the previous analysis for electron spectra, in the cylinder with beam axis and azimuthal plane, the invariant mass of the e^+e^- pairs is reconstructed with an opening angle cut less than $\pi/10$. The photonic electrons are identified from the previous invariant mass subtracted by the combinatorial background in a very low mass region ($M_{e^+e^-} < 15$ MeV). Other cuts such as $M_{e^+e^-} < 10$ MeV, $M_{e^+e^-} < 20$ MeV are also tried to systematically study the photonic electron v_2.

An event plane method was used for electron v_2 [PV98]. The event plane was reconstructed from the final particles' azimuths excluding electron candidates ($n\sigma_e < 0$ or $n\sigma_e > 3$) to remove the auto-correlations. The acceptance and efficiency of the detectors in azimuth was corrected by compensating the azimuth to a flat distribution with ϕ weights from day-by-day run. Additional p_T weights were also applied to improve the event plane resolution. The second order harmonic azimuth angle Ψ_2 for event plane can be calculated from the $\overrightarrow{Q}$ vector, as Eq. 3.2,3.3:

$$\Psi_2 = \left(\arctan \frac{Q_y}{Q_x} \right) /2, \qquad 0 < \Psi_2 < \pi \qquad (3.2)$$

$$\overrightarrow{Q} = (Q_x, Q_y) = \left(\sum_i w_i \cdot \cos(2\phi_i), \quad \sum_i w_i \cdot \sin(2\phi_i) \right) \qquad (3.3)$$
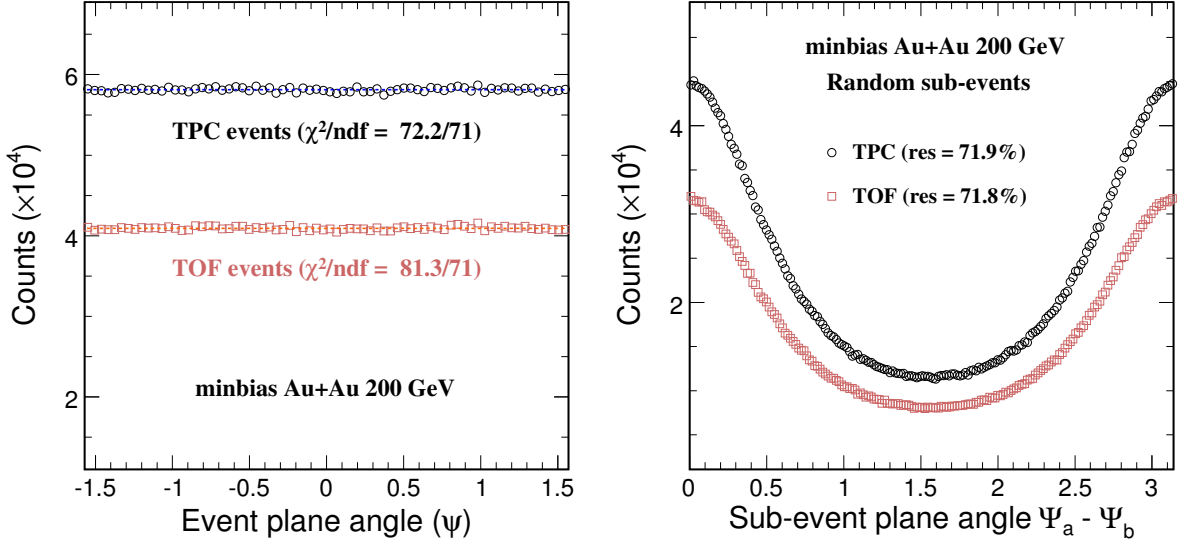
Figure 3.17: Left panel: The event plane azimuthal angle distributions from TPC and TOF events. Right panel: Event plane resolution from random sub-event method.

Here, w_i is the weight for each track with both the track azimuthal compensation and p_T weight contributions.

The left panel of Fig. 3.17 shows the event plane azimuthal angle distributions from both TPC and TOF events. A constant function fit to the distributions gives reasonable χ^2/ndf, which indicates that the event plane was reconstructed successfully.

The event plane resolution was calculated using the random sub-event method [PV98]. Each event was divided into two sub-events "a" and "b" randomly. Two event plane azimuthal angles Ψ_2^a and Ψ_2^b were reconstructed correspondingly. Then the event plane resolution $r = \langle cos[2(\Psi_2 - \Psi_{rp})]\rangle$ can be calculated from Eq.(14) and (11) of [PV98]:

$$\langle \cos[2(\Psi_2 - \Psi_{rp})]\rangle = \frac{\sqrt{\pi}}{2\sqrt{2}}\chi_2 \exp(-\chi_2^2/4) \times [I_0(\chi_2^2/4) + I_1(\chi_2^2/4)] \tag{3.4}$$

$$\langle \cos[2(\Psi_2^a - \Psi_{rp})]\rangle = \sqrt{\langle \cos[2(\Psi_2^a - \Psi_2^b)]\rangle} \tag{3.5}$$

$$\chi_2 = v_2/\sigma = v_2\sqrt{2N} \tag{3.6}$$

Ψ_{rp} is the event plane angle calculated from the event plane $\overrightarrow{Q}$ vector. I_0 and I_1
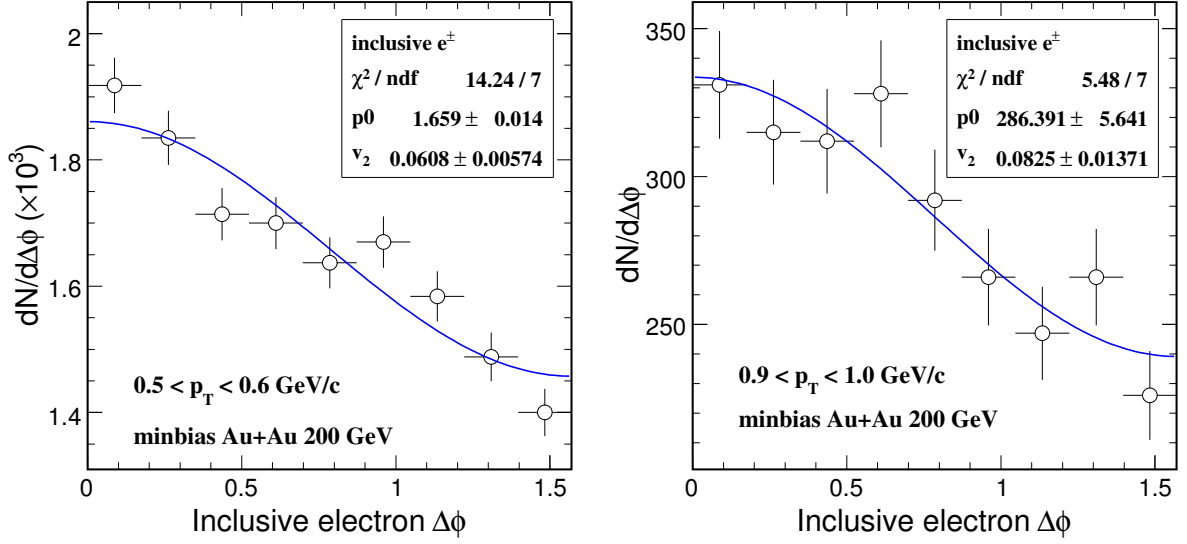
Figure 3.18: Inclusive electron $\Delta\phi$ distributions from TOF.

are the Bessel functions. The event plane resolution is around 72% from random sub-event method, shown in the right panel of Fig. 3.17. The event plane angle Ψ_{rp} is used as reference to obtain the azimuthal distributions ($dN/d\Delta\phi$) of inclusive and photonic electrons. Fig. 3.18 shows the $dN/d\Delta\phi$ distributions for inclusive electron in two typical p_T bins. The v_2 can be extracted from fitting the $dN/d\Delta\phi$ distributions in each p_T bin corrected by the event resolution.

The electron pairs in the mass window $M_{e^+e^-} < 15$ MeV are filled into $dN/d\Delta\phi_{all}$ distributions as well as the combinatorial background electrons $dN/d\Delta\phi_{com}$. Then the photonic electron $dN/d\Delta\phi_{ph}$ distributions were derived as:

$$dN/d\Delta\phi_{ph} = dN/d\Delta\phi_{all} - dN/d\Delta\phi_{com} \tag{3.7}$$

Fig. 3.19 shows the extraction of the $dN/d\Delta\phi$ distributions for photonic electrons. Photonic electron v_2 was also obtained from fitting to the $dN/d\Delta\phi$ distributions in each p_T bin corrected by the event resolution.

The inclusive and photonic electron v_2 are shown in Fig. 3.20. They are higher than the meson and baryon v_2 shown in lines [DES04] in the low p_T due to the decay kinematics.
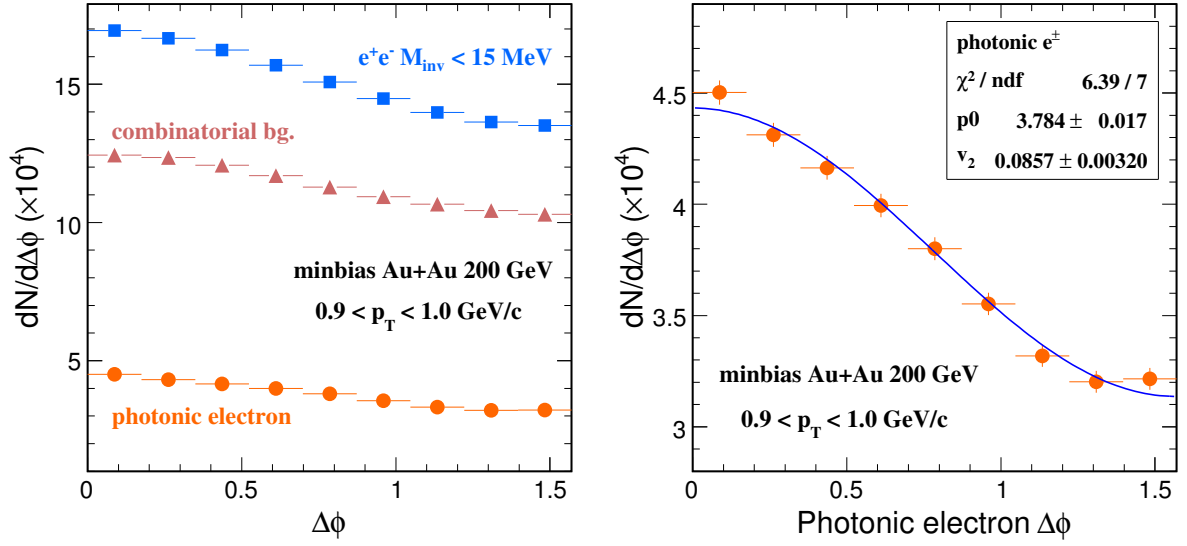
Figure 3.19: Left panel: Extraction of photonic electron $dN/d\Delta\phi$ distribution from TPC. Right panel: Photonic electron $dN/d\Delta\phi$ distribution (zoom in the photonic electron $\Delta\phi$ distribution in the left panel).
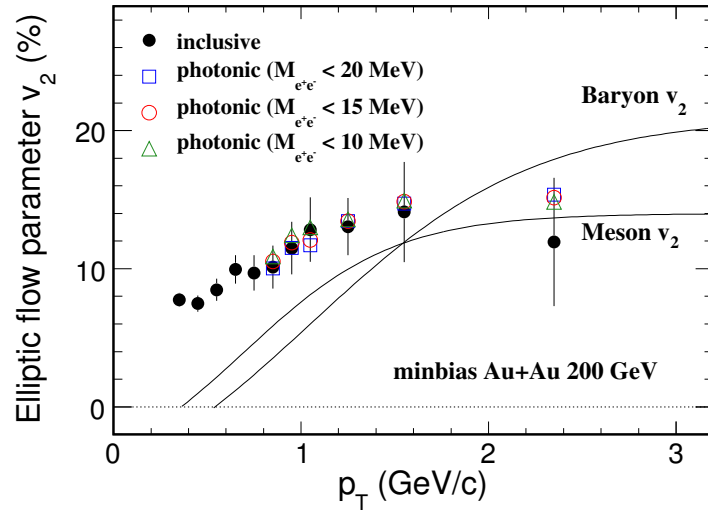
Figure 3.20: Inclusive electron v_2 from TOF and photoinic electron v_2 from TPC comparing with meson v_2 and baryon v_2. Error bars are only statistical.

The different invariant mass cuts are systematically tried for the photonic electron v_2. The statistical errors are limited by inclusive electron yield.

3.2.3 non-photonic electron elliptic flow

The non-photonic electron v_2 and its propagated error can be derived from the formulae:

$$v_2^{non} = \frac{rv_2^{inc} - v_2^{pho}}{r - 1}, \sigma_{v_2^{non}} = \frac{r\sigma_{v_2^{inc}}}{r - 1},$$

where r is the yield ratio of inclusive over photonic electrons, which is from the measurement of their spectra. The statistic error of photonic electron is extremely small to be neglected comparing to that of inclusive electron. The non-photonic electron v_2 is shown in the bottom panel of Fig. 3.21. The wild error bars are due to the very small r ($\sim 1.3 - 1.5$ at $2 - 3$ GeV/c) and large errors of inclusive electron v_2. The small r is due to the huge photon conversion from the material in the STAR detector. The poor statistics of inclusive electron is due to the small acceptance of current TOF tray.
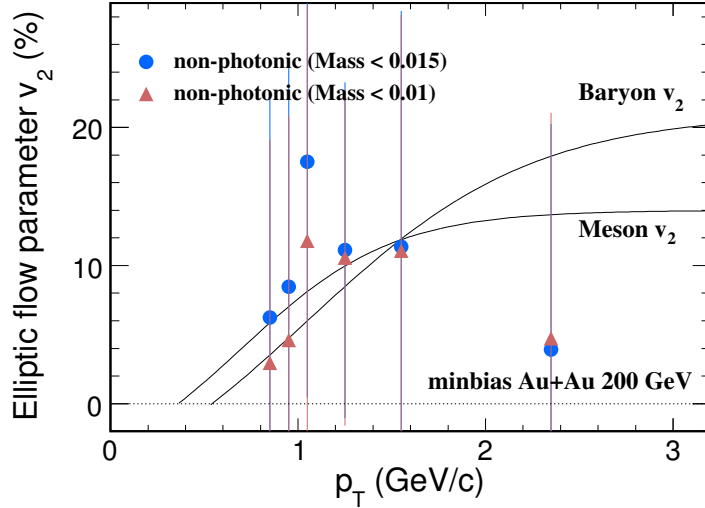
Figure 3.21: Current status of TOF non-photoinic electron v_2 from inclusive electron v_2 with the photonic background subtracted.

The coming update for STAR detector will give us a very good chance to measure non-photonic electron v_2 precisely. The hydrodynamic model and quark coalescence model for heavy flavors will be tested from this future experiment at STAR.

CHAPTER 4

Charm energy-loss, freeze-out, flow properties and cross-section

In this chapter, the measurements of $D^0 \to K\pi$ at low p_T (< 2 GeV/c) in 200 GeV Au+Au collisions will be introduced. In addition, we use a newly proposed technique to identify muons from charm decays at low p_T [LZZX06]. Combined with non-photonic electron measurement, all three measurements together stringently constrain the total charm production cross-section at mid-rapidity covering $\sim 90\%$ of the kinematics. They allow us to extract the charmed hadron spectral shape and to study the charm energy-loss and radial flow properties.

4.1 D^0 reconstruction in Au+Au collisions

A total of 13.3 million 0-80% minbias triggered Au+Au events in year 2004 Run IV were used for the D^0 ($\bar{D}^0$) direct reconstruction through hadronic channel ($D^0 \to K^-\pi^+$, $\bar{D}^0 \to K^+\pi^-$). The decay branching ratio is 3.83%. The collision vertex Z was required from -30 cm to 30 cm. In what follows, we imply $(D^0 + \bar{D}^0)/2$ when using the term D^0 unless otherwise specified.

Without the inner tracker devices, the exact D^0 decay vertex cannot be reconstructed due to insufficient track projection resolution close to the collision vertex. The invariant mass spectrum of D^0 mesons was obtained by pairing each oppositely charged kaon and pion candidate in the same event. The kaon and pion daughter tracks were identified by the dE/dx measured in the TPC. The cuts for selection of the D^0 daughter candidates are listed in Table 4.1.

Table 4.1: Cuts for D^0 daughter candidates.

momentum p	> 0.3 GeV/c
p_T	> 0.2 GeV/c
nFitPts	> 15
Global dca	< 1.5 cm
pseudorapidity η	(-1,1)
pair rapidity	(-1,1)
$n\sigma_\pi$	(-3,3)
$n\sigma_K$	$p < 0.7$ GeV/c (-2,2)
	$p > 0.7$ GeV/c (-1,1)

Table 4.1 lists the cuts for the kaon and pion candidate tracks.
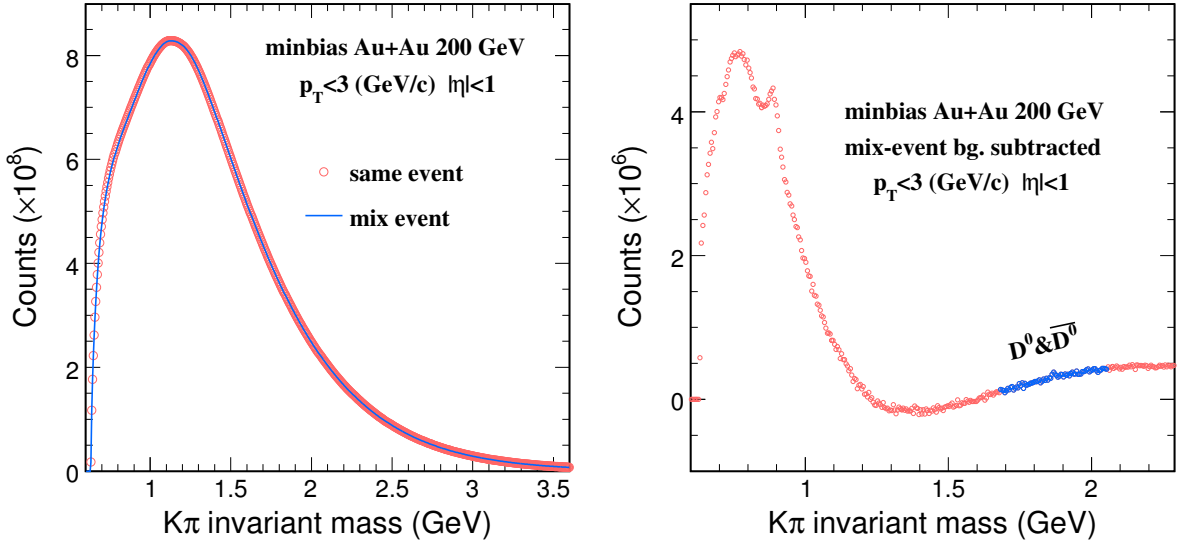
Figure 4.1: Left panel: Kaon/pion invariant mass distributions from same event (red open circle) and invariant mass distributions from mixed event (blue curve). Right panel: Kaon/pion invariant mass distributions from same event after the combinatorial background subtracted.

The random combination of kaon and pion pairs contribute to a huge combinatorial background. An event-mixing method [Hbz03, STAc05] was provided to represent the random combinatorial background. In this method, the kaon in one event and the pion in another event from the event buffer were selected to generate a reference event-mixing invariant mass distribution. The buffered event candidates were required to have similar

event environment. The mixing-buffer is divided into 10 RefMult bins and 10 Vertex Z bins. Each RefMult bin and Vertex Z bin has roughly the same number of events. Each event is mixed with two other events in the same RefMult bin and Vertex Z bin. Due to the multi-combination with different event buffers, the statistics of the combinatorial background can be increased ~ 4 times. Then the event-mixing spectrum was normalized with a factor obtained by comparing the entries in the two spectra with invariant mass > 2.5 GeV/c^2. In order to increase statistics, D^0 and $bar D^0$ signals are added together. Left panel of Fig. 4.1 shows kaon/pion invariant mass distributions from same events and mixed events after normalization. Due to the huge magnitude of the combinatorial background, the signal is invisible. But if the invariant mass distributions from same events are subtracted by the event-mixing combinatorial background, the signal can be seen within a mass region of $1.68-2.05$ GeV, shown in the right panel of Fig. 4.1. The small peak near mass ~ 0.96 GeV is known as K^*.
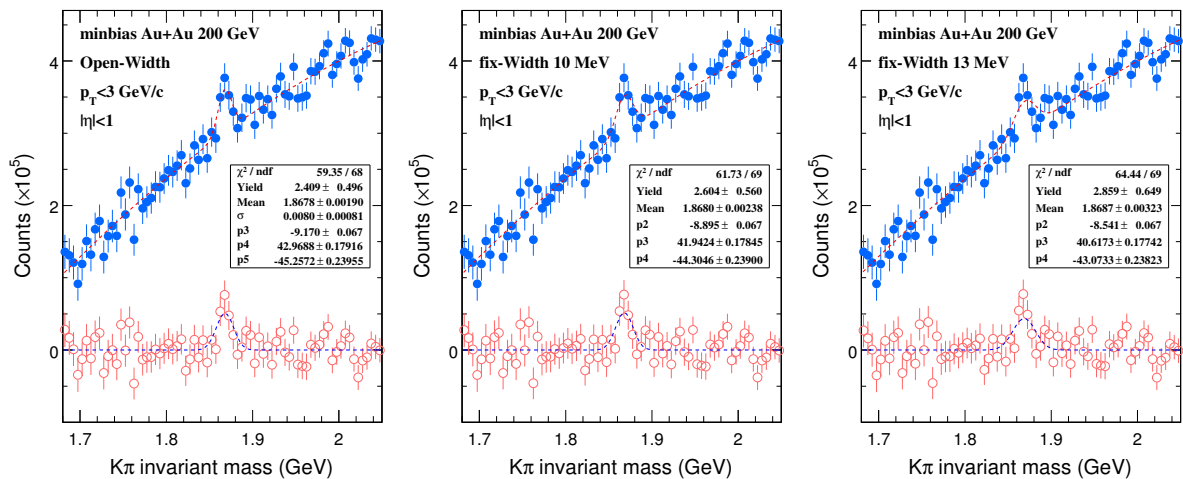
Figure 4.2: Extraction of the signal raw yields by fitting with open-width and fix-width from kaon/pion invariant mass distributions.

After the event-mixing background subtraction, the kaon/pion invariant mass distributions within the mass window ($1.68-2.05$ GeV) were shown as the blue solid circles in Fig. 4.2. The red open circle is the invariant mass subtracted by the residual background.

A gauss+linear or second order polynomial (Pol-2) function as

$$f(m) = \frac{W \times A_0}{\sqrt{2\pi} \times \sigma} \times e^{\frac{-(m-\bar{m})^2}{2\sigma^2}} + f', \qquad (4.1)$$

was used to fit the data to extract the signal, where $W = 0.005$ GeV is the bin width. A_0 is the signal raw yield. f' is the linear or the Pol-2 function. σ is the width of the gaussian mass distribution. From embedding, the width of the mass is around 13 MeV, but in real data, the width turns out to be smaller. Since in sub-p_T bins, due to statistical limit, the mass distributions can not be fitted by open width. So the width was fixed as 10 MeV, and the overall uncertainty of fix-width and open-width fits, which is around 10%, was done at $p_T < 3$ GeV/c for good statistics, shown as Fig. 4.2.

To estimate the uncertainties of the combinatorial background, we use linear and Pol-2 function to describe the background by varying several fit mass regions. The average yield from linear and Pol-2 fit with best χ^2 was extracted as the final raw yield. The dominant bin-by-bin systematic error was estimated as the largest deviation from all the fits with reasonable χ^2, since all the fit results are considered as a uniform distribution.

Fig. 4.3 gives the fits for three sub-p_T bins using linear function (the first row) and Pol-2 function (the second row) with best χ^2.

Table 4.2 lists the systematical uncertainties for D^0 spectrum in minimum bias 200 GeV Au+Au collisions.

Table 4.2: D^0 systematical uncertainties in minimum bias 200 GeV Au+Au collisions.

p_T (GeV/c)	bin-by-bin fit	open/fix-width	Full Field / Reversed FF	Tracking eff.	Track cuts (dE/dx)	Total sys.
0.2-0.7	42.9%					49.5%
0.7-1.2	26.8%	10%	9%	10%	18%	36.4%
1.2-2.0	27.0%					36.6%

The final D^0 spectrum in 0-80% minbias AuAu collisions at 200 GeV are shown in Fig. 4.8.
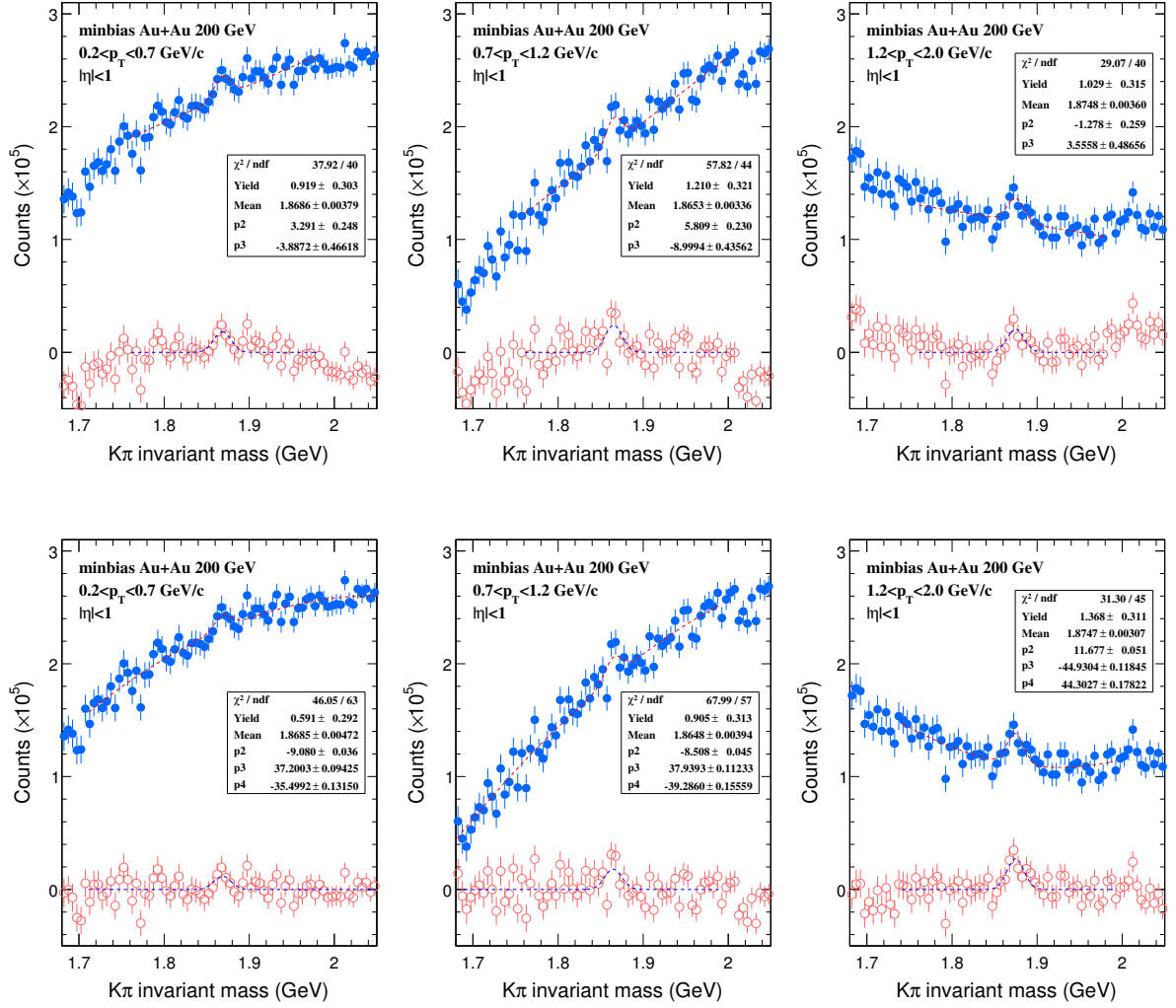
Figure 4.3: Kaon/pion invariant mass distributions by fitting with linear and Pol-2 function in each p_T bin.

4.2 Muon from charm decay at low transverse momentum

In recent experiments in STAR, due to large random combinatorial background, it is difficult to reconstruction charmed hadrons directly. And single electron measurement is impossible due to overwhelming photon conversions in the detector material and π^0 Dalitz decay at low p_T, where the yield accounts for a large fraction of the total cross-section. Nevertheless, the charm total cross-sections have been measured in d+Au collisions at RHIC by a combination of the directly reconstructed low p_T $D^0 \to K\pi$ and the non-photonic electron spectra [STAc05], and by electron spectra alone [PHECAA, PHECPP]. Although the systematic and statistical errors are large, the result indicates a much larger charm yield than predicted by pQCD calculations [STAc05, CNV05]. Since most of the measurements to date at RHIC are from indirect heavy-flavor semileptonic decays, it is therefore important to find novel approaches to improve the measurements and also study in detail how to extract the maximum information about the heavy-flavor spectrum from its lepton spectrum.

In this section, we propose a new method to extract the charm total cross-section by measuring muons from charmed hadron semileptonic decay at low p_T (e.g. $0.17 \leq p_T \leq 0.25$ GeV/c). Since muons in this p_T range are a very uniform sample of the whole charmed hadron spectrum, the inferred charm total cross-section is insensitive to the detail of the charm spectrum. Once the cross-section is determined, the electron spectrum at higher p_T can be used to sensitively infer the charmed hadron spectral shape. Left panel of Fig. 4.4 shows the charmed hadron p_T spectrum before and after requiring its decayed muons at $0.16 < p_T < 0.26$ GeV/c. The similarity of the spectral shape shows that the muon selection reasonably uniformly samples the entire charmed hadron spectrum. The muons in this p_T range sample 14% of the charmed hadron spectrum. The muon yield is about 1/70 of the charmed yield due to an additional 9.6% ($c \to l + anything$) decay branching ratio. Right panel of Fig. 4.4 shows the dependence of the muon yield on $\langle p_T \rangle$ for a fixed total charm yield. The yield is normalized to yields at $n = 10$ and $\langle p_T \rangle = 1.3$ GeV/c, see the power-law function Eq. 4.5. We also note that the muon yield has a very

weak dependence on n which demonstrates that over a wide range in $\langle p_T \rangle$, the muon yield is within $\pm 15\%$. This is in contrast to the large variation of the electron yield integrated above p_T of 1.0 GeV/c, where a factor of 8 variation is seen in Fig. 4.4.
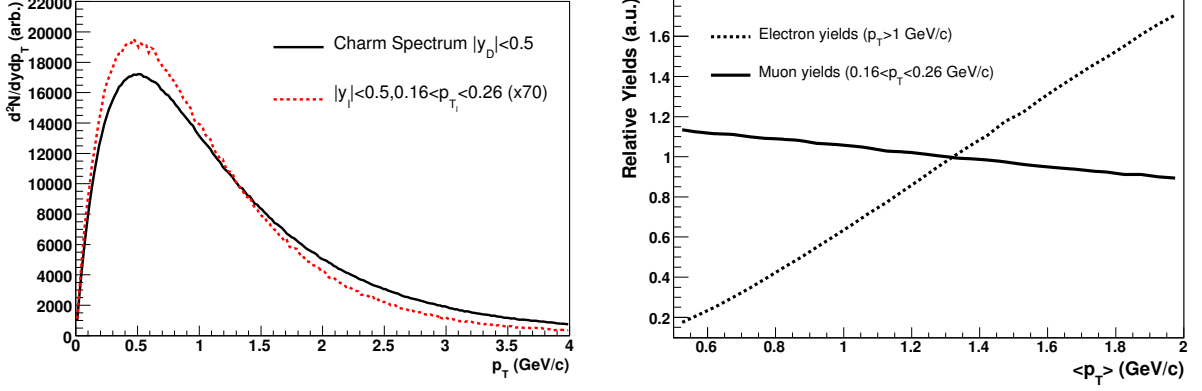
Figure 4.4: Left panel: Charmed hadron (D) spectra ($dN/dydp_T$) as a function of p_T at midrapidity before (solid line) and after (dashed line) a muon selection of $0.16 < p_T < 0.26$ GeV/c and $|y_l| < 0.5$. The later was scaled up by a factor of 70. Right panel: Lepton yields relative to the fixed total charm cross- section as a function of $\langle p_T \rangle$ for a charmed hadron transverse momentum spectrum. Solid line shows muon yields with a kinematics selection $0.16 < p_T < 0.26$ GeV/c and $|y_l| < 0.5$. Dashed line shows electron yields with $p_T > 1.0$ GeV/c.

A total of 7.8 million 0-80% minbias and 15 million 0-12% central triggered Au+Au events in year 2004 Run IV were used for the charm-decayed prompt muons analysis covering a p_T range of 0.17-0.25 GeV/c at mid-rapidity ($-1 < \eta < 0$). The collision vertex Z was required from -30 cm to 30 cm. The number of fit points was required above 24.

The low p_T single muons were analyzed by combining the dE/dx measured in the TPC and $m^2 = (p/\beta/\gamma)^2$ from the TOF at STAR [Sha06]. A variable called $n\sigma_\mu$, which is calculated as Eq. 4.4, was used for the muon dE/dx selection.

$$n\sigma_\pi = \frac{A}{\sqrt{N_{dE/dx}}} \times \ln \frac{dE/dx_{TPC}^\pi}{dE/dx_{Bichsel}^\pi}, \qquad (4.2)$$

$$n\sigma_e = \frac{A}{\sqrt{N_{dE/dx}}} \times \ln \frac{dE/dx_{TPC}^e}{dE/dx_{Bichsel}^e}, \qquad (4.3)$$

$$n\sigma_\mu = \frac{A}{\sqrt{N_{dE/dx}}} \times \ln \frac{dE/dx^\mu_{TPC}}{dE/dx^\mu_{Bichsel}}. \qquad (4.4)$$

where A is the calibration factor which only basically depends on the detector intrinsic character, $N_{dE/dx}$ is the number of dE/dx fit points for the track reconstruction, dE/dx^x_{TPC} is the energy-loss of track x measured in TPC, $dE/dx^x_{Bichsel}$ is the predicted value for track x from Bichsel calculation.

The muons were selected as $-3 < n\sigma_\mu < 0$, $-3 < n\sigma_\mu < -0.5$ for the two p_T bins: $0.17 < p_T < 0.21$ and $0.21 < p_T < 0.25$ GeV/c, respectively.
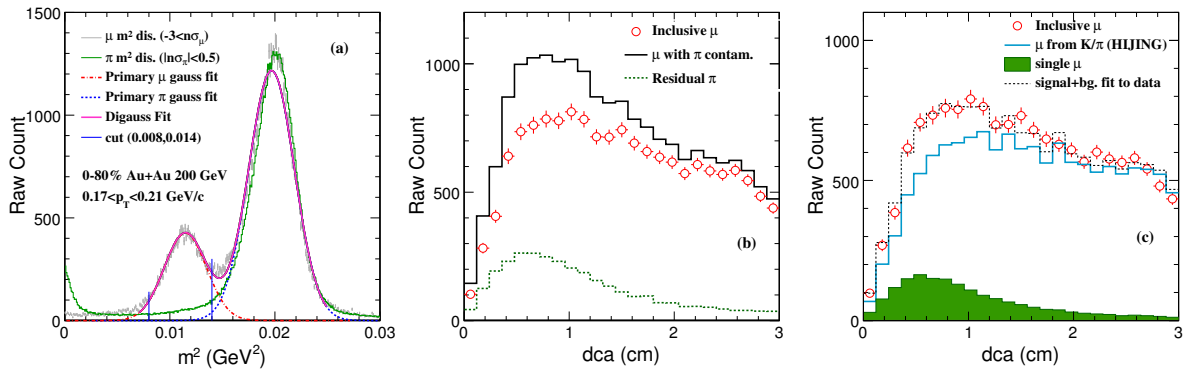
Figure 4.5: Panel (a): Particle mass squared distribution $m^2 = (p/\beta/\gamma)^2$ from the TOF measurements. A clear muon mass peak is shown on the left and the primary pion candidates are shown at the right. The pion contamination was estimated by applying pion m^2 samples using dE/dx selection. Panel (b): Inclusive muon DCA distributions were obtained by subtracting the residual pion DCA in the muon mass window. Panel (c): The single muon raw yield was obtained from a fit to muon DCA distributions with the background DCA distributions combining the primary particle DCA distributions.

After the muon dE/dx selection, a clean muon peak can be identified within a mass window of $0.008 < m^2 < 0.014$ GeV^2/c^4 measured from the TOF, see Fig. 4.5 (a). A digaussian function was used to fit the muon m^2 distributions (purple curve). The residual pions contributing to the muon mass window were estimated by a pion m^2 distributions with $|n\sigma_\pi| < 0.5$ (green histogram). After dE/dx and m^2 selections, the muon yields in the mass window were counted in each bin of the DCA distributions, see Fig. 4.5 (b). The residual pions (green dotted histogram) were subtracted statistically from the DCA distribution within the muon mass window applied to the dE/dx selected pion

sample [LZZX06]. The systematic uncertainties $(18 - 25\%)$ are dominated by the pion contaminations, which were estimated using different dE/dx cuts for the residual pions. After the residual pion contamination subtracted, the inclusive muon DCA distributions were obtained (red open circle).

The dominant background muons are from pion/kaon weak decays at low p_T. Other sources of background ($\rho \rightarrow \mu^+\mu^-$,$\eta \rightarrow \gamma\mu^+\mu^-$, etc.) are found to be negligible from simulations, due to their very low yield at low p_T. The measurement of η/π ratio shows around 0.5 at high p_T (> 3 GeV/c), but drops very fast at low p_T, its contribution to the low p_T muons is very small. The background muon from pion/kaon weak decays were subtracted using the DCA distribution from HIJING simulation. The single muon raw yield was obtained from a fit to muon DCA distributions with the background DCA distributions combining the primary particle DCA distributions [LZZX06], see Fig. 4.5 (c). The p_T distributions for muon invariant yields in 0-12% central and minbias Au+Au collisions are shown as open crosses and diamonds in Fig. 4.8, respectively.

To understand the background shape, some relevant checks were performed. The muon DCA distribution from pion decay and that from kaon decay have similar shape, shown in the left panel of Fig. 4.6, the relative yield of pion and kaon in HIJING dose not affect the background DCA shape. Embedding results give consistent shape of the background DCA, see right panel of Fig. 4.6.

4.3   Decay form factors

In this section, we discuss the charmed hadron semileptonic decay form factor and its effect on the lepton spectrum. Fig. 4.7 shows the electron momentum spectra from charmed meson decays at rest generated using the Particle Data Table [PDG02], PYTHIA [STAc05, PHECAA, PHECPP, Sj01], pQCD calculations [CNV05] and from the CLEO preliminary inclusive measurement [CLEO04]. The spectrum generated by the PDG is according to the form factor of charmed meson decays to pseudoscalar $K+l+\nu$, vector meson $K^*+l+\nu$ and non-resonance $(K\pi) + l + \nu$ where the K^* mass is used for the $(K\pi)$ system. The
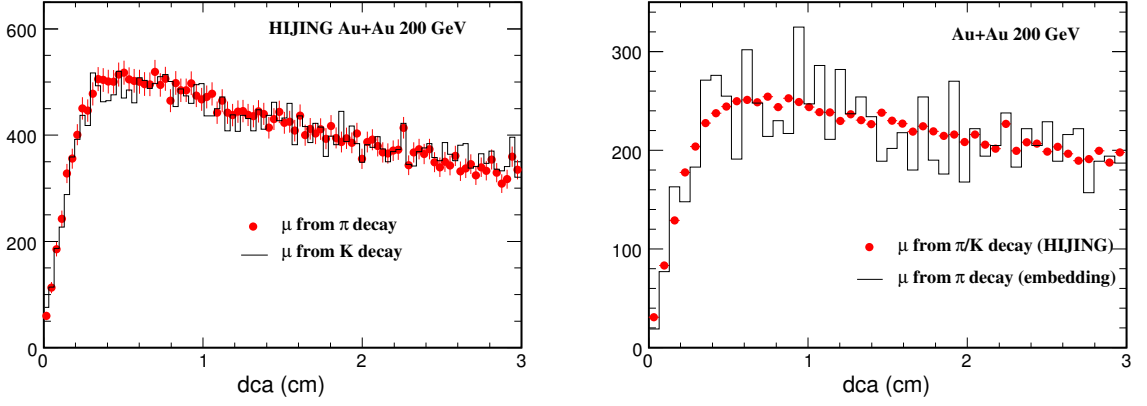
Figure 4.6: Left panel: Background muon DCA distributions from pion decay (circle) and kaon decay (histogram). Right panel: Background muon DCA distributions from HIJING simulation (circle) and embedding (histogram).

decay partial widths (Γ) of the three dominant decay channels are:

1. $K + l + \nu$ with pseudo scalar meson in final state ($D^{\pm}$ B.R.=7.8%)

$$\frac{d\Gamma}{dq^2} \propto \frac{p_k^3}{(1 - q^2/M^{*2})^2}$$

   where q^2 is the invariant mass of the virtual $W \to \nu l$, p_K is the momentum of the kaon, and $M^* = 0.189$ GeV/c^2 is a parameterization of the effective pole mass in the decay.

2. $(K\pi) + l + \nu$ with non-resonant $K\pi$ in final state($D^{\pm}$ 4.0%)

   We use the K^* mass (0.892 GeV/c^2) for the $K\pi$ invariant mass and the form factor is the same as in the decay to the pseudo scalar meson.

3. $K^* + l + \nu$ with vector meson in final state($D^{\pm}$ 5.5%)

$$\frac{d\Gamma}{dq^2 d\cos\theta_l} \propto \frac{p_V q^2}{M^2}[(1-\cos\theta_l)^2|H_+(q^2)|^2 + \frac{4}{3}(1+\cos\theta_l)^2|H_-(q^2)|^2 + \frac{8}{3}\sin^2\theta_l|H_0(q^2)|^2]$$

   where θ_l is the decay angle between the lepton and the vector meson, p_V is the

vector meson momentum,

$$H_\pm(q^2) = (M + m)A_1(q^2) \mp \frac{2Mp_V}{M + m}V(q^2)$$

and

$$H_0(q^2) = \frac{1}{2mq}[(M^2 - m^2 - q^2)(M + m)A_1(q^2) - \frac{4M^2p_V^2}{M + m}A_2(q^2)]$$

where $A_{1,2}, V$ take the form of $1/(1 - q^2/M_{A,V}^{*2})$ with $M_A^* = 2.5$ GeV/c^2, $M_V^* = 2.1$ GeV/c^2 and $r_V = V(0)/A_1(0) = 1.62 \pm 0.08$, $r_2 = A_2(0)/A_1(0) = 0.83 \pm 0.05$ [PDG02, Polem].

For different charmed hadrons, we assume that the relative branching ratios among these three channels are the same, and their decay electron spectra are the same. The overall charmed hadron to electron branching ratio $\Gamma(c \rightarrow e)/\Gamma(c \rightarrow anything)$ is 10.3% [PDG02]. There is a possible $\sim 5\%$ difference between electron and muon decays due to phase space which was not taken into account in this analysis. Electrons at high momentum are mainly from decay channel (1) $K + l + \nu$ because the kaon is lighter than the K^* and the form factor of the decay channel to a vector meson ($K^* + l + \nu$) favors a low momentum lepton and higher momentum neutrino. Since PYTHIA uses a simplified vector meson decay form factor [Sj01], it tends to produce a softer electron spectrum. Both the parameterization by Cacciari [CNV05] and formulae from the PDG agree with CLEO's preliminary electron spectrum. In addition, we also find that although the charmed mesons ($D^\pm$ and D^0) from $\Psi(3770)$ decay have a momentum of 244 MeV/c only and without correction of final state radiation [CLEO04], it affects slightly its subsequent electron spectrum.

We use our electron momentum spectra and that of Cacciari to generate electron spectra from charmed decay at RHIC. A power-law function of the charmed hadron transverse momentum spectrum was obtained from minimum-bias Au+Au collisions [CQM05]. Fig. 4.7 shows the ratios of those electron spectra divided by the spectrum using PYTHIA decay form factors [Sj01, STAc05]. The slightly soft form factor of the charm semileptonic
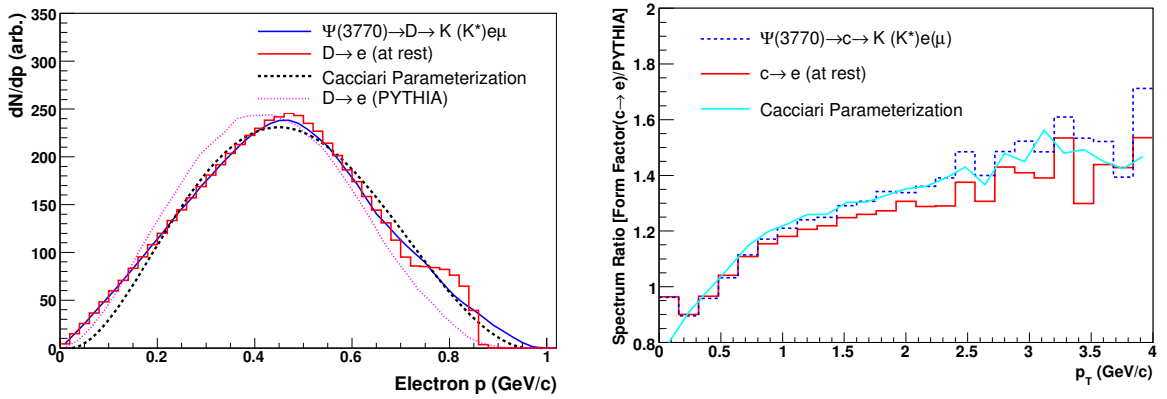
Figure 4.7: Left panel: Electron momentum spectra from charmed meson decays at rest. Histogram is the one with form factor from PDG. The dashed line is that of Cacciari's parameterization. The dotted line is from the simplified vector-meson form factor in PYTHIA. The solid line is that from the PDG which takes a form factor from $\Psi(3770) \to D \to e$. Right panel: Charm-decay electron spectra for three different form factors divided by the spectrum using the PYTHIA form factor. The histogram represents the ratio using the PDG form factor. The solid line is Cacciari's parameterization, and the dashed line is from PDG and takes a form factor from $\Psi(3770) \to D \to e$. See text for detail.

decay in PYTHIA convoluted with a steeply falling charm spectrum produces an electron p_T spectrum in Au+Au collisions at RHIC, which can be lower than the correct one by up to a factor of 1.5 at high p_T. Part of the discrepancy between experimental results and PYTHIA in electron spectra [STAc05, PHECAA] can be explained by the decay form factor. Taking $D^{\pm}$ and D^0 from $\Psi(3770)$ decay as if it were at rest, results in slight change on the electron spectrum.

In the following, if we say 'form factor decay' that means we let the charmed hadrons decay using the form factor discussed above.

4.4 Combined fit: Charm cross-section, freeze-out and flow, energy-loss

At RHIC energy, charm total cross-section have been measured from single electron spectra alone at $p_T > 0.8$ GeV/c by PHENIX. But the charmed hadron p_T spectrum is

unknown and the electron p_T region is corresponding to higher p_T of the charmed hadron spectrum. Then the charmed hadron at low p_T where the yield accounts for a large fraction of the total cross-section, is missing. The method to estimate the background from cocktail is also strongly model dependent. The direct extraction from electron spectrum will have large systematic uncertainties. STAR provided a method to extract the charm production cross-section by a combination of the directly reconstructed low p_T $D^0 \to K\pi$ and the non-photonic electron spectra [STAc05]. The D^0 measurement constrains most of the cross-section. But due to large combinatorial background, the systematic uncertainties are still large.

On the other hand, as discussed in the previous sections, STAR collaboration has measured D^0 hadronic decay channel ($0.2 < p_T < 2$ GeV/c), single muon with high precision at low p_T ($0.17 < p_T < 0.25$ GeV/c) and single electron ($0.9 < p_T < 5$ GeV/c) at 200 GeV Au+Au collisions. Charm cross-sections at mid-rapidity ($d\sigma_{c\bar{c}}^{NN}/dy$) were extracted from a combination of the three measurements covering $\sim 90\%$ of the kinematics. In this section, the detail of how we perform the fit combining all the data points from these three measurements to extract the charm cross-section will be presented. In addition, the extraction of charmed hadron freeze-out temperature and flow velocity based on blast-wave model will be discussed.

Firstly, the decay kinematics of charmed hadron to electrons were studied in previous section. The same improved charm semileptonic decay form factors were used for all charmed hadrons. Assume similar p_T spectrum shape between different charmed hadrons. And assume their decay electron spectra are similar. We applied the D^0 mass (1.863 GeV) for the form factor decay. The decay electron spectra were normalized by the D^0 fraction in total charmed hadrons from e^+e^- collisions at $\sqrt{s}=$ 91 GeV from PDG [PDG04]: $R \equiv N_{D^0}/N_{c\bar{c}} = 0.54 \pm 0.05$, and the charm branching ratio to electron ($c \to e$ $B.R. = 10.3\%$). There is $\sim 15\%$ systematical difference between charm decay to electron and muon. In the following combined-fit, the single electrons are all from charm decays (Bottom contributions will be discussed in next chapter).

A power-law function is used to create charmed hadron p_T spectra. The function takes

the form:

$$\frac{dN}{2\pi dy p_T dp_T} = \frac{dN}{dy}\frac{2(n-1)(n-2)}{\pi(n-3)^2\langle p_T\rangle^2}(1+\frac{2p_T}{\langle p_T\rangle(n-3)})^{-n},\tag{4.5}$$

where dN/dy is the yield and n and $\langle p_T\rangle$ are the parameters controlling the shape of the spectrum. A D^0 p_T distribution with a set of these parameters was used as input for form factor decay, and the decay electron spectrum was obtained. A 3-dimensional scan on the $(dN/dy, \langle p_T\rangle, n)$ "plane" was done to fit D^0 and muon/electron data points simultaneously. The point with the smallest χ^2 value was set to be the fit result. When we calculate the χ^2, we try to exclude the correlations between different measurements [?]. Correlated errors are, however, treated explicitly when there are a number of results of the form $A_i \pm \sigma_i \pm \Delta$ that have identical systematic errors Δ, where σ_i includes the statistical error and uncorrelated (bin-to-bin) systematical error. In this case, we use the quadratic sum of these errors $(\sigma_i^2 \pm \Delta_i^2)^{1/2}$, where the modified systematic error

$$\Delta_i = \sigma_i\Delta[\Sigma(1/\sigma_j^2)]^{1/2}.\tag{4.6}$$

Then χ^2 was calculated from the following equation.

$$\chi^2 = \sum_D(\frac{y_D - f_D}{\sigma_D})^2 + \sum_\mu(\frac{y_\mu - f_\mu}{\sigma_\mu})^2 + \sum_e(\frac{y_e - f_e}{\sigma_e})^2,\tag{4.7}$$

where y_D, y_μ, y_e denote the measured yields of D^0, muons and electrons. σ_D, σ_μ, σ_e denote the measured errors, where we use statistical errors only to calculate the statistical errors for the fit results and use total errors calculated as above to estimate the systematical errors for the fit results. f_D, f_μ, f_e denote the expected values from input power law function for D^0 and its decay curve respectively. To avoid the p_T position issue in large p_T bins, we used the integral yield dN instead of $dN/p_T dp_T$ in each p_T bin.

In addition, since the p_T distributions of D^0 is unknown, we also tried a blast-wave function as the input D^0 p_T distribution. The blast-wave function is written as the following: The 3 free parameters are: dN/dy, freeze-out temperature T_{fo} and collective velocity β_m, where $\langle\beta_t\rangle = \beta_m \times \frac{2}{3}$. A 3-dimensional scan on the $(dN/dy, T_{fo}, \beta_m)$ "plane"

Table 4.3: The combined fit results for D^0, muons and electrons in Au+Au collisions.

power-	measurements	$d\sigma_{c\bar{c}}^{NN}/dy$ (μb)	$\langle p_T \rangle$ (GeV)	n	χ^2/ndf
law	mb ($D^0 + \mu + e$)	$277 \pm 26 \pm 63$	$0.92 \pm 0.06 \pm 0.12$	$11.5 \pm 6.5 \pm 7$	$18.6(4.2)/11$
fit	0-12% ($\mu + e$)	$311 \pm 26 \pm 64$	$0.95 \pm 0.04 \pm 0.16$	$13 \pm 1.5 \pm 6.5$	$18.5(0.6)/8$
blast-	measurements	$d\sigma_{c\bar{c}}^{NN}/dy$ (μb)	T_{fo} (MeV)	$\langle \beta_t \rangle$	χ^2/ndf
wave	mb ($D^0 + \mu + e$)	$271 \pm 24 \pm 57$	222	$0.27 (< 0.60)$	$13.9(3.2)/8$
fit	0-12% ($\mu + e$)	$283 \pm 21 \pm 61$	220	$0.35 (< 0.63)$	$45.2(2.3)/5$

was also performed to fit D^0 and muon/electron data points simultaneously. The way to calculate errors and χ^2 is the same as above.

The error estimation was through the contour scan in the 3-D "plane" with the $\chi^2 = \chi^2_{min} + 1$. The error of dN/dy was then obtained by projecting this 3-D contour into dN/dy axis.

Once the dN/dy was extracted, the charm production cross-section per nucleon-nucleon interaction at mid-rapidity can be calculated from Eq. 4.8:

$$\frac{d\sigma_{c\bar{c}}^{NN}}{dy}\Big|_{y=0} = \frac{dN_{D^0}}{dy}\Big|_{y=0} \times R \times \frac{\sigma_{inel}^{pp}}{\langle N_{bin} \rangle}. \tag{4.8}$$

In this equation, the factor R is the D^0 fraction in total charmed hadrons, as mentioned before. The number of binary collisions N_{bin}, which is from Glauber calculations, is 293 ± 35 for 0-80% minbias Au+Au collisions and is 900 ± 71 for 0-12% central Au+Au collisions.

Table 4.3 lists all the fitting results.

Fig. 4.8 shows D^0, muons spectra and centrality dependence of non-photonic electrons spectra and the combining fit results for D^0, muons and electrons spectra in Au+Au collisions.

Within errors, both power-law fit and blast-wave fit give the similar $d\sigma_{c\bar{c}}^{NN}/dy$. Therefore, by averaged the two fits, $d\sigma_{c\bar{c}}^{NN}/dy$ is presented to be 274±25(stat.)±60(sys.) μb in minbias Au+Au and 297±24±63 μb in 0-12% central Au+Au collisions at $\sqrt{s_{NN}}$=200 GeV. The total charm cross-section per nucleon-nucleon collision ($\sigma_{c\bar{c}}^{NN}$) following the
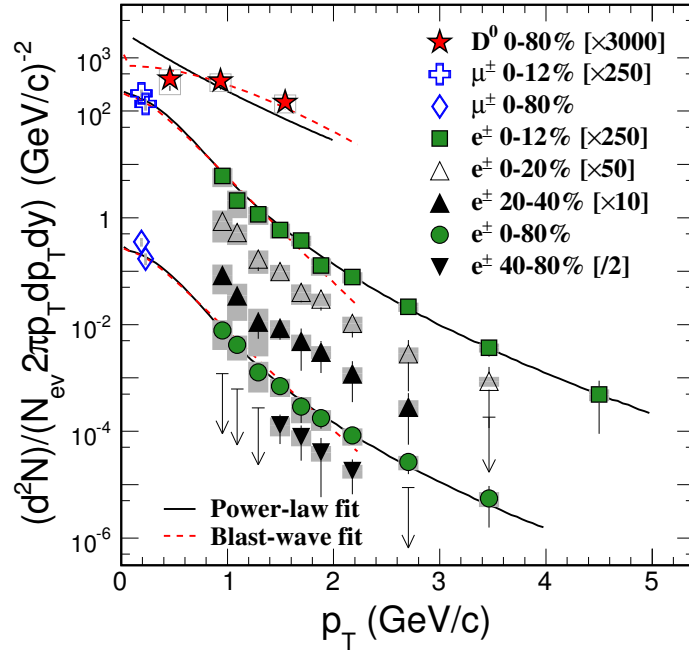
Figure 4.8: D^0 spectrum in minbias Au+Au collisions (star), muons spectra in minbias (diamond) and 0-12% (open cross) Au+Au collisions. Centrality dependence of non-photonic electron spectra. Solid curves show the power-law combined fit results. Dashed curves are from the blast-wave combined fit.

method addressed in Ref. [STAc05] is presented to be 1.40±0.11(stat.)±0.39(sys.) mb in 0-12% central Au+Au and 1.29±0.12±0.36 mb in minbias Au+Au collisions at $\sqrt{s_{NN}}$=200 GeV. Fig. 4.9 shows the $d\sigma_{c\bar{c}}^{NN}/dy$ as a function of $N_{\rm bin}$ for minbias d+Au, minbias Au+Au and 0-12% central Au+Au collisions. It can be observed that the charm cross-section seems to follow $N_{\rm bin}$ scaling from d+Au [STAc05] to Au+Au collisions which supports the conjecture that charm quarks are produced at early stages in relativistic heavy-ion collisions. However, the recent cross-section result from PHENIX is a factor of 2 lower than STAR and the FONLL (NLO) calculations [CNV05, Vog02, Vog03] shown as the band, which under-predicts the minbias data by a factor of $5.1 \pm 0.48(stat.) \pm 1.2(syst.)^{+6.8}_{-3.1}(theory)$.
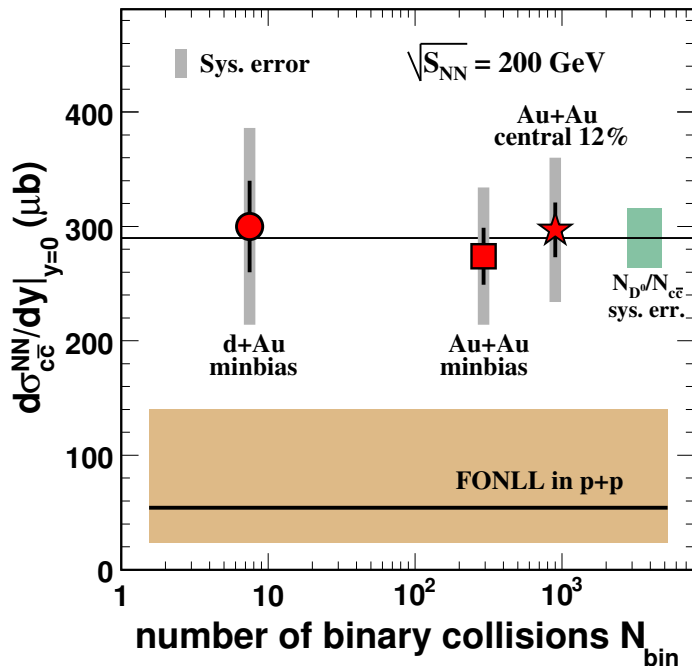
Figure 4.9: Mid-rapidity charm cross-section per nucleon-nucleon collision as a function of number of binary collisions ($N_{\rm bin}$) in d+Au, minbias and 0-12% central Au+Au collisions. R factor is the D^0 fraction in total charmed hadrons. The solid line is from the average of the three values. Within the errors, the measured cross-sections are consistent with the number of binary collisions scaling. FONLL prediction, shown as the band, under-predicts the charm cross-section for collisions at RHIC.

The nuclear modification factor ($R_{AuAu/dAu}$) [Adl02a] for single muon (open crosses) and non-photonic electron $R_{AuAu/dAu}$ (solid squares) are shown in Fig. 4.11. The $R_{AuAu/dAu}$

are obtained taking the ratio of the p_T spectra in 0-12% central Au+Au collisions and the N_{bin} scaled decay electron spectra in d+Au collisions. The decay d+Au electron spectra curve is from the combined fit with both TOF and EMC data [STACRAA, PHECRAA], see Fig. 4.10. The bin-by-bin errors from the fit are propagated in the systematic errors of the $R_{AuAu/dAu}$.
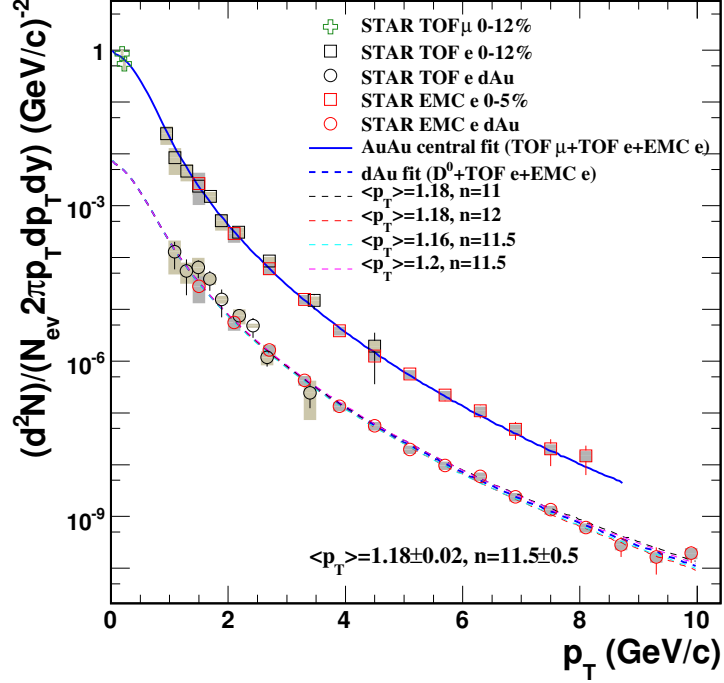
Figure 4.10: Single electron spectra measured from TOF are consistent with EMC results. In order to reduce the errors of the reference spectrum in d+Au collisions, a combined fit was performed to fit both TOF data points and EMC data points. The variation of the power-law parameters in $1 - \sigma$ was applied to propagate the uncertainties of the spectra shape.

The muon $R_{AuAu/dAu}$ at low p_T is consistent with unity considering uncertainties. The non-photonic electron $R_{AuAu/dAu}$ in 0-12% central Au+Au collisions is observed to be significantly below unity at $1 < p_T < 5$ GeV/c and is suppressed as strongly as that of light hadrons [Lqe06], which indicates a large amount of energy-loss for heavy quarks in central Au+Au collisions. The measurement of non-photonic electron at high p_T from STAR EMC also shows strong suppression [STACRAA, PHECRAA]. Theoretical calculations [Arm05, DGW05] considering only the charm contributions to the non-photonic electrons agree with the measured non-photonic electron $R_{AuAu/dAu}$, while calculations

with single electrons decayed from both bottom and charm quarks give larger $R_{AuAu/dAu}$ values. The discrepancy from pQCD calculation assuming only gluon radiative energy-loss challenges our understanding of the detailed mechanisms of quark and gluon energy-loss in strongly interacting matter. Model calculations incorporating in-medium charm resonances/diffusion or collisional dissociation can reasonably describe the non-photonic electron spectra [MT05, HGR06, Rap06, Vit06], see Fig. 4.11.
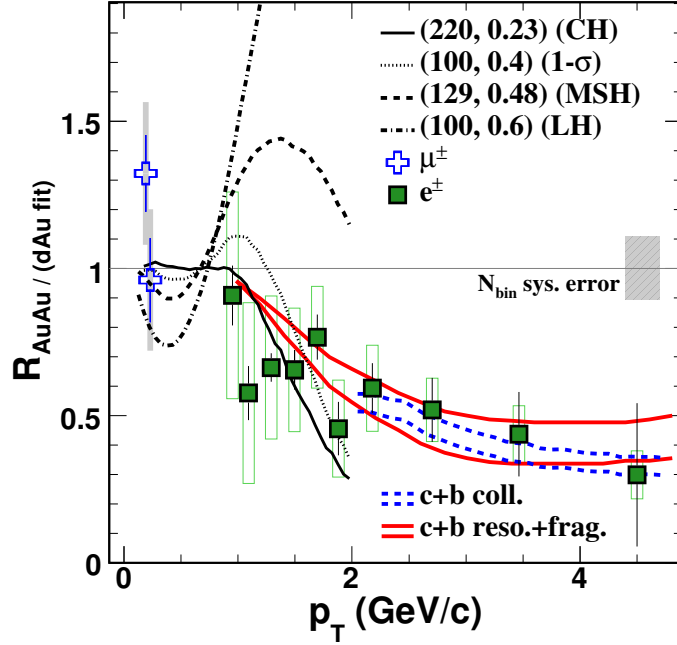
Figure 4.11: Nuclear modification factor ($R_{AuAu/dAu}$) of the spectra in $0 - 12\%$ Au+Au collisions divided by corresponding spectra in d+Au collisions. Bin to bin systematic errors are represented by the open boxes. Box on the right at unity shows the common normalization uncertainty in N_{bin}. Model calculations are presented: coalescence and fragmentation [Rap06] (double-solid lines), and collisional dissociation of heavy meson [Vit06] (double-dashed lines). The solid, dashed and dot-dashed lines are Blast-Wave calculations with different freeze-out parameters of (T_{fo} in MeV, $\langle \beta_t \rangle$) for charmed hadrons (CH,$1 - \sigma$), multi-strange hadrons (MSH) and light hadrons (LH), respectively.

The precise measurement of charmed hadron flow properties are expected to be a good test for partonic thermalization. The solid curve in Fig. 4.11 from bast-wave model with the parameters (T_{fo}=129 MeV, $\langle \beta_t \rangle$= 0.477) for multi-strange hadrons cannot describe the data. The parameters obtained from pion, kaon and proton spectra (T_{fo}=100 MeV,

$\langle\beta_t\rangle$= 0.6, dot-dashed curve) show even larger discrepancy [LZZX06, Ada04a]. Due to the smearing of the charm semileptonic decay kinematics, only qualitative conclusion can be reached, that the charm spectra are not consistent with large flow and late freeze-out. Bast-wave parameters with low temperature and moderate radial flow(dotted line), or with high temperature and low radial flow (dashed line) can describe our results. The data are also consistent with the dynamical models [MT05, HGR06, Rap06, Vit06] using finite charm interaction cross-section in a strongly interacting medium. This may connect the freeze-out parameters (temperature and flow velocity) to the drag constant in those dynamical models. Future upgrades with a direct reconstruction of charmed hadrons are crucial for more quantitative answers [STA05].

In summary, we report measurements of charmed hadron production at mid-rapidity from analysis of $D \to K\pi$, muons and electrons from charm semileptonic decays in minbias and central Au+Au collisions at RHIC. The transverse momentum spectra from non-photonic electrons are strongly suppressed at $1 < p_T < 5$ GeV/c in Au+Au collisions relative to those in d+Au collisions. For electrons with $p_T{\sim}2$ GeV/c, corresponding to charmed hadrons with $p_T{\sim} 3 - 5$ GeV/c, the suppression is similar to that of light baryons and mesons. Detailed model-dependent analysis of the electron spectra with $p_T < 2$ GeV/c indicates that charmed hadrons have a different freeze-out pattern than the more copiously produced light hadrons. Charm differential cross-sections at mid-rapidity $(d\sigma_{c\bar{c}}^{NN}/dy)$ are extracted from a combination of the three measurements covering $\sim 90\%$ of the kinematics. The cross-sections are found to follow binary scaling as a signature of charm production exclusively at the initial impact. This supports the assumption that hard processes scale with binary interactions among initial nucleons and charm quarks can be used as a probe sensitive to the early dynamical stage of the system.

CHAPTER 5

Discussion

5.1 Heavy flavor energy loss

As we discussed in the introduction chapter, the energy loss of heavy quarks is considered as a unique tool to study the interactions between heavy quarks and the medium created in the heavy-ion collisions, and provide us important information of the medium properties. Experimentally, the high p_T modifications of heavy flavor hadron (D-mesons, B-mesons, *etc.*) yields are expected to be the direct variables to reveal heavy quark energy loss. But in current STAR experiment, it is very difficult to topologically reconstruct D-mesons or B-mesons. And due to large random combinatorial background, the same- and mixing-event method can only provide the D^0 p_T spectrum below 2 GeV/c with large systematical uncertainties in minimum bias Au+Au collisions. In central Au+Au collisions, the combinatorial background becomes even larger, the signals are not good enough to extract useful information. Due to small acceptance, direct measurement of heavy flavor hadrons in PHENIX experiment becomes even harder. Nevertheless, the measurements of single electron from heavy quark decays were used as the indirect substitute.

The single electron strong suppression, similar to light hadrons, was observed in recent measurements [STACRAA, PHECRAA]. Fig. 5.1 shows the nuclear modification factor of single muons (open crosses) and electrons (solid squares), $R_{AuAu/dAu}$ as a function of p_T measured from STAR TPC+TOF detector. The $R_{AuAu/dAu}$ are obtained using d+Au fit curve as reference, which has been discussed in previous section. The PHENIX result [PHECRAA] and STAR EMC result [STACRAA], R_{AA} which use electron spectra measured in $p+p$ collisions as references, are shown as open circles and solid circles for

comparison. Within errors, these results are consistent in different experiments. The $R_{AuAu/dAu}$ may show some Cronin effect [Cro73, Rua04b, Xin05] due to enhancement in d+Au collisions relative to p+p collisions $R_{dAu} > 1$. But this effect is not significant compared to huge error bars.
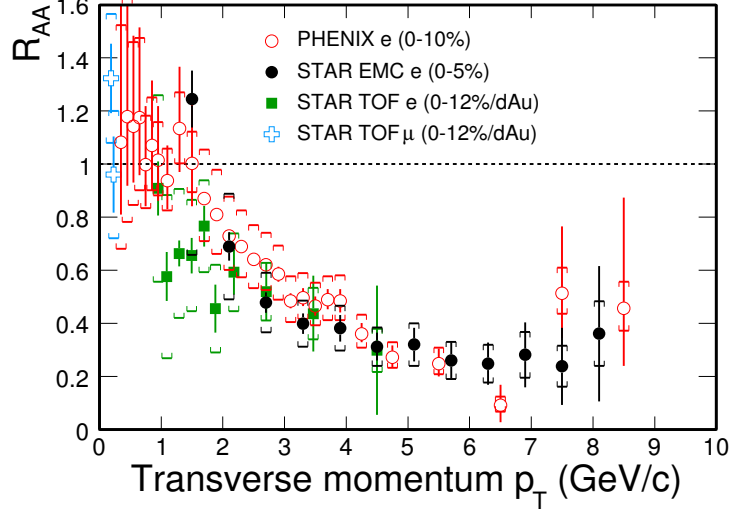
Figure 5.1: Nuclear modification factors of single electrons as a function of p_T.

There are still some outstanding issues: how can the behavior of heavy flavor decay electrons reflect heavy quarks? Is the medium also opaque to heavy quarks? What is the contribution of bottom in single electron measurements?

Fig. 5.2 shows the 2D-scattering plot of D-meson p_T(D) versus decay electron p_T(e) from form factor decay. The inserted small panel shows the D-meson p_T(D) distributions when select electron at $1.45 < p_T(e) < 1.55$ GeV/c. $\sim 92\%$ yields of D-meson are from $1 < p_T(D) < 4$ GeV/c. This indicates that the p_T correlation between single electrons and their parent D-mesons is weak.

On the other hand, due to large mass and small radiative angle, heavy quarks are predicted to lose less energy than light quarks via only gluon radiation – the "dead cone" effect [DK01]. Many theoretical calculations tried to explain the single electron strong suppression observed in experiments. A collisional (elastic) energy loss has been proposed to be taken into account for heavy quark energy loss calculations.

Fig. 5.3 shows some recent theoretical calculations for single electron R_{AA} from heavy
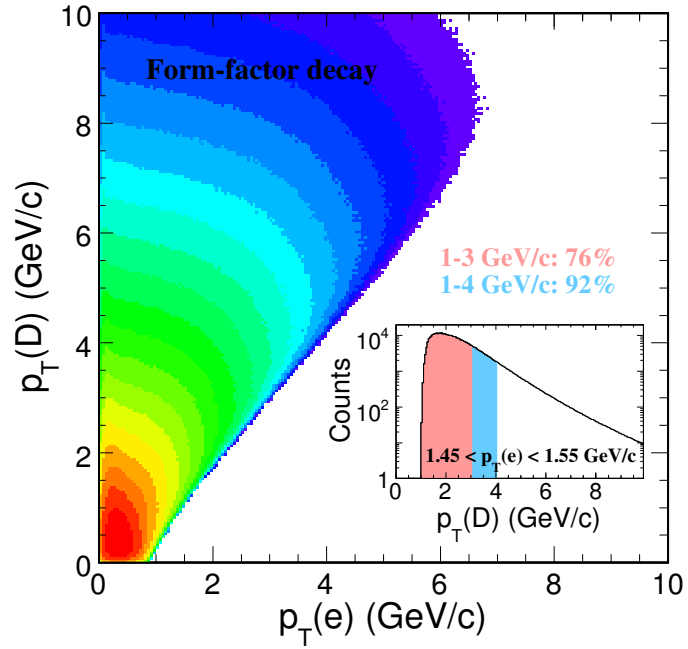
Figure 5.2: 2D-scattering plot of D-meson $p_T(D)$ versus electron $p_T(e)$ from form factor decay.
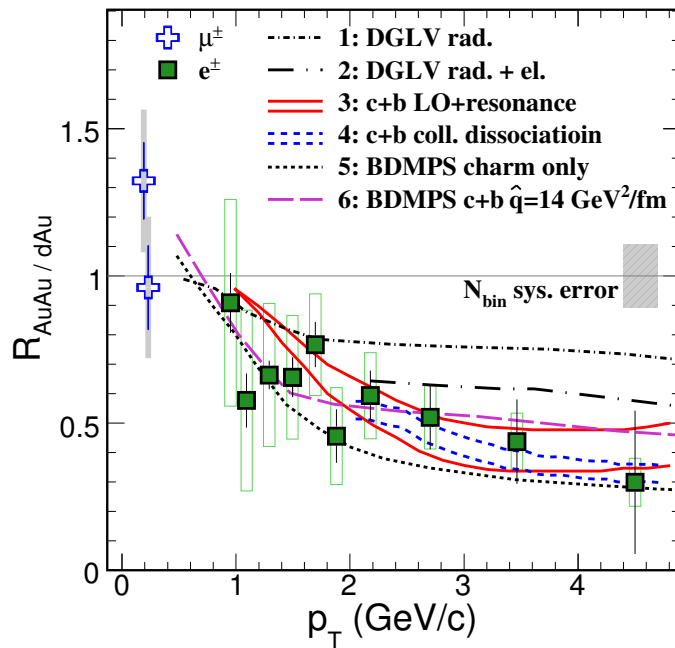
Figure 5.3: Theoretical calculations for single electron R_{AA} compared to data.

flavor semi-leptonic decays. The DGLV radiative energy loss via few hard scatterings with initial gluon density $dN_g/dy = 1000$ [DGV06] predicts significantly less suppression than data, shown as curve 1. The curve drops dramatically after including collisional energy loss [Wic05], shown as curve 2, but still predicts less suppression than observed. Curve 3, which has a good agreement with data, is from the calculation of heavy quark energy loss via elastic scattering mediated by resonance excitations of D- and B- mesons and LO pQCD gluon exchange, and including heavy-light quark-coalescence at hadronization [Rap06]. The double curves indicate the uncertainties from the calculation assuming the D- and B- resonance width $\Gamma = 0.4 - 0.75$ GeV. Curve 4 shows the calculation of single electron suppression from collisional dissociation of heavy mesons in QGP by deriving heavy meson survival and dissociation probability from the collisional broadening of their light cone wave function [Vit06]. The double-curve indicate the uncertainties from tuning the typical value of $\xi \sim 2 - 3$. This calculation also shows consistent suppression with data. Curve 5 is for single electron only from D-meson decays with only radiative energy loss from BDMPS calculations via multiple soft collisions [Arm06]. Curve 6 is the same calculation as curve 5 except that it includes electron from B-meson decays. And assumes the transport coefficient $\hat{q} = 14$ GeV^2/fm [Arm06]. Both BDMPS calculations agree with data.

There are still a few assumptions and uncertainties in theory. Several different processes can describe data within the large experimental uncertainties. The exact mechanism of heavy quark energy loss is still under intense theoretical and experimental investigations.

5.2 Heavy flavor collectivity

Theoretical calculations have shown that interactions between the surrounding partons in the medium and heavy quarks could change the measurable kinematics [MT05, HGR06, DDZ06], and could boost the radial and elliptic flow resulting in a different heavy quark p_T spectrum shape. Fig. 5.4 shows the picture that heavy quarks participate in collective

motion. We can simply treat heavy quark as an intruder, put into the hot medium with relatively very high density of light quarks. Due to their large mass and partonic density gradient, such a heavy quark may acquire flow from the sufficient interactions with the constituents of a dense medium in analog to Brownian motion. We expect that bottom quark has small collective velocity due to its extremely large mass and small interaction cross section.
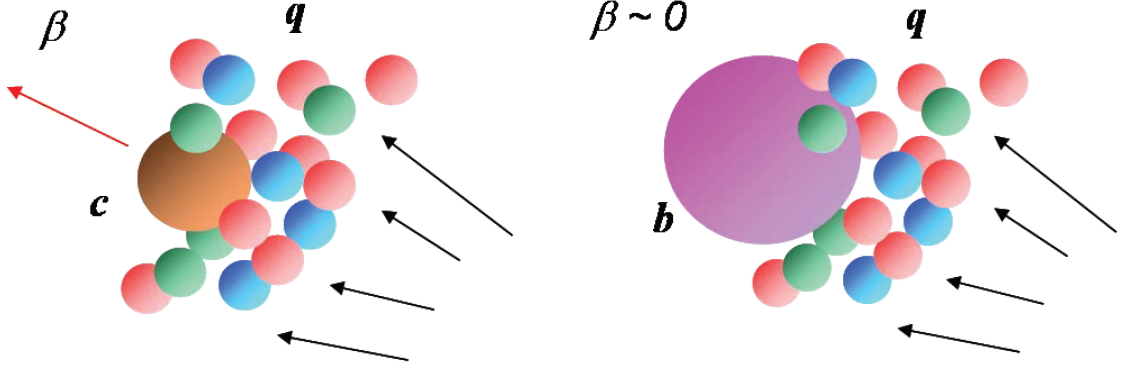
Figure 5.4: Heavy quarks (c, b) participate in the collective motion.

Base on blast wave model [SSH93] discussed in previous section, a combined fit was performed to describe the spectral shape and to provide the freeze-out temperature T_{fo} and collective velocity $\langle \beta \rangle$. Fig. 5.5 shows the 2D distribution of T_{fo} versus β_m ($\langle \beta \rangle = \frac{2}{3}\beta_m$) extracted from the combined fit to muon and electron spectra measured in $0-12\%$ central Au+Au collisions. The best fit with minimum χ^2 gives the parameters as: $T_{fo} = 220$ MeV and $\langle \beta_t \rangle = 0.23$. The 1-$\sigma$ (dotted curve) and 2-σ (white solid curve) contours are from combined fits with statistical errors only. Black solid curve is for the 1-σ contour from combined fit with both statistical errors and systematical errors. The fit results are not sensitive to T_{fo}, and $\langle \beta \rangle$ is smaller than that of light hadrons. One can also see that T_{fo} and β_m are strongly correlated.

To understand whether charmed hadrons may have similar radial flow as lighter hadrons, the blast wave fit result of charmed hadrons was compared to multi-strange hadrons and light hadrons (π,K,p). Fig. 5.6 (a) shows these comparisons. Solid curve shows the blast wave fit for charmed hadrons ($T_{fo} = 220$ MeV and $\langle \beta_t \rangle = 0.23$). The

80
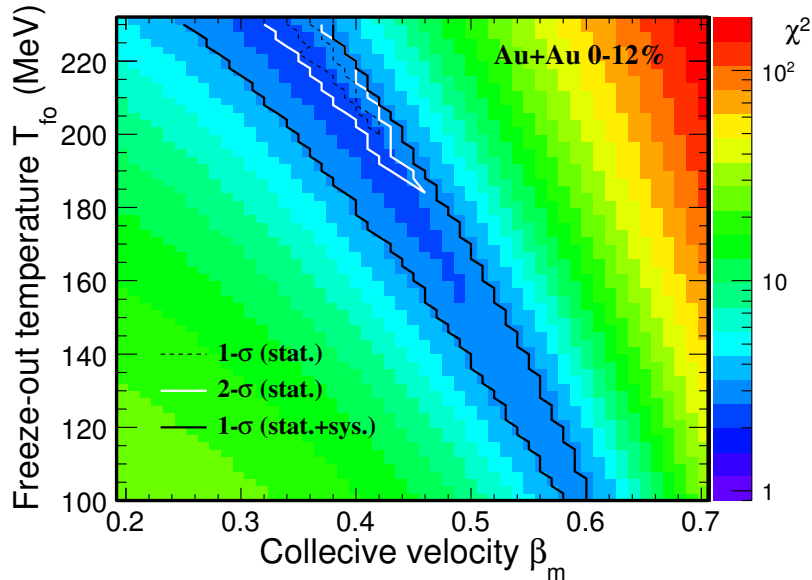
Figure 5.5: Blast wave parameters T_{fo} versus β_m and 1-σ contours from the combined fit to muon and electron spectra in 0-12% central Au+Au collisions.

blast wave fit parameters for multi-strange hadrons (short-dashed curve) are $T_{fo} = 129$ MeV and $\langle \beta_t \rangle = 0.48$, and for light hadrons (short-dot-dashed curve) are $T_{fo} = 100$ MeV and $\langle \beta_t \rangle = 0.6$. The long-dot-dashed curve, as a reference, is from a power law combined fit ($\langle p_T \rangle = 1.18 \pm 0.02$, $n = 11.5 \pm 0.5$) to both TOF and EMC data in d+Au collisions, also shown in Fig. 4.10. All these curves are scaled to match the measured cross sections. One may consider these comparisons highly model dependent. In principle, we can directly compare the nuclear modification function between Omega and charmed hadrons since their masses are very similar. In practice, we take the blast-wave fit to Omega, which describes the Omega data well, and apply the charmed hadron semileptonic decay to obtain lepton spectra if the Omega and charmed hadrons would have the same freeze-out properties. This comparison is practically independent of model.

The short-dashed curve in Fig. 5.6 (b) from blast-wave model with the parameters ($T_{fo} = 129$ MeV, $\langle \beta_t \rangle = 0.48$) for multi-strange hadrons cannot describe the data [HYP06]. The parameters obtained from pion, kaon and proton spectra ($T_{fo} = 100$ MeV, $\langle \beta_t \rangle = 0.6$, short-dot-dashed curve) show even larger discrepancy [Adl02a]. Due to the smearing of the charm semileptonic decay kinematics, only the qualitative conclusion that the charm
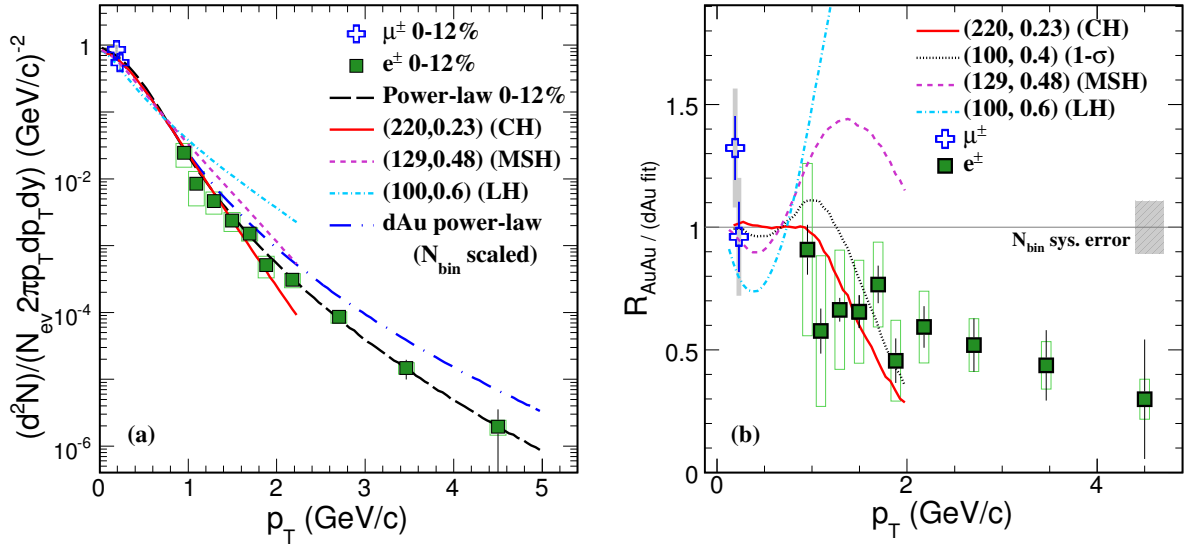
Figure 5.6: Panel (a): Different sets of blast wave parameters compared to measured lepton p_T spectra. The solid, short-dashed and short-dot-dashed curves are blast-wave calculations with different freeze-out parameters of (T_{fo} in MeV, $\langle \beta_t \rangle$) for charmed hadrons (CH), multi-strange hadrons (MSH) and light hadrons (LH), respectively. The long-dot-dashed curve is the power law decay curve fit to d+Au data. Bin to bin systematic errors are represented by the gray bands for muons and open boxes for electrons. Panel (b): Nuclear modification factor ($R_{AuAu/dAu}$) of the spectra in $0-12\%$ Au+Au collisions divided by corresponding power law decay curve fit to d+Au data. Box on the right at unity shows the common normalization uncertainty in N_{bin}. The curves show the ratio of blast wave fit results and d+Au power law, corresponding to panel (a).

spectra are not consistent with large flow and late freeze-out can be drawn. Bast-wave parameters with low temperature and moderate radial flow(dotted curve), or with high temperature and low radial flow (solid curve) can describe our results. This may indicate that charmed hadrons interact and decouple from the system differently from lighter hadrons. Future upgrades with a direct reconstruction of charmed hadrons are crucial for more quantitative answers [STA05].

5.3 Charm production cross-section – consistency and discrepancy

We reported the charm cross sections from a combination of three independent measurements: $D \rightarrow K\pi$, muons and electrons from charm semileptonic decays in minbias and central Au+Au collisions at RHIC. While the discrepancy between STAR and PHENIX also exists. We perform a detailed comparison in this section.

Charm total cross sections have been extracted from single electron spectra alone at $p_T > 0.8$ GeV/c by PHENIX. The single electron spectrum from charmed hadron decay peaks at $p_T \sim 0.5$ GeV/c and therefore a large fraction of the total cross section is missing from the measurement. Recently, PHENIX reported new charm total cross section in $p+p$ collisions from single electron spectrum at $p_T > 0.3$ GeV/c. In all the cases, the inclusive electron spectrum contains photonic background. The photonic background level in this p_T range is comparable to STAR electron photonic background level at high p_T. Cocktail and converter methods have been used by PHENIX to obtain the background.

In this thesis, the charm cross sections are reported from combined three independent measurements: $D^0 \rightarrow K\pi$, low p_T muons and single electrons in STAR experiments. Currently, the consistencies within STAR experiments are observed, while the discrepancy between STAR and PHENIX still exists.

The comparison of the single muon/electron spectra measured from STAR TOF detector and the single electron spectrum measured from EMC detector in 0-12% and 0-5%

central Au+Au collisions, respectively, is shown in Fig. 4.10. These data points are scaled by N_{bin} since they are from different centralities. In order to see the comparison more clearly, we take the ratio of the data and the fit curve, see Fig. 5.7. Since EMC results have smaller errors, so it constrains the fit curve, thus the EMC data points are around unity and TOF result is a little higher, probably due to 0-5% has more suppression than 0-12%. But within errors, the results from two independent measurements are consistent.
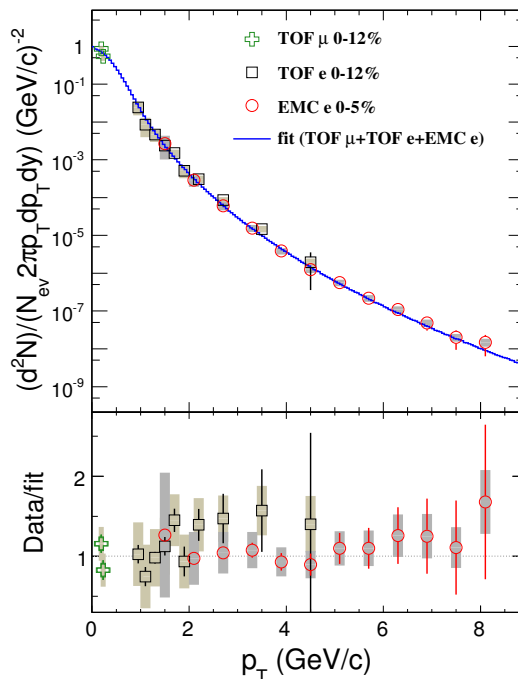
Figure 5.7: The comparison of the single muon (open crosses) and electron (open squares) spectra measured from STAR TOF detector and the single electron spectrum (open circles) measured from EMC detector in 0-12% and 0-5% central Au+Au collisions, respectively. The curve shows the fit to all the data points. Bottom panel shows the ratio of data and the fit curve.

In Fig. 5.8 (a), the single electron spectrum from PHENIX measurement in $p+p$ collisions, shown as triangles, has similar shape but systematically lower than STAR measurements, while STAR TOF result (circles) is consistent with STAR EMC result (diamonds) within errors. STAR TOF muon measurement (crosses) has also good agreement with STAR TOF electron measurement (squares) in 0-12% central Au+Au collisions. A form factor decay combined fit (solid curve) describes both low p_T muons and higher p_T electrons and gives the charm cross section at mid-rapidity as 297 mb. In addition, STAR

muons can not be fitted together with PHENIX electrons (scaled by N_{bin}), see the dashed curve, which is mostly constrained by PHENIX electron data points with small errors. PHENIX published charm cross section is 123 mb. The cross section from fit to PHENIX data only is 131 mb. And the fit combining STAR Au+Au muons and PHENIX electrons gives 137 mb with large χ^2. The PHENIX cross sections are systematically a factor of 2 lower than STAR. But both STAR and PHENIX are self-consistent in different collisions. Both observed the number of binary collisions scaling behavior of charm cross section. Fig. 5.8 (b), which shows the charm cross section at mid-rapidity as a function of number of binary collisions for STAR (circles), PHENIX (triangles) and FONULL calculations (solid line and dashed box), clearly summarizes the consistency and discrepancy among different data sets and theories.
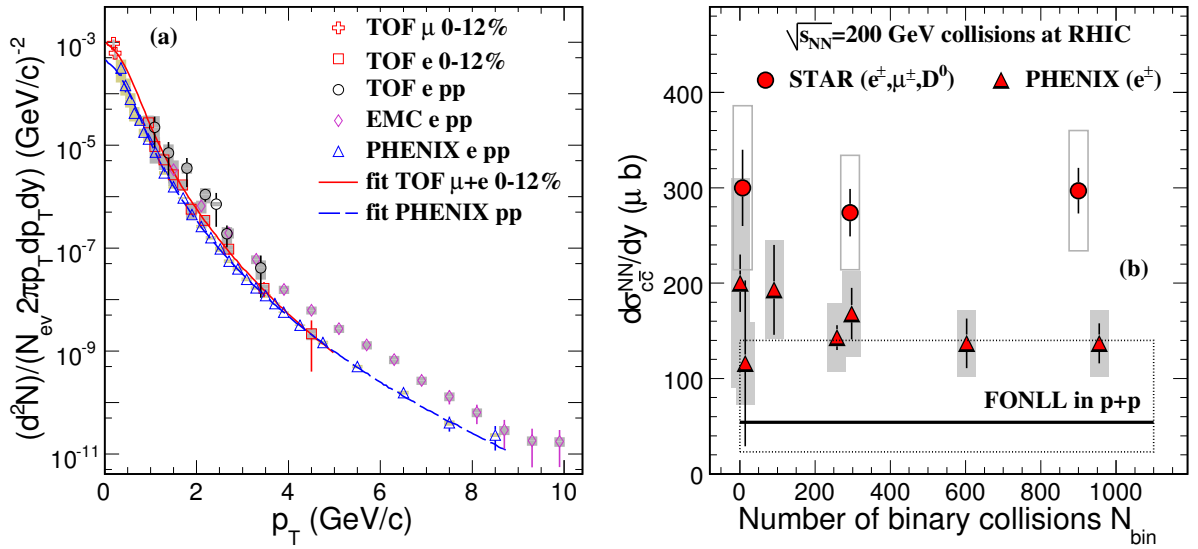
Figure 5.8: Panel (a) Spectra comparisons between STAR and PHENIX. Spectra measured in $p+p$ collisions are scaled by N_{bin} to compare with central results. Curves, from power law charmed hadron distributions via form factor decay, are used to fit data. Panel (b): The comparisons of charm cross section at mid-rapidity in different centralities and different measurements. FONULL calculation is shown as the solid line for comparison, and the dashed box stands for the uncertainties of theory.

The FONLL and NLO pQCD calculations [CNV05, Vog02, Vog03] underpredict the STAR minbias data by a factor of $5.1 \pm 0.48(stat.) \pm 1.2(syst.)^{+6.8}_{-3.1}(theory)$. As discussed previously [Xin05], theoretical calculations tuned parameters to match the low energy

measurements and then extrapolated to high energies, and the parameters are probably energy dependent but not understood well yet. The charm cross section will be precisely measured with a direct reconstruction of charmed hadrons in the future, more detail will be discussed in the outlook chapter.

The mid-rapidity charm cross-section per nucleon-nucleon collision ($d\sigma_{c\bar{c}}^{NN}/dy$) can be converted to the total charm cross-section per nucleon-nucleon collision ($\sigma_{c\bar{c}}^{NN}$) following the method addressed in Ref. [?]. The $\sigma_{c\bar{c}}^{NN}$ is presented to be $1.40\pm0.11(stat.)\pm0.39(sys.)$ mb in $0-12\%$ central Au+Au and $1.29\pm0.12\pm0.36$ mb in minbias Au+Au collisions at $\sqrt{s_{NN}} = 200$ GeV. But the different widths of the rapidity distributions from theoretical models will lead to substantial systematical uncertainties. Fig. 5.9 shows the charm cross sections as a function of rapidity distributions measured from STAR and PHENIX, compared to theoretical models [Vog04, RP03, BCH03]. Here the systematical uncertainties are dominant. PHENIX forward muon measurement [PHEMu] with large errors, shown as the solid triangle at rapidity ~ 1.6, gives consistent result with STAR, which is also significant higher than theoretical predictions.
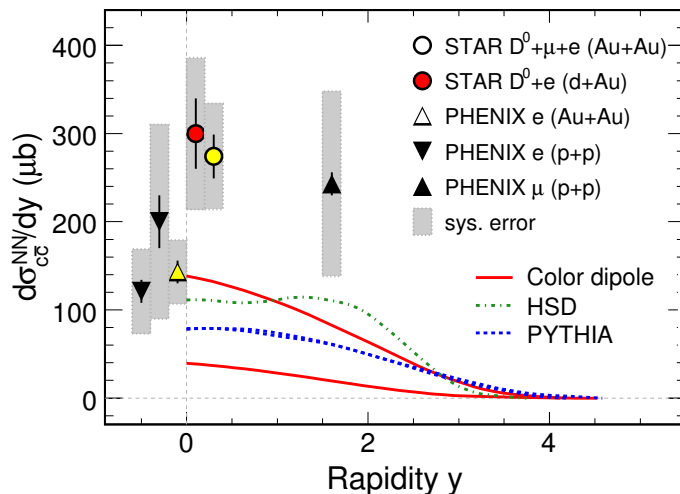
Figure 5.9: Charm cross sections as a function of rapidity distributions measured from STAR and PHENIX, compared to theoretical models.

5.4 Identify bottom contribution in non-photonic electron spectra and v_2 from Au+Au collisions at RHIC

In the above discussions, the bottom contribution to the non-photonic electron spectrum is neglected. We have discussed in the introduction chapter that the separation of bottom and charm contributions in current non-photonic electron measurements is very difficult. There are large uncertainties in the model predictions for charm and bottom production in high-energy nuclear collisions. And many theoretical calculations with charm or with both charm and bottom contributions describe the non-photonic electron suppression [DGV06, Wic05, Rap06, Vit06, Arm06] and v_2 [GKR04, ZCK05, HGR06]. Thus identification of bottom from the non-photonic electron measurements is crucial to better understand charm physics. In this section, we try a fit to non-photonic electron spectrum and estimate the bottom contributions. We also compare the v_2 distribution from simulation to the experimental data and estimate the possible charm v_2.

5.4.1 Fit to non-photonic electron spectrum and relative cross section ratio

The non-photonic electron spectrum up to 10 GeV/c has been measured by STAR experiment in 200 GeV $p+p$ collisions. The idea is that we use the sum of electron spectra from both charm and bottom decays in PYTHIA model [Sj01] to fit the STAR $p+p$ data [STACRAA] to extract the fraction of the bottom contribution. As we discussed previously, the D-mesons and their decay electrons spectra from default PYTHIA parameters are soft [LZZX06], see Fig. 4.7. Thus a modified Peterson Fragment Function (FF) and the high p_T tuned parameter are used to make spectra harder to be comparable with the form factor decays [LXY04].

Table 5.1 lists the parameter initialization for PYTHIA 6.131:

Fig. 5.10 (a) shows the p_T distributions of the heavy flavor hadrons and their decay electrons from PYTHIA with above parameters. The D-meson spectrum, shown as the

Table 5.1: PYTHIA parameters for heavy flavor decays.

Parameter	Value
MSEL	4 (charm), 5 (bottom)
quark mass	$m_c = 1.25$, $m_b = 4.8$ (GeV)
parton dist. function	CTEQ5L
Q^2 scale	4
K factor	3.5
$\langle K_t \rangle$	1.5
Peterson Frag. function	$\varepsilon = 10^{-5}$
high p_T tuned PARP(67)	4

hatched band, is normalized to

$$dN/dy = dN/dy(D^0)/\langle N_{bin} \rangle / R_{dAu}/R, \qquad (5.1)$$

where $dN/dy(D^0) = 0.028 \pm 0.004 \pm 0.008$ measured in d+Au collisions [STAc05]. $\langle N_{bin} \rangle = 7.5 \pm 0.4$ in d+Au collisions. $R_{dAu} = 1.3 \pm 0.3$ [Xin05]. R factor stands for D^0 fraction in total charmed hadrons, the fragmentation ratio $R(c \rightarrow D^0) \equiv N_{D^0}/N_{c\bar{c}} = 0.54 \pm 0.05$ [PDG04]. All these normalization errors are propagated into the uncertainty band of the D-meson spectrum. The curve in this band is the lower limit of the D-meson spectrum in our simulation. Correspondingly, its decay electron spectrum is shown as the solid band. The non-photonic electron spectrum measured in p+p collisions at STAR [STACRAA] is shown as the open squares. The decay electron band alone can describe the data, indicating that the contribution of electrons from bottom decay could be very small. In order to estimate the upper limit of bottom contribution, we use the lower limit of the decay electron spectrum, shown as the open circles. B-meson spectrum (solid curve) and its decay electron spectrum (open triangles) are normalized by varying the ratio of $\sigma_{b\bar{b}}/\sigma_{c\bar{c}}$. The summed spectrum (solid circles) by combining the lower limit of $D \rightarrow e$ and $B \rightarrow e$ is used to fit STAR data in p+p collisions, and then the upper limit of $B \rightarrow e$ contribution will be extracted.

Fig. 5.11 (a) shows the fit χ^2 as a function of the unique variable $\sigma_{b\bar{b}}/\sigma_{c\bar{c}}$. The best fit with a minimum $\chi^2/ndf = 16.6/14$ gives the upper limit of the total cross section
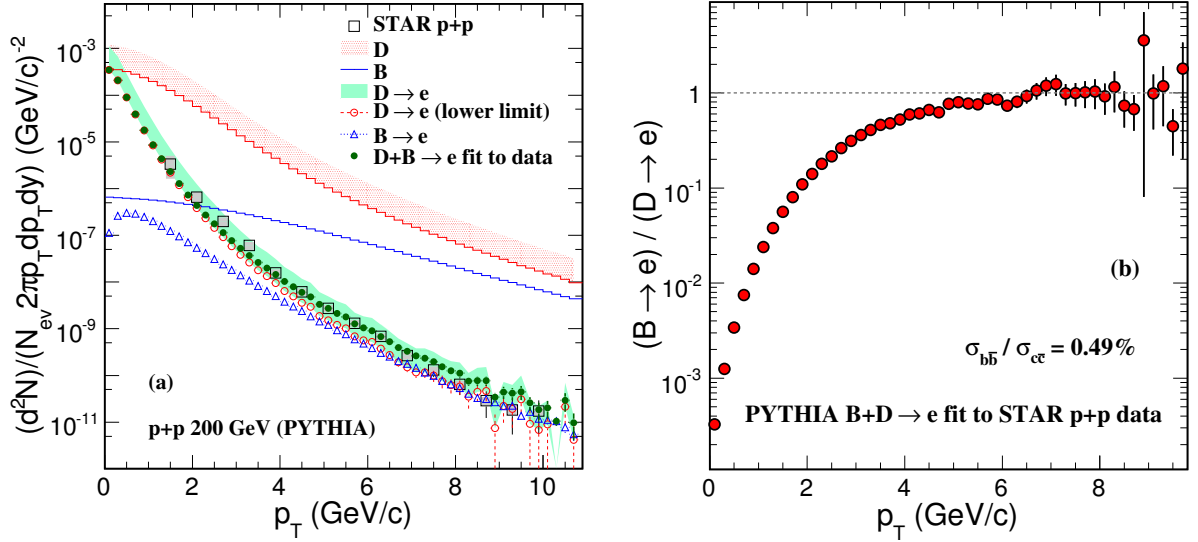
Figure 5.10: Panel (a): D-/B- mesons and their decay electron spectra from PYTHIA. The $B + D \rightarrow e$ fit to STAR non-photonic electron data in $p+p$ collisions. Panel (b): The relative spectra ratio, upper limit of $B \rightarrow e$ contributions as a function of p_T.

ratio as $\sigma_{b\bar{b}}/\sigma_{c\bar{c}} \leq (0.49 \pm 0.09 \pm 0.09)\%$. The first term of the errors is calculated from $\chi^2 = \chi^2_{min} + 1$. The second term is from the 15% normalization error of the dN/dy converted to total cross sections due to the uncertainties of the model dependent rapidity distributions [Xin05]. Fig. 5.11 (b) shows the B-/D- mesons rapidity distributions from PYTHIA. The cross section ratio from FONLL calculation is 0.18%-2.6% [CNV05]. The upper limit is consistent with theory prediction.

The upper limit of $B \rightarrow e$ contributions as a function of p_T is shown in Fig. 5.10 (b). It is increasing and becomes flat around 7 GeV/c. The p_T crossing point, where the bottom contribution is equal to charm, of electron spectra from B,D decay is very sensitive to the cross section ratio, since at high p_T, these electron spectra shapes are similar. From the $B + D \rightarrow e$ fit to STAR $p+p$ data, we estimate the crossing point $p_T^c \geq 7$ GeV/c.

Table 5.2 lists the crossing points of heavy flavor decay electrons in several p_T bins.

Table 5.2: Crossing points of heavy flavor decay electrons as a function of p_T.

p_T (GeV/c)	2	3	4	5	6	7 (p_T^c)	8
$(B \rightarrow e)/(D \rightarrow e) \leq$	0.11	0.31	0.53	0.77	0.85	1.2	1.1
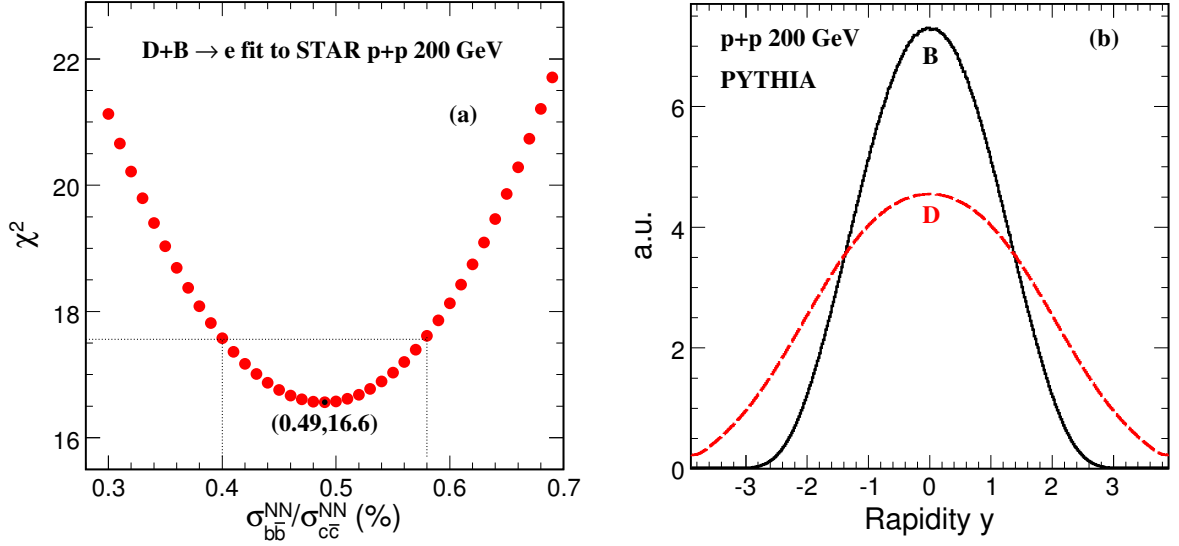
Figure 5.11: Panel (a): Fit χ^2 as a function of $\sigma_{b\bar{b}}/\sigma_{c\bar{c}}$. Straight lines is for the $\chi^2 = \chi^2_{min} + 1$. Panel (b): B- (solid curve) /D- (dashed curve) mesons rapidity distributions from PYTHIA.

5.4.2 Fit to non-photonic electron v_2

Besides the non-photonic electron spectrum, the non-photonic electron v_2 has also been measured in 200 GeV Au+Au collisions at RHIC [?]. In this measurement, bottom contribution has not been separated, which can be studied by comparing simulations and data. Since heavy flavor hadrons p_T distributions and v_2 are unknown, our simulations have to base on the following assumptions:

- The same relative $(B \to e)/(D \to e)$ ratio from $p+p$ to Au+Au.

- Assume the B-/D- meson v_2 as the inputs for the simulation, here we assume three aspects:

  - I: B-/D- meson v_2 are similar as light meson v_2.

  - II: D-meson v_2 as light meson v_2 but B-meson does not flow.

  - III: $B \to e$ contribution is neglected and D-meson v_2 decreases at $p_T > 2$ GeV/c.

90

Here heavy flavor baryons, Λ_c, Λ_b are taken into account as 10% of total heavy flavor hadrons [PDG04, **?**]. Their v_2 are assumed to follow light baryon v_2. This baryon contribution effect in this simulation is small.

We use the light meson v_2 curve from fitting experimental data [DES04] as the input B/D v_2 distributions (Assumption I), see Fig. 5.12 (a). That means in each p_T bin, the B/D $\Delta\phi$ distribution is initialized. The electron $\Delta\phi$ distributions in each p_T bin will be obtained via B/D decays in PYTHIA model. Then the electron v_2, shown in Fig. 5.12 (b), will be extracted by fitting the $\Delta\phi$ distributions in each p_T bin.
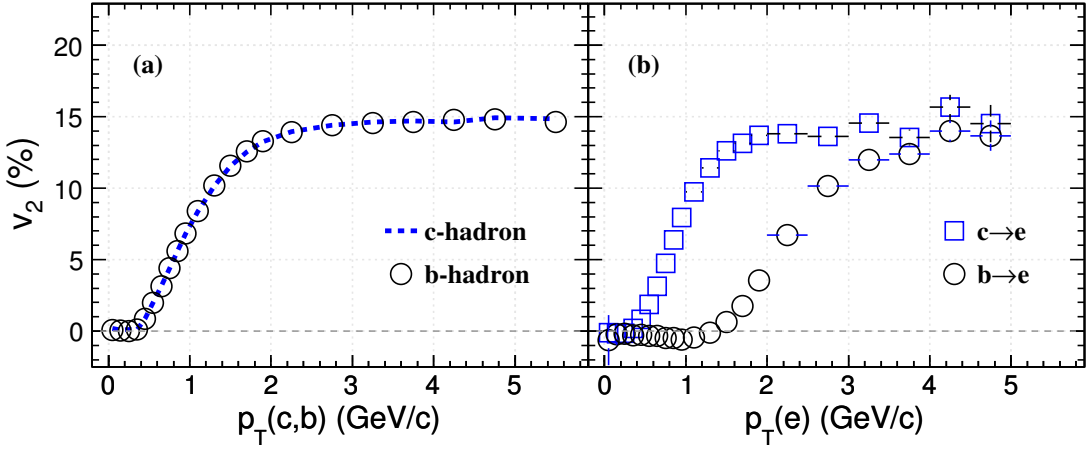
Figure 5.12: Panel (a): Assumed B-meson v_2 (open circles) and D-meson v_2 (dashed curve) as light meson v^2. Panel (b): Electron v_2 from B-meson decays (open circles) and D-meson decays (open squares).

Fig. 5.12 shows the obvious mass effect: The B/D v_2 are assumed as the same, but the decay electron v_2 can be very different due to decay kinematics [YFHP06]. This is not surprising, since we know B-meson is much heavier than D-meson and light hadrons. The decay electrons can only have a small momentum fraction of B-mesons. The momentum and angular correlations between decay electrons and B-mesons are weak, especially at low p_T. Therefore, at low p_T the decay electron ϕ angle will almost randomly distribute. So we see the zero or negative v_2 for the electron from B-meson decays. But from previous study, we know that bottom contribution below 3 GeV/c is small, thus the mass effect to the total electron v_2 is not significant.

Fig. 5.13 (a) shows the total electron v_2 from PYTHIA simulation compared to data. The measured non-photonic electron v_2 from PHENIX is shown as the triangles. The solid curve (Assumption I) is the sum v_2 of the two decay electron v_2 distributions in Fig. 5.12 (b) by taking the relative ratio of $(B \to e)/(D \to e)$ into account. It can not describe the data. If we assume B-meson does not flow (Assumption II), the total decay electron v_2 will become decreasing, shown as the band. The band is corresponding to the $\sigma_{b\bar{b}}/\sigma_{c\bar{c}} = (0.3 - 0.7)\%$ (The upper limit, 0.49%, is in between). It has better agreement with data, but still higher. The decreasing of non-photonic electron v_2 could be due to $B \to e$ contribution and B-meson v_2 could be very small. But below 3 GeV/c, $B \to e$ contribution is not significant. That indicates D-meson v_2 should be smaller than light meson v_2 and start decreasing at higher p_T (> 2 GeV/c).
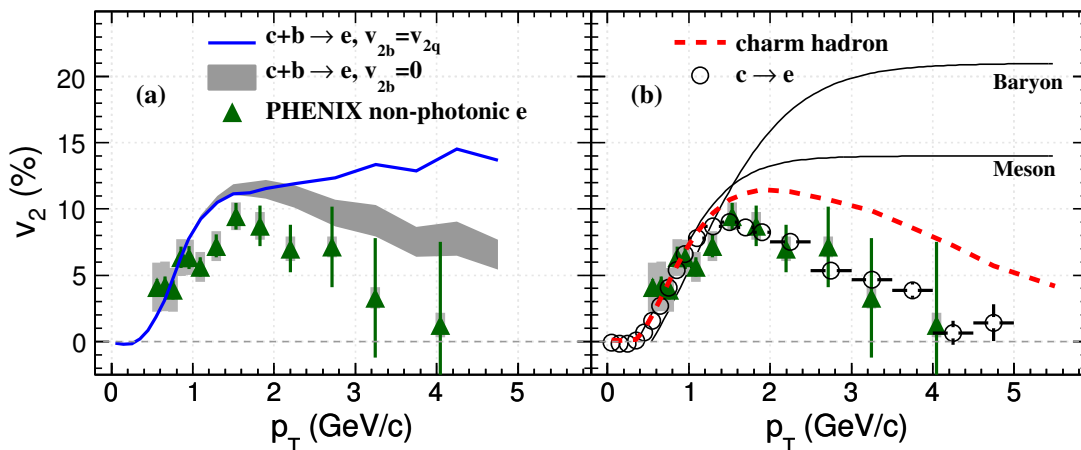
Figure 5.13: Panel (a): The total electron v_2 from PYTHIA simulation assuming that bottom flows (solid curve) and bottom does not flow (band) compared to data. Panel (b): The total electron v_2 from PYTHIA simulation fit to data and the estimated D-meson v_2.

So ignoring $B \to e$ contribution, we try to speculate the D-meson v_2 by fitting the data using decay electron v_2 (Assumption III). In Fig. 5.13 (b), the best fit of the decay electron v_2 is shown as the open circles. The estimated D-meson v_2 is shown as the dashed curve, which is smaller than light meson v_2 above 1 GeV/c and start decreasing above 2 GeV/c. This most possible D-meson v_2 distribution shows that at $p_T < 3$ GeV/c, where the bottom contribution is negligible, D-meson has large v_2, indicating that charm strongly

flows in high dense medium, which could be the evidence of light flavor thermalization in QGP created at RHIC energy.

CHAPTER 6

Detector upgrades and outlook

6.1 STAR detector upgrades: TOF and HFT

The experimental physics results are inevitably limited by the detector resolutions, luminosities, acceptances and electronics *etc*. Physics developments require the upgrade of the detectors and electronics. The STAR Collaboration has proposed some important sub-detector upgrades. The full barrel Time-Of-Flight (TOF) detector [STA04] and the Heavy Flavor Tracker (HFT) [STA05] are two of them. The other detector upgrades like the Intermediate Silicon Tracker (IST) and the Forward GEM Tracker (FGT) *etc*, will not be introduced in this thesis.

The barrel TOF detector based on recently developed Multi-gap Resistive Plate Chamber (MRPC) technology will surround the outer edge of the TPC, covering $-1 < \eta < 1$ and $\sim 2\pi$ in azimuth. The TOF system can achieve the required timing resolution < 100 ps and the particle detecting efficiency $> 95\%$. This detector will significantly extend the reach of the STAR scientific program, doubling the percentage of kaons and protons for which particle identification is possible to more than 95% of all those produced within the MRPC-TOF acceptance. Combined with existing STAR detectors, the barrel TOF detector will allow STAR to extract the maximum amount of information and statistics for heavy flavor, dilepton and resonances physics, such as the single electron, muon p_T spectra, the single electron v_2, J/Ψ, ρ, ω, vector mesons, *etc*.

When combined with a possible future vertex detector upgrade, the proposed TOF detector will also reduce the integrated luminosity needed to measure a statistically robust sample of D^0, D^+, D_s^+ mesons by approximately an order of magnitude, enabling STAR

to make systematic studies of charm thermalization and D^0 meson flow.

In addition, with the barrel TOF detector, it becomes possible to separate the bottom contribution in non-photonic electron measurement experimentally and charm physics will be more clearly understood.

The expectant vertex detector HFT brings extremely high precision tracking capabilities to STAR with a resolution of 10 μm at the first layer of the detector, over a large pseudo-rapidity range, and with complete azimuthal angular coverage $\Phi = 2\pi$. The two layers of the Heavy Flavor Tracker (HFT), which are composed of monolithic CMOS pixel detectors using 30 $\mu m \times 30 \mu m$ square pixels, will be placed closed to beam pipe in STAR at radii of 2.5 cm and 7 cm, respectively.

The HFT is designed to measure displaced vertices that are displaced 100 micros, or less, from the primary vertex. Therefore, the neutral and charged particles with very short lifetimes can be distinguished from the primary particles which originate at the collision vertex. The addition of the HFT will extend STAR's unique capabilities even further by providing particle identification for hadrons containing charm and beauty and electrons decaying from charm and beauty hadrons. Thus, the HFT is the enabling technology for making direct charm and beauty measurements at STAR.

6.2   Direct measurements of charmed hadrons with HFT

The Monte Carlo events in Au+Au collisions at $\sqrt{s_{\mathrm{NN}}} = 200$ GeV are generated by using HIJING model. The standard GSTAR simulation package with modifications of the new detector design is used for the material geometry configurations. The new STAR tracking software package ITTF with HFT layers added is used for tracking.

The physical interactiona between particles and the material of the detector are simulated using the STAR implementation of the GEANT simulation package. This package is used in STAR and is a standard analysis tool which includes a detailed understanding of the TPC response function; including dead areas and realistic detector resolutions and

responses. Realistic detector resolutions are used to smear the perfect position information, and the resulting simulated hits are used in tracking. For the SSD, the hits were smeared by 20 μm in and 750 μm in z, in agreement with the SSD specifications. For the HFT, the hits were smeared by 6 μm in both Φ and z.

In this section, we will focus on the charmed hadron reconstruction. The optimization of the HFT hit finding accuracy, vertex reconstruction performance, single track efficiency and ghost rate *etc*, will not be discussed. The details can be found in Ref. [STA05].

To demonstrate the power of the HFT, we have simulated several specific charm hadron decay channels, including $D^0 \rightarrow K^-\pi^+$ and $D^+ \rightarrow K^-\pi^+\pi^+$. Table 6.1 displays some of the properties of these channels.

Table **6.1**: Open charm hadron properties.

Particle	Daughters	c_τ (μm)	Mass (GeV)
D^0	$K^-\pi^+$ (3.8%)	122.9	1.8645
D^+	$K^-\pi^+\pi^+$ (9.5%)	311.8	1.8693
D_s^+	$\Phi\pi^+$ (4.4%) $\pi^+\pi^+\pi^-$ (1.2%)	149.9	1.9682
Λ_c	$pK^-\pi^+$ (5.0%)	59.9	2.2865

Signal and background events are generated separately. The signal consists of one D^0 or D^+ per event. The transverse momentum distribution of the charmed hadrons follows a Boltzman distribution which reproduces the $\langle p_T \rangle$ of D-mesons as measured by STAR in d+Au collisions at $\sqrt{s_{\text{NN}}} = 200$ GeV [STAc05] and the rapidity distribution suggested by perturbative QCD calculations applying the program code Pythia [Sj01]. The background is simulated using the MevSim event generator parameterized to reproduce the experimentally measured particle multiplicities in Au+Au collisions at $\sqrt{s_{\text{NN}}} = 200$ GeV. Our parameterization is accurate for particles below 3 GeV/c. It may underestimate the background above this momentum. The distributions of reconstructed D-meson signal and background were scaled to match the expected D-meson production per central Au+Au collision. Also, the higher track reconstruction efficiency in single (signal) events compared to central Au+Au collisions (background) was taken into account.

The heavy flavor tracker is designed to allow us to directly reconstruct mesons containing charm quarks. If this is true, we should see differences between the charm meson daughter tracks and the background and the primary tracks in several important variables. The DCA between the tracks and the vertex is an important example of this; see Fig. 6.1. The distributions of reconstructed D^0 and $^+$ daughters is compared to the primary track background. The charm meson tracks clearly have a broader distribution, driven by the decay length of the charm mesons. Cutting on the track DCA, then, will improve the signal to noise in the analyses.
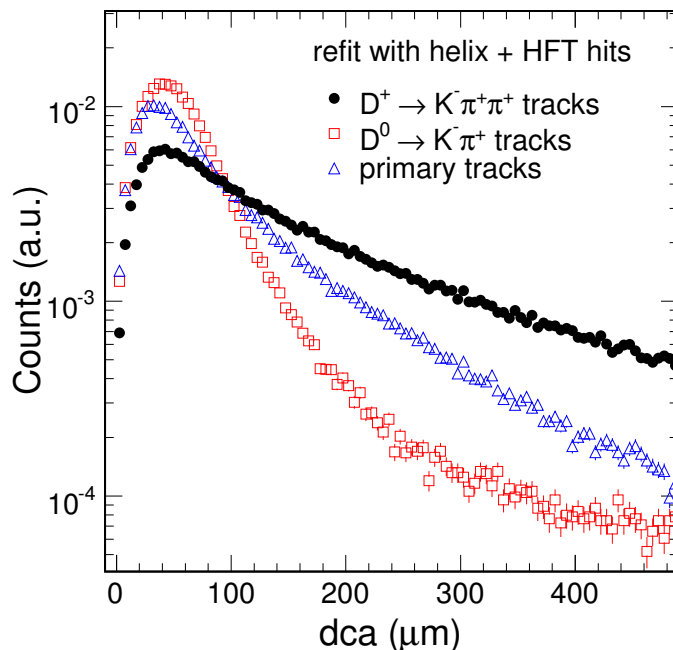
Figure 6.1: The DCA distributions for D^0 (triangles) and D^+ (circles) reconstructed by HFT. The results of the dca distribution for primary tracks are shown in squares for comparison.

The following selection criteria were also used to separate the D-meson signal from background.

- The decay length l: the distance between the primary vertex and the D-meson decay vertex (V0).

- The DCA between the daughter tracks and the reconstructed decay vertex.

- Momentum angle correlation $\cos(\theta)$: θ is defined as the angle between the D-meson momentum (vector sum of the two daughter momenta) and the vector joining the primary vertex to the D-meson decay vertex.

The topological reconstruction of $D^+ \to K^-\pi_1^+\pi_2^+$ is introduced here as an example. The better signal to background can be obtained for the reconstruction of $D^0 \to K^-\pi^+$, since it is two-body decay. The HFT is designed as close to collision vertex as possible, so that it gives good primary vertex performance ($\sim 10\mu m$), which is good enough for the secondary vertex reconstruction. And the reconstructed TPC helixes are required to hit on the two layers of HFT. After refit the helixes with two HFT hits, the new helixes were obtained. The new helixes were used to calculate those variables mentioned above. Since it is three-body decay, D^+ decay vertex is estimated by calculating the average of three displaced points of $K^-\pi_1^+$, $K^-\pi_2^+$ and $\pi_1^+\pi_2^+$.

The reconstruction of charmed baryon Λ_c is similar as D^+. But due to the smaller c_τ and different charm fragmentation ratios, the cuts for Λ_c, D^0 and D^+ should be different. The cuts are optimized to obtain good signal to background ratio. Table 6.2 lists the cuts for the charmed hadrons.

Table 6.2: Topological cuts for open charm hadrons.

Cuts	D^0	D^+	Λ_c
nFitPts $>$	15	15	15
$|\eta| <$	1.0	1.0	1.0
DCA (global) $\geq$		100 μm	35 μm
DCA (V0) $\leq$	35 μm	100 μm	40 μm
decay length $\geq$	150 μm	150 μm	50 μm
$\cos(\theta) >$	0.996	0.85	0.92

The dca, $\cos(\theta)$, and decay-length distributions for both primary tracks (open-squares) and D^+ decayed tracks are shown in Fig. 6.2. Clearly the decayed tracks are well separated from the primary track. For D^+ reconstruction, a slightly different method was used compared to that of the D^0. The 'signal event' and 'background event' were mixed together. The distribution of the invariant mass from a K and two π tracks is then
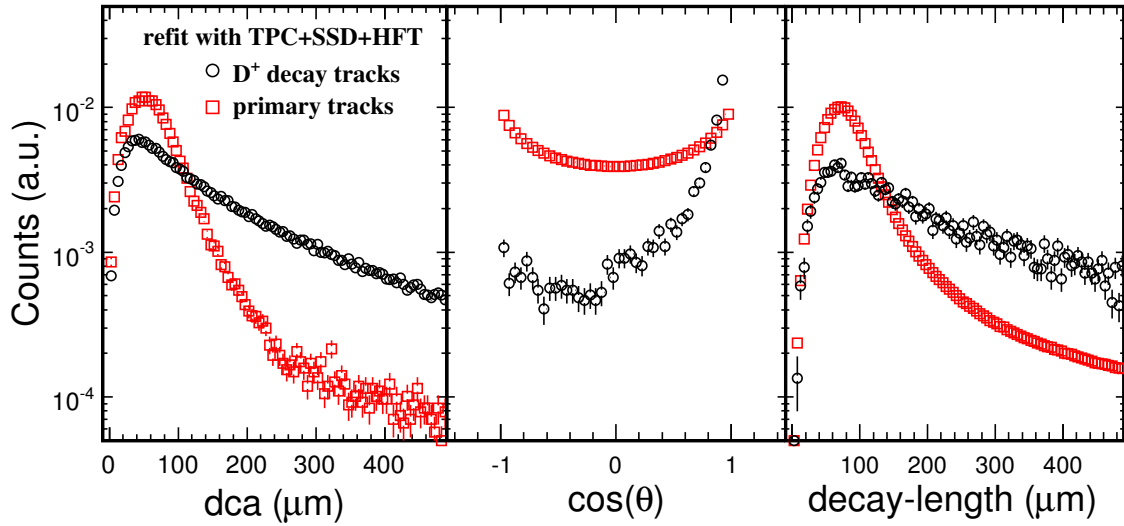
Figure 6.2: The D^+ daughter tracks decay-length, dca, and $\cos(\theta)$ distributions (circles). The same distributions for primary tracks are shown as squares.

formed. The number of tracks used in the background events is consistent with the top 10% central Au+Au collisions at RHIC. The resulting invariant mass distributions for several p_T bins are shown in Fig. 6.3. For the p_T bins studied so far, the significance $S/\sqrt{S+B}$ is better than 3.

6.3 Bottom separation in heavy flavor measurements

With the barrel TOF detector and vertex detector HFT, the D-meson p_T spectrum and non-photonic electron p_T spectrum will be measured precisely. The D-meson semileptonic decayed electron spectrum will be known based on models via decay kinematics. Comparison between the D-meson decayed electron and non-photonic electron p_T distributions will tell us the information of the bottom contribution in non-photonic electron measurements. This will also be tested from the measurements of D-meson v_2 and non-photonic electron v_2 when the TOF detector and HFT are available.

But before the barrel TOF detector and HFT installation in STAR, the separation of B-meson and D-meson due to their different life time (decay length) is proposed to be a
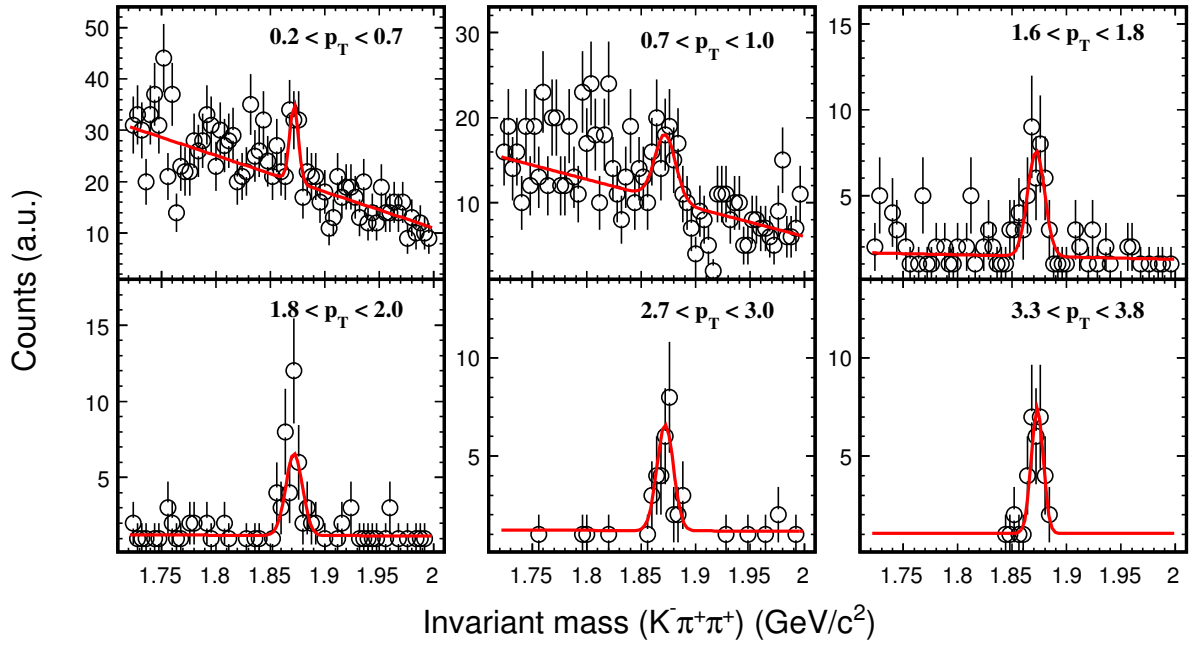
Figure 6.3: Invariant mass distributions for D^+ for several p_T windows. The lines are a polynomial (up to 2nd order) + Gaussian fit.

good try. Fig. 6.4 shows the different decay length distributions of D-meson and B-meson.

D-meson decay vertex will be closer to the collision vertex than B-meson. Currently, the existing vertex detector SVT and intermediate detector SSD will be used to help the reconstruction of the B-meson decay vertex.
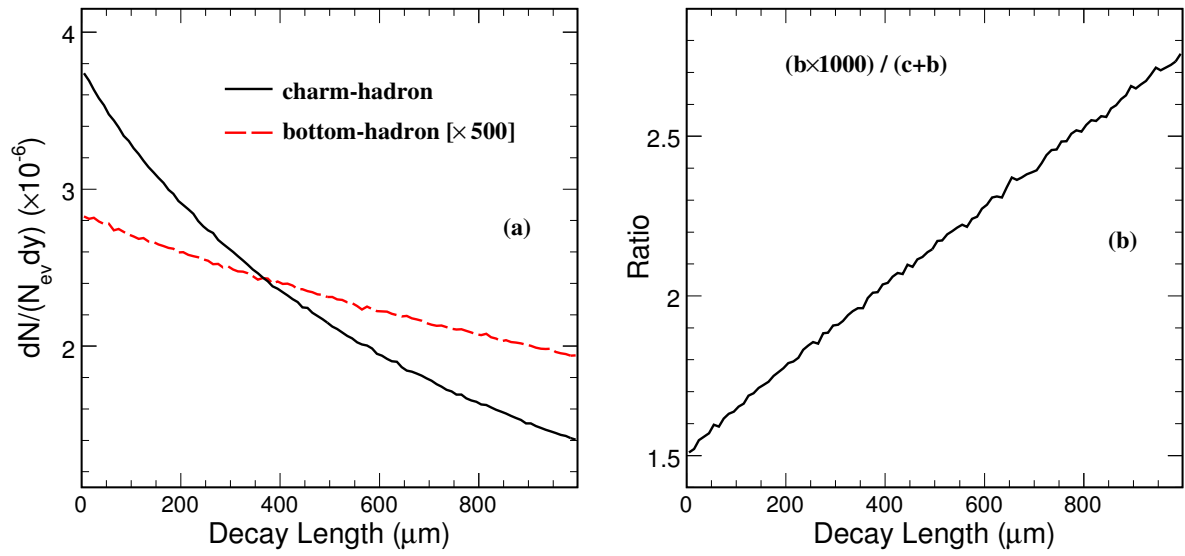
Figure 6.4: Panel (a): D-/B- mesons decay length distributions. Panel (b): The fraction of B-meson in the total decay length of (B+D)-meson.

APPENDIX A

Presentations and publication list

<u>Presentations</u>

- *Electron Spectra in Au+Au Collisions at 200 GeV* (poster)
  2005 Gordon Research Conference on Nuclear Chemistry, Bates College, Lewiston, ME, USA, 07/10/2005 - 07/15/2005.

- *Charm Hadron Reconstructions with HFT*
  STAR Upgrades Workshop, Brookhaven, New York, USA, 12/01/2005 - 12/07/2005.

- *Scaling of Charm Integrated Cross Section and Modification of its p_T Spectra in 200 GeV Au+Au Collisions at STAR*
  2006 International Conference of Strangeness in Quark Matter, UCLA, California, USA, 03/25/2006 - 04/01/2006.

- *Charm Cross Sections and Collectivity from its Semileptonic Decay at RHIC*
  2nd International Conference on Hard and Electromagnetic Probes of High-Energy Nuclear Collisions, Asilomar, California, USA, 06/09/2006 - 06/16/2006.

- *Identify Bottom Contribution in Non-photonic Electron Spectra and v_2 from p+p and Au+Au Collisions at RHIC*
  23rd Winter Workshop on nuclear Dynamics, Big Sky, Montana, USA, 02/11/2007 - 02/18/2007.

Publication List

- Y. F. Zhang (for STAR collaboration), "Open charm production in $\sqrt{(s_{NN})} = 200$ GeV Au+Au collisions.", *J. Phys. G: Nucl. Part. Phys.*, **32**, S529-S532, 2006.

- Z. Xu *et al.*, "Measurement of charm flow with the STAR Heavy Flavor Tracker.", *J. Phys. G: Nucl. Part. Phys.*, **32**, S571-S574, 2006.

- Y. F. Zhang, S.Esumi, H.Huang, Y.Miake, S.Sakai and N.Xu, "Identifying bottom contribution in non-photonic electron spectra and v_2 from Au+Au collisions at RHIC.", *Nucl. Phys. A*, **783**, 489-492, 2007.

- H. D. Liu, Y. F. Zhang, C. Zhong and Z. Xu, "Extracting the charm cross-section from its semileptonic decay at RHIC." , *Phys. Lett. B*, **639**, 441, 2006.

- Y. F. Zhang, S. L. Huang, Z. P. Zhang, J. Wu, "Study on "soft" and "hard" interactions in $pp(\bar{p}p)$ collisions using HIJING and PYTHIA.", *Chinese Physics*, **16**, 58-61, 2007.

- Y. F. Zhang, S. L. Huang, Z. P. Zhang, J. Wu, "Simulation on "soft" and "hard" process in $pp(\bar{p}p)$ collisions using HIJING and PYTHIA.", *Journal of University of Science and Technology of China*, **35(6)**, 821-824, 2005 (in Chinese).

- Q. Shan, J. Wu, X. L. Wang, H. F. Chen, Y. F. Zhang, Z. P. Zhang, M. Shao, "Upper limit of the yield of di-omega in central Au+Au collision at $\sqrt{(s_{NN})} = 200$ GeV with HIJING.", *High Energy Phys. and Nucl. Phys.*, **29**, 1146-1149, 2005.

- J. Adams *et al.*, STAR Collaboration. "Pion, Kaon, Proton and Anti-proton Transverse Momentum Distributions from p + p and d + Au Collisions at $\sqrt{s_{NN}}= 200$ GeV.", *Phys. Lett. B*, **616** 8, 2005.

- J. Adams *et al.*, STAR Collaboration. "Hadronization Geometry and Charge-dependent Number Autocorrelations on Axial Momentum Space in Au+Au Collisions at $\sqrt{s_{NN}}= 130$ GeV. ", *Phys. Lett. B*, **634** 347, 2006.

- J. Adams *et al.*, STAR Collaboration. "Azimuthal Anisotropy in Au+Au Collisions at $\sqrt{s_{\mathrm{NN}}}$= 200 GeV. ", *Phys. Rev. C*, **72** 014904, 2005.

- J. Adams *et al.*, STAR Collaboration. "Minijet Deformation and Charge-independent Angular Correlations on Momentum Subspace (η, ϕ) in Au+Au Collisions at $\sqrt{s_{\mathrm{NN}}}$= 130 GeV. ", *Phys. Rev. C*, **73** 064907, 2006.

- J. Adams *et al.*, STAR Collaboration. "Experimental and Theoretical Challenges in the Search for the Quark Gluon Plasma: The STAR Collaboration's Critical Assessment of the Evidence from RHIC Collisions. ", *Nucl. Phys. A*, **757** 102, 2005.

- J. Adams *et al.*, STAR Collaboration. "Multiplicity and Pseudorapidity Distributions of Photons in Au+Au Collisions at $\sqrt{s_{\mathrm{NN}}}$= 62.4 GeV. ", *Phys. Rev. Lett*, **95** 062301, 2005.

- J. Adams *et al.*, STAR Collaboration. "Multi-strange Baryon Elliptic Flow in Au+Au collisions at $\sqrt{s_{\mathrm{NN}}}$= 200 GeV. ", *Phys. Rev. Lett.*, **95** 122301, 2005.

- J. Adams *et al.*, STAR Collaboration. "Incident Energy Dependence of p_T Correlations at RHIC. ", *Phys. Rev. C*, **72** 044902, 2005.

- J. Adams *et al.*, STAR Collaboration. "Transverse-momentum p_T Correlations on (η, ϕ) from mean p_T Fluctuations in Au+Au Collisions at $\sqrt{s_{\mathrm{NN}}}$= 200 GeV. ", *J. Phys. G*, **32** L37, 2006.

- J. Adams *et al.*, STAR Collaboration. "Directed Flow in Au+Au Collisions at $\sqrt{s_{\mathrm{NN}}}$= 62 GeV. ", *Phys. Rev. C*, **73** 034903, 2006.

- J. Adams *et al.*, STAR Collaboration. "Proton-Lambda Correlations in Central Au+Au Collisions at $\sqrt{s_{\mathrm{NN}}}$= 200 GeV. ", *Phys. Rev. C*, **74** 064906, 2006.

- J. Adams *et al.*, STAR Collaboration. "Multiplicity and Pseudorapidity Distributions of Charged Particles and Photons at Forward Pseudorapidity in Au+Au Collisions at $\sqrt{s_{\mathrm{NN}}}$= 62.4 GeV. ", *Phys. Rev. C*, **73** 034906, 2006.

- J. Adams *et al.*, STAR Collaboration. "Strangelet Search at RHIC. ", *arXiv: nucl-ex/0511047* .

- M. Calderon de la Barca Sanchez *et al.*, STAR Collaboration. "Open Charm Production from d + Au Collisions in STAR. ", *Eur. Phys. J. C*, **43** 187, 2005.

- A. A. P. Suaide *et al.*, STAR Collaboration. "Charm Production in the STAR Experiment at RHIC. ", *Eur. Phys. J. C*, **43** 193, 2005.

- C. A. Gagliardi *et al.*, STAR Collaboration. "Recent high-p_T Results from STAR. ", *Eur. Phys. J. C*, **43** 263, 2005.

- J. Adams *et al.*, STAR Collaboration. "Identified Hadron Spectra at Large Transverse Momentum in p + p and d + Au Collisions at $\sqrt{s_{\mathrm{NN}}}$ = 200 GeV. ", *Phys. Lett. B*, **637** 161, 2006.

- J. Adams *et al.*, STAR Collaboration. "Measurements of Identified Particles at Intermediate Transverse Momentum in the STAR Experiment from Au+Au Collisions at $\sqrt{s_{\mathrm{NN}}}$=200 GeV. ", *arXiv: nucl-ex/0601042* .

- J. Adams *et al.*, STAR Collaboration. "Forward Neutral Pion Production in p + p and d + Au Collisions at $\sqrt{s_{\mathrm{NN}}}$ = 200 GeV. ", *Phys. Rev. Lett.*, **97** 152302, 2006.

- J. Adams *et al.*, STAR Collaboration. "Direct Observation of Dijets in Central Au+Au Collisions at $\sqrt{s_{\mathrm{NN}}}$ = 200 GeV. ", *Phys. Rev. Lett.*, **97** 162301, 2006.

- J. Adams *et al.*, STAR Collaboration. "Strange Baryon Resonance Production in $\sqrt{s_{\mathrm{NN}}}$ = 200 GeV p + p and Au+Au Collisions. ", *Phys. Rev. Lett*, **97** 132301, 2006.

- J. Adams *et al.*, STAR Collaboration. "The Energy Dependence of p_T Angular Correlations Inferred from mean p_T Fluctuation Scale Dependence in Heavy Ion Collisions at the SPS and RHIC. ", *J. Phys. G*, **33** 451, 2007.

- J. Adams *et al.*, STAR Collaboration. "Identified Baryon and Meson Distributions at Large Transverse Momenta from Au+Au Collisions at $\sqrt{s_{\mathrm{NN}}}$ = 200 GeV. ", *Phys. Rev. Lett*, **97** 152301, 2006.

- J. Adams *et al.*, STAR Collaboration. "Scaling Properties of Hyperon Production in Au+Au Collisions at $\sqrt{s_{\mathrm{NN}}}$= 200 GeV. ", *arXiv: nucl-ex/0606014.*

- J. Adams *et al.*, STAR Collaboration. "The Multiplicity Dependence of Inclusive p_T Spectra from $p + p$ Collisions at $\sqrt{s_{\mathrm{NN}}}$= 200 GeV. ", *Phys. Rev. D*, **74** 032006, 2006.

- J. Adams *et al.*, STAR Collaboration. "Delta phi Delta eta Correlations in Central Au+Au Collisions at $\sqrt{s_{\mathrm{NN}}}$= 200 GeV. ", *Phys. Rev. C*, **75** 034901, 2007.

- B. I. Abelev *et al.*, STAR Collaboration. "Transverse Momentum and Centrality Dependence of high-p_T Non-photonic Electron Suppression in Au+Au Collisions at $\sqrt{s_{\mathrm{NN}}}$= 200 GeV. ", *arXiv: nucl-ex/0607012.*

- B. I. Abelev *et al.*, STAR Collaboration. "Strange Particle Production in $p + p$ Collisions at $\sqrt{s_{\mathrm{NN}}}$= 200 GeV. ", *arXiv: nucl-ex/0607033.*

- B. I. Abelev *et al.*, STAR Collaboration. "Neutral Kaon Interferometry in Au+Au Collisions at $\sqrt{s_{\mathrm{NN}}}$= 200 GeV. ", *Phys. Rev. C*, **74** 054902, 2006.

- B. I. Abelev *et al.*, STAR Collaboration. "Longitudinal Double-spin Asymmetry and Cross Section for Inclusive Jet Production in Polarized Proton Collisions at $\sqrt{s_{\mathrm{NN}}}$= 200 GeV. ", *Phys. Rev. Lett*, **97** 252001, 2006.

- B. I. Abelev *et al.*, STAR Collaboration. "Rapidity and Species Dependence of Particle Production at Large Transverse Momentum for $d + $ Au Collisions at $\sqrt{s_{\mathrm{NN}}}$= 200 GeV. ", *arXiv: nucl-ex/0609021.*

- B. I. Abelev *et al.*, STAR Collaboration. "Partonic Flow and Phi-meson Production in Au $+$ Au Collisions at $\sqrt{s_{\mathrm{NN}}}$= 200 GeV. ", *arXiv: nucl-ex/0703033.*

- B. I. Abelev *et al.*, STAR Collaboration. "Charged Particle Distributions and Nuclear Modification at High Rapidities in $d + $ Au Collisions at $\sqrt{s_{\mathrm{NN}}}$= 200 GeV. ", *arXiv: nucl-ex/0703033.*

- B. I. Abelev *et al.*, STAR Collaboration. "Mass, Quark-number, and $\sqrt{s_{\mathrm{NN}}}$ Dependence of the Second and Fourth Flow Harmonics in Ultra-Relativistic Nucleus-Nucleus Collisions. ", *arXiv: nucl-ex/0701010.*

References

[Abr01] M.C. Abreu et al. *Phys. Lett. B*, **521**:195, 2001.

[ABR03] A. Andronic, P. Braun-Munzinger, K. Redlich, and J. Stachel. *Phys. Lett. B*, **571**:36, 2003.

[Acc04] A. Accardi and M. Gyulassy. *J. Phys. G*, **30**:S969, 2004; *Phys. Lett. B*, **586**:244, 2004.

[Aco03] D. Acosta et al. *Phys. Rev. Lett.*, **91**:241804, 2003.

[Ada03a] D. Adamova et al. *Phys. Rev. Lett.*, **91**:042301, 2003.

[Ada03b] J. Adams et al. *Phys. Rev. Lett.*, **91**:072304, 2003.

[Ada03c] J. Adams et al. *arXiv: nucl-ex/0309012*, 2003.

[Ada03d] J. Adams et al. *Phys. Rev. Lett.*, **91**:172302, 2003.

[Ada04a] J. Adams et al. *Phys. Rev. Lett.*, **92**:112301, 2004.

[Ada04b] J. Adams et al. *Phys. Rev. Lett.*, **92**:052302, 2004.

[Ada04c] J. Adams et al. *arXiv: nucl-ex/0406003*, 2004.

[Ada04d] J. Adams et al. *Phys. Rev. C*, **70**:044902, 2004.

[Ada04e] J. Adams et al. *Phys. Rev. Lett.*, **93**:252301, 2004.

[Ada04f] J. Adams et al. *Phys. Rev. Lett.*, **93**:252301, 2004.

[Ada04g] J. Adams et al. *Phys. Rev. Lett.*, **92**:171801, 2004.

[Ada05] J. Adams et al. "STAR white paper." *arXiv: nucl-ex/0501009*, 2005.

[Adc02] K. Adcox et al. *Phys. Rev. Lett.*, **88**:192303, 2002.

[Adc04] K. Adcox et al. "PHENIX white paper." *arXiv: nucl-ex/0410003*, 2004.

[Adl02a] C. Adler et al. *Phys. Rev. Lett.*, **89**:202301, 2002.

[Adl02b] C. Adler et al. *Phys. Rev. C*, **66**, 2002.

[Adl03a] S.S. Adler et al. *Phys. Rev. Lett.*, **91**:182301, 2003.

[Adl03b] S.S. Adler et al. *Phys. Rev. Lett.*, **91**:241803, 2003.

[Adl04a] S.S. Adler et al. *arXiv: nucl-ex/0409015*, 2004.

[Adl04b] S.S. Adler et al. *Phys. Rev. Lett.*, **92**:051802, 2004.

[Adl04c] S.S. Adler et al. *Phys. Rev. C*, **69**:014901, 2004.

[Adl05]   S.S. Adler et al. *Phys. Rev. Lett.*, **94**:082301, 2005.

[Afa02]   S.V. Afanasiev et al. *Phys. Rev. C*, **66**:054902, 2002.

[Ala01]   J. Alam et al. *Phys. Rev. C*, **63**:021901, 2001.

[Alp02]   S. Bethke. *Nucl. Phys. Proc. Suppl.*, **121**:74-81, 2003.

[Alt03]   C. Alt et al. *Phys. Rev. C*, **68**:034903, 2003.

[Alv96]   G.A. Alves et al. *Phys. Rev. Lett.*, **77**:2388, 1996.

[Amm88] R. Ammar et al. *Phys. Rev. Lett.*, **61**:2185, 1988.

[And03]   M. Anderson et al. *Nucl. Instr. Meth. A*, **499**:659, 2003.

[Arm05]   N. Armesto et al. *Phys. Rev. D*, **71**:054027, 2005.

[Arm06]   N. Armesto et al. *Phys. Lett. B*, **637**:362, 2006.

[B76]   F.W. Büsser et al. *Nucl. Phys. B*, **113**:189, 1976.

[Bar88]   S. Barlag et al. *Z. Phys. C*, **39**:451, 1988.

[BCH03]   E.L. Bratkovskaya, W. Cassing, and Stöcker H. *Phys. Rev. C*, **67**:054905, 2003.

[BCS04]   E.L. Bratkovskaya, W. Cassing, H. Stöcker, and N. Xu. *arXiv: nucl-th/0409047*, 2004.

[Bea04]   I.G. Bearden et al. *Phys. Rev. Lett.*, **93**:102301, 2004.

[Bic06]   H. Bichsel. *Nucl. Instr. Meth. A*, **562**:154, 2006.

[Bjo83]   J.D. Bjorken. *Phys. Rev. D*, **27**:140, 1983.

[BKG03]   S. Batsouli, S. Kelly, M. Gyulassy, and J.L. Nagle. *Phys. Lett. B*, **557**:26, 2003.

[Bot90]   O. Botner et al. *Phys. Lett. B*, 1990.

[BPLF04] G. G. Barnaföldi, G. Papp, P. Lévai and G. Fai. *J. Phys. G*, **30**:S1125, 2004.

[Bra01]   P. Braun-Munzinger. *Nucl. Phys. A*, **681**:119c, 2001.

[Bus04]   P.J. Bussey et al. *arXiv: hep-ex/0408020*, 2004.

[Cat04]   E. Cattaruzza and D. Treleani. *Phys. Rev. D*, **69**:094006, 2004.

[Css89]   J.C. Collins, D.E. Soper and G. Sterman, in *Perturbative QCD*, edited by A.H. Mueller (World Scientific, Singapore, 1989), p.1.

[Col98]   J.C. Collins. *Phys. Rev. D*, **66**:094002, 1998.

[Cas04]   J. Castilllo et al. *J. Phys. G*, **30**:S1207, 2004.

[CER]   CERN. "http://wwwasd.web.cern.ch/wwwasd/cernlib/.".

[CLEO04] CLEO Collaboration, J. Yelton et al. Presented at Heavy Quarks and Leptons, San Juan, Puerto Rico, June 4, 2004

[CNV05]   M. Cacciari, P. Nason and R. Vogt. *Phys. Rev. Lett.*, **95**:122001, 2005.

[CQM05]   H. B. Zhang et al. Quark Matter 2005, Budapest, Hungary, 4-9 Aug. 2005, *arXiv: nucl-ex/0510063*; J. Bielcik et al. *arXiv: nucl-ex/0511005*.

[Cro73]   J.W. Cronin et al. *Phys. Rev. Lett.*, **31**:1426, 1973.

[DDZ06]   X. Zhu et al. *arXiv: hep-ph/0604178*.

[DES04]   X. Dong, S. Esumi, P. Sorensen, N. Xu, and Z. Xu. *Phys. Lett. B*, **597**:328, 2004.

[DFS03]   D. de Florian and R. Sassot. *Phys. Rev. D*, **69**:074028, 2004.

[DG03]   M. Djordjevic and M. Gyulassy. *Phys. Lett. B*, **560**:37, 2003.

[DG04a]   M. Djordevic and M. Gyulassy. *J. Phys. G*, **30**:S1183, 2004.

[DG04b]   M. Djordjevic and M. Gyulassy. *Nucl. Phys. A*, **733**:265, 2004.

[DGV06]   M. Djordjevic, M. Gyulassy, R. Vogt and S. Wicks. *Phys. Lett. B*, **632**:81, 2006.

[DGW05]   M. Djordjevic, M. Gyulassy, and S. Wicks. *Phys. Rev. Lett.*, **94**:112301, 2005.

[DK01]   Y.L. Dokshitzer and D.E. Kharzeev. *Phys. Lett. B*, **519**:199, 2001.

[DKS03]   G. Dissertori, I. Knowles, and M. Schmelling. *Quantum Chromodynamics - High Energy Experiments and Theory*. Oxford Universidy Press, 2003.

[EKS98]   K. J. Eskola, V. J. Kolhinen and C. A. Salgado. *Eur. Phys. J. C*, **9**:61, 1999.

[FK02]   Z. Fodor and S.D. Katz. *J. High Energy Phys.*, **0203**:014, 2002.

[Glau01] P. Shukla *arXiv: nucl-th/0112039*, 2001.

[FMN97]   S. Frixione, M.L. Mangano, P. Nason, and G. Ridolfi. *arXiv: hep-ph/9702287*, 1997.

[Hou01]   P. Houvinen et al. *Phys. Lett. B*, **503**:58, 2001.

[GK04]   V. Greco and C.M. Ko. *Phys. Rev. C*, **70**:024901, 2004.

[GKL02]   M.I. Gorenstein, A.P. Kostyuk, McLerran L., H. Stöcker, and W. Greiner. *J. Phys. G*, **28**:2151, 2002.

[GKR04]   V. Greco, C.M. Ko, and R. Rapp. *Phys. Lett. B*, **595**:202, 2004.

[GR01]   L. Grandchamp and R. Rapp. *Phys. Lett. B*, **523**:60, 2001.

[Gra04]   L. Grandchamp. *Private communications*, 2004.

[Gup98]   R. Gupta. *arXiv: hep-lat/9807028*, 1998.

[Hbz03]   H. B. Zhang. Ph.D. Thesis, Yale University, 2003.

[HY04]   R.C. Hwa and C.B Yang. *Phys. Rev. Lett.*, **93**:082302, 2004.

[HYP06]   J. Adams et al. *arXiv: nucl-ex/0606014*.

[HGR06]   H. Hees, V. Greco and R. Rapp. *Phys. Rev. C*, **73**:034913, 2006.

[Joh02]   I. Johnson. Ph.D. Thesis, U.C. Davis, 2002.

[Kar02a] F. Karsch. *Lect. Notes Phys.*, **583**:209, 2002.

[Kar02b] F. Karsch. *Nucl. Phys. A*, **698**:199, 2002.

[KH03]   P.F. Kolb and U. Heinz. *arXiv: nucl-th/0305084*, 2003.

[KL01]   D. Kharzeev and E Levin. *Phys. Lett. B*, **523**:79, 2001.

[KLP00]   F. Karsch, E. Laermann, and A. Peikert. *Phys. Lett. B*, **478**:447, 2000.

[Kod91]   K. Kodama et al. *Phys. Lett. B*, **263**:573, 1991.

[Kop03]   B. Z. Kopeliovich. *Phys. Rev. C*, **68**:044906, 2003.

[Kos02]   Kostyuk et al. *Phys. Lett. B*, **524**:265, 2002.

[LG96]   Z. Lin and M. Gyulassy. *Phys. Rev. Lett.*, **77**:1222, 1996.

[Lin95]   Z. Lin et al. *Phys. Rev. C*, **51**:2177, 1995.

[Lin96]   Z. Lin. Ph.D. Thesis, Columbia University, 1996.

[LXY04]   X. Y. Lin. *arXiv: hep-ph/0412124*.

[LXY06]   X. Y. Lin. *arXiv: hep-ph/0602067*.

[LK02]   Z. Lin and C.M. Ko. *Phys. Rev. Lett.*, **89**:202302, 2002.

[Llo04]   W.J. Llope et al. *Nucl. Instr. Meth. A*, **522**:252, 2004.

[LM03]   Z. Lin and D. Molnar. *Phys. Rev. C*, **68**:044901, 2003.

[Lqe06]   J. Adams et al. *Phys. Rev. Lett.*, **97**:152301, 2006.

[LZZX06]   H. Liu, Y. Zhang, C. Zhong and Z. Xu. *Phys. Lett. B*, **639**:441, 2006.

[MNR93]   M.L. Mangano, P. Nason, and G. Ridolfi. *Nucl. Phys. B*, **405**:507, 1993.

[MS86]   T. Matsui and H. Satz. *Phys. Lett. B*, **178**:416, 1986.

[MT05]   G.D. Moore and D. Teaney. *Phys. Rev. C*, **71**:064904, 2005.

[MV03]   D. Molnar and S.A. Voloshin. *Phys. Rev. Lett.*, **91**:092301, 2003.

[NLC03]   G.C. Nayak, M.X. Liu, and F. Cooper. *Phys. Rev. D*, **68**:034003, 2003.

[Pbm00]   P. Braun-Munzinger and J. Stachel. *Phys. Lett. B*, **490**:196, 2000.

[PDG02]   K. Hagiwara et al. *Phys. Rev. D*, **66**:010001, 2002.

[PDG04]   S. Eidelman et al. "Review of Particle Physics." *Phys. Lett. B*, **592**:1+, 2004.

[PDG06]   W. M. Yao et al. *J. Phys. G*, **33**:1, 2006.

[PHECAA]   S. S. Adler et al. *Phys. Rev. Lett.*, **94**:082301, 2005. K. Adcox et al. *Phys. Rev. Lett.*, **88**:192303, 2002.

[PHECPP]   S. S. Adler et al. *Phys. Rev. Lett.*, **97**:252002, 2006.

[PHECRAA] S. S. Adler et al. *Phys. Rev. Lett.*, **96**:032301, 2006.

[PHEMu]   S. S. Adler et al. *arXiv: hep-ex/0609032*.

[Phpi0]   S. S. Adler et al. *Phys. Rev. Lett.*, **91**:072301, 2003.

[Pic95]   A. Pich. *arXiv: hep-ph/9505231*, 1995.

[Polem]   G. S. Huang et al. *Phys. Rev. Lett.*, **94**:011802, 2005; E. M. Aitala et al. *Phys. Rev. Lett.*, **80**:1393, 1998.

[PV98]   A.M. Poskanzer and S.A. Voloshin. *Phys. Rev. C*, **58**:1671, 1998.

[Rap01]   R. Rapp. *Phys. Rev. C*, **63**:054907, 2001.

[Rap06]   R. Rapp and H. Hees. *J. Phys. G*, **32**:S351, 2006.

[RP03]   J. Raufeisen and J.-C. Peng. *Phys. Rev. D*, **67**:054008, 2003.

[RRL03]   I.V. Rakobolskaya, T.M. Roganova, and Sveshnikova L.G. *Nucl. Phys. B (Proc. Suppl.)*, **122**:353, 2003.

[RS03]   R. Rapp and E.V. Shuryak. *Phys. Rev. D*, **67**:074036, 2003.

[Rua04a]   L.J. Ruan et al. *J. Phys. G*, **30**:S1197, 2004.

[Rua04b]   L.J. Ruan. Ph.D. Thesis, University of Science and Technology of China, 2004.

[Se04]   B. Muller *arXiv: nucl-th/0404015.*

[Sha02]   M. Shao et al. *Nucl. Instr. Meth. A*, **492**:344, 2002.

[Sha05]   M. Shao et al. *J. Phys. G*, **31**:S85, 2005.

[Sha06]   M. Shao et al. *Nucl. Instr. Meth. A*, **558**:419, 2006.

[Sj01]   T. Sjöstrand et al. *Computer Physics Commmun.*, **135**:238, 2001.

[Sor03]   P.R. Sorensen. Ph.D. Thesis, UC Los Angeles, 2003. *arXiv: nucl-ex/0309003.*

[Sor04a]   P.R. Sorensen. *Private communications*, 2004.

[Sor04b]   P.R. Sorensen. *STAR internal talk*, 2004.

[Sor99]   H. Sorge. *Phys. Rev. Lett.*, **82**:2048, 1999.

[SSH93]   E. Schnedermann, J. Sollfrank, and U. Heinz. *Phys. Rev. C*, **48**:2462, 1993.

[SS07]   S. Sakai. *Quark Matter 2006 proceeding, Shanghai, China.*

[STA03]   K.H. Ackermann et al. *Nucl. Instr. Meth. A*, **499**:624, 2003.

[STA04]   STAR TOF Collaboration. *STAR TOF Proposal*, 2004.

[STA05]   STAR HFT Collaboration. *STAR HFT Proposal*, 2005; Z. Xu et al. *J. Phys. G: Nucl. Part. Phys.*:32, S571, 2006; A. Rose et al. *Quark Matter 2006 proceeding, Shanghai, China.*

[STAc05]   J. Adams et al. *Phys. Rev. Lett.*, **94**:062301, 2005.

[STACRAA] J. Adams et al. *arXiv: nucl-ex/0607012.*

[Sto04]   R. Stock. *J. Phys. G*, **30**:S633, 2004.

[Tai04]   A. Tai et al. *J. Phys. G*, **30**:S809, 2004.

[Tav87]   S.P.K. Tavernier. *Rep. Prog. Phys.*, **50**:1439–1489, 1987.

[Tof05]   J. Adams et al. *Phys. Lett. B*, **616**:8, 2005.

[TSR01]   R.L. Thews, M. Schroedter, and J. Rafelski. *Phys. Rev. C*, **63**:054905, 2001.

[Vit03]   I Vitev. *Phys. Lett. B*, **562**:36, 2003.

[Vit06]   A. Adil and I. Vitev. *arXiv: hep-ph/0611109.*

[Vog02]   R. Vogt. *arXiv: hep-ph/0203151*, 2002.

[Vog03]   R. Vogt. *Int. J. Mod. Phys. E*, **12**:211, 2003.

[Vog04]   R. Vogt. *Private communications*, 2004.

[Vogt04]   R. Vogt. *Phys. Rev. C*, **70**:064902, 2004.

[Wan00]   X.N. Wang. *Phys. Rev. C*, **61**:064910, 2000.

[Wan04]   F. Wang et al. *J. Phys. G*, **30**:S1299, 2004.

[WG91]   X.N. Wang and M. Gyulassy. *Phys. Rev. D*, **44**:3501, 1991.

[Wic05]   S. Wicks et al. *arXiv: nucl-th/0512076.*

[Won94]   C.-Y. Wong. *Introduction to High-Energy Heavy-Ion Collisions*. World Scientific Publishing Co. Pte. Ltd., 1994.

[Xin05]   X. Dong. Ph.D. Thesis, USTC Hefei, China, 2005. *arXiv: nucl-ex/0509011.*

[Xu03]   N. Xu and Z. Xu. *Nucl. Phys. A*, **715**:587c, 2003.

[Xu04]   Z. Xu et al. *arXiv: nucl-ex/0411001*, 2004.

[Yan07]   Y. Lu. Ph.D. Thesis, CCNU Wuhan, China, 2007.

[YF06]   Y. F. Zhang. *J. Phys. G: Nucl. Part. Phys.*, **32**:S529-S532, 2006.

[YFHP06]   Y. F. Zhang, S. Esumi, H. Huang, Y. Miake, S. Sakai and N. Xu. *Nucl. Phys. A*, **783**:489, 2007.

[ZCK05]   B. Zhang, L.W. Chen, and C.M. Ko. *Phys. Rev. C*, **72**:024906, 2005.

[ZGK99]   B. Zhang, M. Gyulassy, and C.M. Ko. *Phys. Lett. B*, **455**:45, 1999.